# Carbonyl Sulfide in the Stratosphere: airborne instrument development and satellite based data analysis

Corinna Kloss

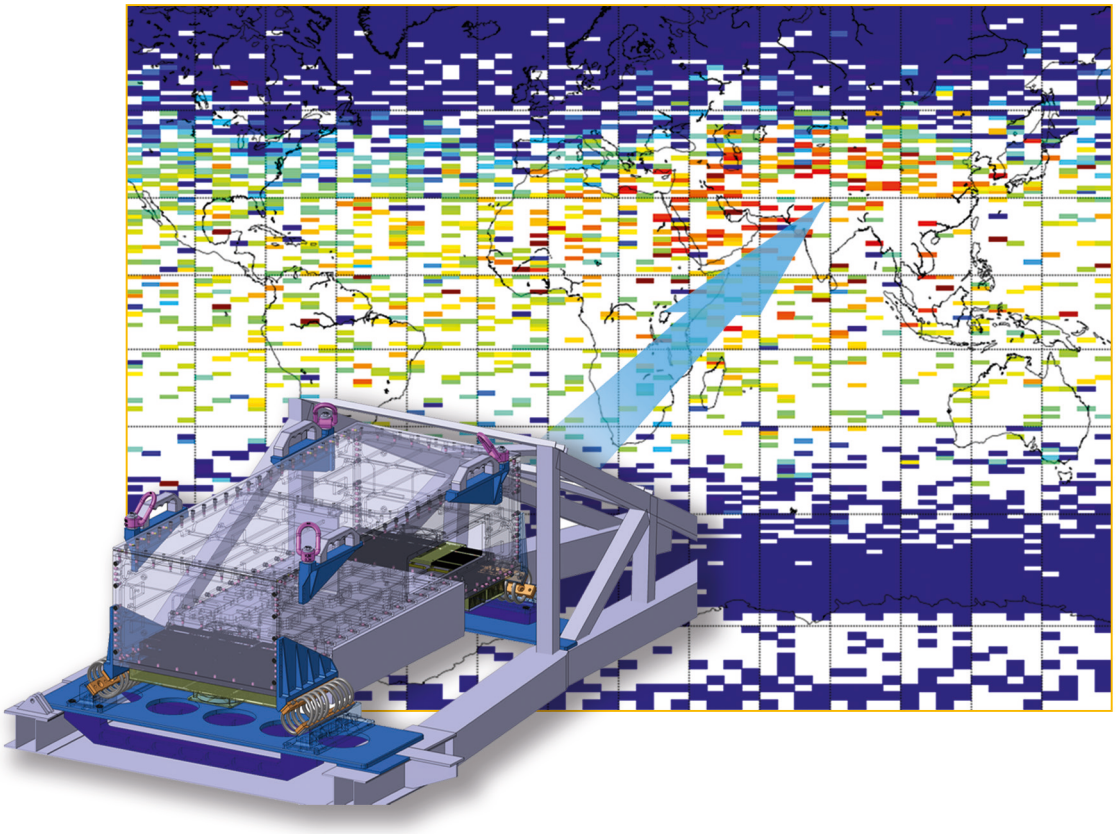

Energie & Umwelt / Energy & Environment
Band / Volume 399
ISBN 978-3-95806-276-4

JÜLICH
FORSCHUNGSZENTRUM

Schriften des Forschungszentrums Jülich
Reihe Energie & Umwelt / Energy & Environment Band / Volume 399

Forschungszentrum Jülich GmbH
Institute of Energy and Climate Research
Stratosphere (IEK-7)

# Carbonyl Sulfide in the Stratosphere: airborne instrument development and satellite based data analysis

Corinna Kloss

Schriften des Forschungszentrums Jülich
Reihe Energie & Umwelt / Energy & Environment Band / Volume 399

ISSN 1866-1793 ISBN 978-3-95806-276-4

Bibliographic information published by the Deutsche Nationalbibliothek.
The Deutsche Nationalbibliothek lists this publication in the Deutsche
Nationalbibliografie; detailed bibliographic data are available in the
Internet at http://dnb.d-nb.de.

Publisher and Distributor: Forschungszentrum Jülich GmbH
Zentralbibliothek
52425 Jülich
Tel: +49 2461 61-5368
Fax: +49 2461 61-6103
Email: zb-publikation@fz-juelich.de
www.fz-juelich.de/zb

Cover Design: Grafische Medien, Forschungszentrum Jülich GmbH

Printer: Grafische Medien, Forschungszentrum Jülich GmbH



Schriften des Forschungszentrums Jülich
Reihe Energie & Umwelt / Energy & Environment, Band / Volume 399

D 468 (Diss., Wuppertal, Univ., 2017)

ISSN 1866-1793
ISBN 978-3-95806-276-4

The complete volume is freely available on the Internet on the Jülicher Open Access Server (JuSER)
at www.fz-juelich.de/zb/openaccess.

# Abstract

Carbonyl sulfide plays a crucial role in the global atmospheric sulfur cycle and therefore for the global climate. It is the most abundant sulfur containing gas in the atmosphere during volcanic quiescence and is converted to aerosol in the stratosphere, which has a cooling effect on the climate. This work contributes to a better understanding of the role of $OCS$ in the upper troposphere and lower stratosphere. Satellite based data were analyzed and a new instrument AMICA (Airborne Mid-Infrared Cavity enhanced Absorption spectrometer) for in-situ $OCS$ measurements on stratospheric research aircraft was developed.

Using the $OCS$ data set from the satellite based instrument ACE-FTS, the stratospheric $OCS$ burden was calculated to be 524 Gg, which is 10 % of the total atmospheric $OCS$ budget and is in agreement with a sulfur cycle model. No trend in the global burden is observed between 2004 and 2016. Due to the sparse spacial coverage of the data set of ACE-FTS, a sampling bias arises when computing climatological averages over seasons and latitude bands. This sampling bias is corrected for with a newly developed procedure, using a mathematical interpolation. To estimate the significance and magnitude of the bias for each data point, the performance of the interpolation method was tested and some limitations identified.

Additionally, with the ACE-FTS data set, a significant increase in $OCS$ ($CO$ and $HCN$) mixing ratios is observed in the Asian monsoon anticyclone, a pathway from the highest polluted region on earth into the stratosphere. An analysis of the $HCN$:OCS ratios supports the suggestion of a transport from the Bay of Bengal region outside to the southern border of the anticyclone with air masses in the Asian monsoon anticyclone mostly originating from continental convection. The Asian monsoon and the features seen with the ACE-FTS data set will be investigated in detail with the new in-situ, high resolution instrument AMICA during the EU-project StratoClim.

AMICA has been developed and tested as part of this thesis. Important tests were made that contributed to the mechanical design and measurement set up in the final AMICA instrument. Key components include a box-shaped pressure tight enclosure, a flow system that regulates the cavity pressure over a wide ambient pressure range, spanning the full altitude range of available research aircraft, and the establishment of an $OCS$ calibration system.

AMICA successfully measured $OCS$ as well as $CO$, $CO_2$ and $H_2O$ during its first campaign that comprised three flights from Kalamata, Greece in summer 2016. $OCS$ measurements show de-

creasing mixing ratios in the stratosphere as expected and a larger variability in the UTLS region than expected. The complete data set of the important tropospheric tracer $CO$ was provided to the StratoClim community. A comparison with a nearby ACE-FTS profile shows a reasonably good agreement between AMICA and ACE-FTS in the stratosphere.
Further measurement flights in the UTLS region will help understand the detected higher variability of $OCS$ in the UTLS. This can improve the representation of $OCS$ in global climate models.

# Zusammenfassung

Carbonylsulfid ($OCS$) hat einen großen Einfluss auf den globalen Schwefelkreislauf und damit auch auf das globale Klima. In Zeiten geringer vulkanischer Aktivität ist $OCS$ das dominierende Schwefelgas in der Atmosphäre. In der Stratosphäre wird $OCS$ über Schwefeldioxid zu Aerosol umgewandelt. Stratosphärisches Aerosol hat einen kühlenden Effekt auf das Klima. Im Rahmen dieser Dissertation wird ein Beitrag zum Verständnis von $OCS$ und dessen Rolle in atmosphärischen Prozessen, in der oberen Troposphäre und unteren Stratosphäre geleistet. Hierzu wurden Satellitendaten analysiert und ein neues Messgerät AMICA (Airborne Mid-Infrared Cavity enhanced Absorption spectrometer), für Einsätze auf stratosphärischen Forschungsflugzeugen entwickelt.
Mit dem Satelliten Datenprodukt von ACE-FTS wurde die Gesamtmenge an stratosphärischem $OCS$ bestimmt, der sog. stratosphärische „Burden". Dieser beträgt 524 Gg, was gut mit der $OCS$ Repräsentierung eines Schwefelkreislauf Modells übereinstimmt und entspricht etwa 10 % der gesamten atmosphärischen $OCS$ Masse. Im gesamten bisherigen ACE-FTS Messzeitraum von 2004 bis 2016 ist kein signifikanter Trend zu beobachten. Wegen der lückenhaften, globalen Abtastung von ACE-FTS entsteht ein systematischer Fehler bei der Berechnung von klimatologischen Mittlungen über Breitengrad- und Zeitbereiche. Um diesen Fehler zu korrigieren wurde in dieser Arbeit eine Methode entwickelt, die auf einer mathematischen Interpolation basiert. Für eine Einschätzung der Größe und Signifikanz dieser Abweichung wurde diese Methode erprobt und Grenzen aufgezeigt.
Signifikant erhöhte $OCS$- ($CO$- und $HCN$-) Konzentrationen werden in der Antizyklone des asiatischen Monsuns, der als wichtiger Transportweg von dem Treibhausgas- verschmutzen asiatischen Raum in die Stratosphäre gilt, mit dem ACE-FTS Datensatz nachgewiesen. Ein $HCN$:$OCS$ Vergleich unterstützt die Annahme, dass Luftmassen aus der Bay of Bengal Region eher südlich der Antizyklone des asiatischen Monsuns transportiert werden und die Antizyklone eher von kontinentaler Konvektion gespeist wird. Der asiatische Monsun soll mit hochaufgelösten in-situ Messungen genauer untersucht werden.
Ein hochauflösendes, in-situ Messgerät AMICA für den Einsatz auf Flugzeug-Messkampagnen, wurde im Rahmen dieser Arbeit entwickelt und charakterisiert. AMICA ist ein hochauflösendes in-situ Spektrometer, entwickelt für den Einsatz auf Forschungsflugzeugen. Unter die Entwicklung und Erprobung einzelner Komponenten des Messinstruments fallen zum Beispiel ein druckdichtes

Gehäuse für die Messapparatur, ein Flusssystem zur Regulierung eines konstanten Drucks in den Messzellen (bei Schwankungen des Außendrucks während eines Messflugs) und ein geeignetes *OCS* Kalibrierungssystem.
Während der ersten Messkampagne in Kalamata, Griechenland im Sommer 2016, hat AMICA erfolgreich gemessen. Messungen zeigen, dass *OCS*, wie angenommen in der Stratosphäre abnimmt. In der oberen Troposphäre und unteren Stratosphäre (UTLS) zeigen die *OCS* Messungen eine höhere Variabilität als erwartet. Das AMICA *CO* Datenprodukt wurde der StratoClim Gemeinschaft zur Verfügung gestellt. Ein Vergleich mit einem nahe gelegenem ACE-FTS Messprofil zeigt eine gute Übereinstimmung mit AMICA *OCS*- und *CO*-Werten in der Stratosphäre. Ein Vergleich mit ACE-FTS *OCS* und *CO* Messungen zeigt eine gute Übereinstimmung der beiden Messinstrumente in der Stratosphäre.
Weitere geplante Messflüge mit AMICA werden zu einem besseren Verständnis der gemessenen *OCS* Variabilität in der UTLS beitragen, was zu einer besseren Parameterisierung von *OCS* in globalen Klimamodellen führen kann.

# Contents

# Chapter 1

# Introduction

Carbonyl Sulfide ($OCS$) in the upper troposphere and stratosphere, its contribution to the aerosol layer and its role in climate are the main focus of this work. In this chapter dynamical features of this atmospheric region, stratospheric aerosol and the current knowledge about $OCS$ and its contribution to the aerosol layer are discussed together with a motivation for the development of the new instrument AMICA (Airborne Mid-Infrared Cavity enhanced Absorption spectrometer).

## 1.1 The upper troposphere and stratosphere

In this work studies and measurements are done in the region of the upper troposphere and stratosphere (UTS). The lowest two layers of the atmosphere are the troposphere and stratosphere.
The troposphere:

- Temperature decreases with altitude down to around -60 °C.
- The average temperature decrease per 1 km altitude is 6.5 °C (net adiabatic lapse rate).
- Well mixed layer, containing all the weather we experience.
- The troposphere extends to the tropopause.

The tropopause:

- Higher in summer, lower in winter; higher in the tropics ($\sim$ 16 - 18 km, 100 hPa), lower at the poles ($\sim$ 6 - 9 km, 300 hPa).
- The tropopause altitude is defined as follows:
  - Thermal tropopause: as soon as the temperature decrease per 1 km rising altitude falls below 2 °C, that is the defined height of the thermal tropopause according to the World Meteorological Organization (WMO). It is the most commonly used definition.

- Dynamical tropopause: a potential vorticity (PV) threshold (usually between 2 and 4 PVU, Potential Vorticity Unit) is chosen (positive in the Northern Hemisphere and negative in the Southern Hemisphere) defining the dynamical tropopause in the extra tropics. Steep PV gradients on isentropes are associated with a transport barrier, reflected as the dynamical tropopause. In the tropics the dynamical tropopause is defined by the potential temperature (380 K).
- Chemical tropopause: the lower stratosphere exhibits much higher concentrations of ozone than the upper troposphere. Additionally, the upper troposphere contains much higher water concentrations, while the lower stratosphere is much dryer. The location of those steep gradients of concentration differences is used to define the chemical tropopause.

The stratosphere:

- The temperature increases with altitude.
- The ozone layer is situated in the stratosphere. By absorbing UV radiation it releases heat, causing the distinct temperature increase with altitude in the stratosphere. It protects the Earth's surface from the damaging UV-radiation.
- The stratosphere is situated between the tropopause and stratopause (at about 50 km, 1 hPa).

## 1.2 Stratospheric aerosol and OCS

Of the entire middle atmosphere, the one factor with the most immediate impact on climate is the stratospheric aerosol layer. Stratospheric aerosol absorbs near-infrared solar radiation and emits long wave radiation from the surface and backscatters solar shortwave radiation to space. The net effect on the Earth's surface is cooling. Hence, the more aerosol accumulates in the stratosphere, the higher is the negative radiative forcing, which leads to a cooling of the Earth's surface. In contrast, however, in the troposphere, aerosol significantly absorbs longwave radiation, leading to an increased warming effect (compared to stratospheric aerosol), which balances or even leads to a warming of the net effect.
With a maximum at 15 to 23 km altitude, the aerosol layer was first discovered in Junge et al. (1961) and Junge and Manson (1961) and is therefore also referred to as 'Junge layer'. Aerosols in the stratosphere, unaffected by volcanoes have a particle radius below 2$\mu$m (Kremser et al., 2016).
After strong volcanic eruptions, which inject sulfate material directly into the stratosphere, the surface temperature decreases significantly on a global scale for typically a few years. The phenomenon of one volcano eruption influencing the global climate was first described in Simkin

and Fiske (1983). 'The year without summer' in 1816, causing enormous damage in northern America and Europe was assigned to the Tambora eruption in 1815. The Pinatubo eruption 1991 is a more recent example of a volcanic eruption with a global climate influence, with a global mean surface temperature drop of nearly 0.4 °C (Thompson et al., 2009).
An updated overview of stratospheric aerosol and the sulfur cycle is given in Kremser et al. (2016).

### 1.2.1 Transport of sulfur compounds into the stratosphere

The current knowledge on transport- and conversion processes of stratospheric aerosol is presented in Figure 1.1. Stratospheric aerosol mainly consists of sulfate droplets, with contributions from meteoritic and other non-sulfate material. The main transport pathways of sulfur compounds into the stratosphere are:

- Volcanic eruptions: depending on the location and strength of a volcanic eruption, sulfate particles are directly introduced into the stratosphere. Additionally, minor eruptions have an important impact on the climate so that background (no volcanic influence) conditions are hard to find during the last decade (Solomon et al. (2011) and Vernier et al. (2011b)). Injection of sulfur compounds by volcanic eruptions is the main contributor for the stratospheric sulfur and aerosol budget.
- Tropical convection: in the absence of volcanic eruptions, the largest part of sulfur compounds from the surface is transported via tropical convection in the tropics across the tropical tropopause layer (TTL) into the stratosphere, where it is converted to aerosols as seen in Figure 1.1.
- Asian monsoon: another significant pathway of tropospheric air masses (containing sulfur compounds) into the stratosphere is the Asian monsoon anticyclone (Randel et al., 2010), which appears every year between June and September above Asia. A potential vorticity based approach for a definition of the location of the Asian monsoon anticyclone was made by Ploeger et al. (2015). During the Asian monsoon, highly polluted surface air is convectively transported into a strongly isolated anticyclone, showing enhanced mixing ratios of tropospheric tracers and lower mixing ratios of stratospheric tracers, as satellite studies show (Park et al., 2008). Vogel et al. (2015) identify northern India and Southeast Asia as the main boundary layer source regions for the composition of the Asian monsoon anticyclone. The distinct isolation of trace gases in the anticyclone provides an ideal case for investigating common sources and sinks of different substances. For example, the correlation between $HCN$ (and $CO$) as a biomass burning tracer and $OCS$ could help quantifying how much biomass burning contributes as a source for $OCS$. Enhanced aerosol concentrations in the Asian monsoon (ATAL: Asian Tropopause Aerosol Layer) have been found and are matter of investigation (Vernier et al., 2011a). It is considered

as a pathway for anthropogenic sulfur compounds from the whole Asian region into the stratosphere (Vernier et al., 2011a). However, observations allowing a quantification of how much of this material is transported into the stratosphere after the Asian monsoon anticyclone breaks down are missing (Kremser et al., 2016).

Once a sulfur containing air parcel reaches the free troposphere or stratosphere and is not taken up by surface sinks, most sulfur compounds are readily converted to $H_2SO_4$, mainly through reaction with hydroxyl radical ($OH$). The conversion of $SO_2$ to $H_2SO_4$ is described in the simplified reaction Sequence 1.1.

$$\begin{aligned} SO_2 + OH &\rightarrow SO_3 + H \\ SO_2 + O &\rightarrow SO_3 \\ SO_3 + H_2O &\rightarrow H_2SO_4 \end{aligned} \tag{1.1}$$

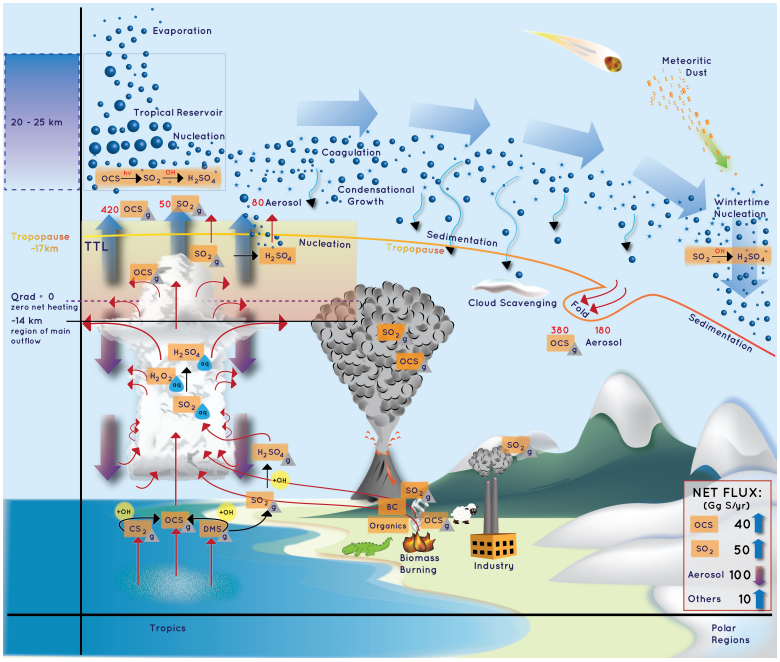


**Figure 1.1:** Schematic view of the processes involved in the stratospheric aerosol life cycle. Blue thick arrows indicate the large scale circulation, Brewer-Dobson Circulation (BDC). Red arrows show transport processes, and blue thin arrows stand for sedimentation processes from the stratosphere down to the troposphere. Red numbers stand for the net flux and are taken from Sheng et al. (2015). Figure adopted from Kremser et al. (2016).

Once $H_2SO_4$ is formed, it accumulates $H_2O$ to form aerosol through nucleation. Aerosols grow further through coagulation and condensation, where coagulation refers to the process of multiple already formed particles colliding to form one bigger particle.

### 1.2.2 Role, mixing ratio and budget of Carbonyl Sulfide

While short lived sulfur compounds just reach the stratosphere through deep convection in the tropics, $OCS$ (Carbonyl Sulfide) also reaches the upper troposphere lower stratosphere (UTLS) region without deep convection due to its long tropospheric lifetime of 2 - 7 years (Xu et al., 2002). $OCS$ is the most stable and abundant sulfur containing gas in the atmosphere. A model study by Sheng et al. (2015) describes that $OCS$ accounts for 74 % of the total sulfur mass in the troposphere and 70 % in the stratosphere.
The first one to suggest that $OCS$ plays a dominant role in transporting sulfur through the tropopause into the stratosphere was Crutzen (1976). More recent studies by Brühl et al. (2012) and Sheng et al. (2015) confirm and strengthen this suggestion with aerosol models: Brühl et al. (2012) suggest that $OCS$ contributes about 70 % of sulfur to the aerosol layer for background conditions. The model described in Sheng et al. (2015) shows: if all other sulfur compounds (such as $SO_2$, $H_2S$ and $DMS$) are switched off, $OCS$ alone establishes 56 % of the current stratospheric aerosol layer. The differences are possibly due to insufficient surface emission representations of short-lived sulfur containing species and uncertainties in transport processes through the tropopause into the stratosphere (Sheng et al., 2015).
The annual mean $OCS$ mixing ratios in the Northern Hemisphere (from seven surface sites during 2000 - 2005) are 476 $\pm$ 4 ppt and 491 $\pm$ 2 ppt in the Southern Hemisphere (Montzka et al., 2007). $OCS$ mixing ratios remain relatively constant throughout the well-mixed troposphere. In the UTLS $OCS$ mixing ratios are above 400 ppt and decrease with increasing latitude and altitude (Barkley et al., 2008). This $OCS$ distribution is mainly determined by the global atmospheric transport (i.e. Brewer-Dobson-Circulation, age of air). In the middle and upper stratosphere $OCS$ is photochemically depleted. The rate of photochemical depletion increases with increasing altitude.
An overview of the current knowledge on the $OCS$ budget and the individual sources and sinks is shown in Figure 1.2. It is evident that $OCS$ sources and sinks carry large uncertainties.
As seen in Figure 1.2, oceans are the largest source of $OCS$ (Chin and Davis, 1993), not only as a direct source but also as an indirect source via Carbon Disulfide ($CS_2$) and Dimethyl Sulfide ($DMS$) (Kettle et al., 2002). $CS_2$ and $DMS$, emitted from the ocean into the atmosphere are oxidized to sulfur species, with $OCS$ as one product.
The main sink for $OCS$ is uptake by vegetation (Montzka et al., 2007), cf. Figure 1.2. The strength of vegetation as a sink is also largely uncertain: while Kettle et al. (2002) suggest an $OCS$ surface uptake by vegetation of around 200 - 300 Gg S/a, Montzka et al. (2007), Sandoval-

Soto et al. (2005) and Stimler et al. (2010a) suggest a significant upward correction of the vegetation sink represented by the larger gray bar in Figure 1.2.
Soils are mainly a sink for $OCS$, but can also act as a source, as seen in Figure 1.2. The sink strength of soil depends on moisture and temperature (Van Diest and Kesselmeier, 2008). Because $OCS$ does not show a significant atmospheric trend or inter annual variability, this upward revision of the vegetation sink suggests a missing source in the atmospheric $OCS$ budget of around 700 - 800 Gg S per year (Kuai et al. (2015) and Glatthor et al. (2015)). This missing source was assigned via satellite observations to most likely originate from the tropical ocean by Kuai et al. (2015) and Glatthor et al. (2015), FTIR (Wang et al., 2016) and an inverse modeling study (Berry et al., 2013). However, with data collected from ship cruises in the tropical Atlantic, Pacific and Indian oceans, Lennartz et al. (2017) shows that direct and indirect $OCS$ emissions from the ocean are very unlikely to account for the missing atmospheric $OCS$ source. Therefore, the large uncertainties and missing atmospheric $OCS$ sources remain. Lennartz et al. (2017) used the MICA (Mid-Infrared Cavity enhanced Absorption spectrometer) instrument for their analysis, as described in Chapter 3.3.1.
Biomass burning is another source for $OCS$. Barkley et al. (2008) and Notholt et al. (2003) see a correlation between biomass burning tracers ($HCN$ and $CO$) and $OCS$, by analyzing backward trajectories of enhanced $OCS$ in biomass burning plumes. $HCN$ is an almost unambiguous tracer of biomass burning. However, analysis of a larger, global data set, in more recent studies, found no evidence for this correlation (Glatthor et al., 2017).
Alternatively, Du et al. (2016) and Barletta et al. (2009) suggest that an underestimated additional anthropogenic source is coal and biofuel combustion in Asia, emitting $OCS$. This source accounts for around 30.5 Gg S/a, which is one magnitude larger than the current $OCS$ estimation from coal combustion in China (Du et al., 2016), but it would not quantitatively account for the missing source in the $OCS$ budget.
In the stratosphere oxidation takes place and sulfate particles are formed (Equation 1.2, 1.3 and 1.4). The total estimated stratospheric net $OCS$ flux is 30 Gg S/a by Chin and Davis (1995) and 40.7 by Sheng et al. (2015). Barkley et al. (2008) estimates the stratospheric sink to be at 63 - 124 Gg $OCS$/a (equivalent to 34 - 66 Gg S/a). 90 % of $OCS$, which reaches the stratosphere, returns back into the troposphere.
Sheng et al. (2015) describe the total tropospheric and stratospheric budgets with the SOOCL-AER model results. The tropospheric budget of 2650 Gg S and the stratospheric budget of 283.1 Gg S, agree well with the calculated atmospheric $OCS$ mass of 5.34 $\cdot 10^3$ Gg $OCS$ (equivalent to 2852 Gg S) by Barkley et al. (2008). Large uncertainties in the $OCS$ budget balance remain.
The tropospheric lifetime of $OCS$ is strongly related to the strength of its sources and sinks. The high uncertainty described above, leads to large uncertainties in tropospheric lifetime estimations.

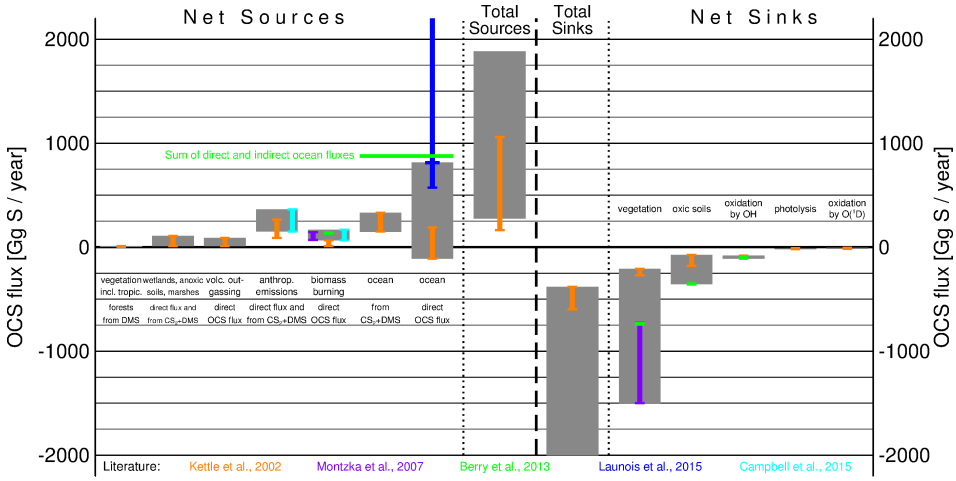


**Figure 1.2:** The tropospheric $OCS$ budget. Color bars represent values for sinks and sources from different literature. Gray bars represent possible ranges, based on all available literature, adopted from Kremser et al. (2016).

Johnson (1981) estimate an $OCS$ tropospheric lifetime of 4 - 7 years and Ulshöfer and Andreae (1997) calculate a lifetime of 5.7 years. Until recently this tropospheric lifetime for $OCS$ was still valid, however, considering enhanced surface sinks (larger by a factor of around 2), the $OCS$ tropospheric lifetime decreases to 2.5 years (Montzka et al., 2007). Compared to other species (e.g. $SO_2$ exhibits a tropospheric lifetime on the order of days) $OCS$ has a relatively long tropospheric lifetime and therefore does not necessarily need deep convection in the tropics to reach the stratosphere. The $OCS$ lifetime in the stratosphere is highly variable and depends on the altitude. Barkley et al. (2008) calculate a total mean stratospheric lifetime of $64 \pm 21$ years. This value is determined over a correlation with other long lived tracers. The higher an $OCS$ molecule is transported, the faster it is depleted via photolysis. Chin and Davis (1995) estimate a photochemical lifetime in the stratosphere of 10 years (in the troposphere 36 years), considering only the destruction processes as described in Equation 1.2.
According to Sheng et al. (2015), the conversion to $SO_2$ in the stratosphere takes place to 80 % via photolysis (Equation 1.2), 17 % is converted via the reaction with $O(^1D)$ and 3 % via reaction with $OH$ (Equations 1.3 and 1.4). Different values are given in Chin and Davis (1995): 71 % via photolysis, 22 % via the reaction with $O(^1D)$ and 7 % via reaction with $OH$. The photolysis rate increases with altitude, due to elevated UV levels (Chin and Davis, 1993).

$$\begin{aligned} OCS + h\nu &\rightarrow CO + S \\ S + O_2 &\rightarrow SO_2 \end{aligned} \tag{1.2}$$

$$\begin{aligned} OCS + O(^1D) &\rightarrow CO + SO \\ SO + OH &\rightarrow SO_2 + H \end{aligned} \tag{1.3}$$

$$\begin{aligned} OCS + OH &\rightarrow CO + H + SO \\ SO + OH &\rightarrow SO_2 + H \end{aligned} \tag{1.4}$$

Once $OCS$ is converted to $SO_2$ (Equation 1.2), it rapidly reacts further to $H_2SO_4$ (Equation 1.1). As shown in Höpfner et al. (2013), a maximum of $SO_2$ in the tropics at an altitude of around 25 km indicates that most $OCS$ is converted through photolysis to $SO_2$.

### 1.2.3 OCS trends and seasonality

Montzka et al. (2004) present $OCS$ mixing ratios of 330 ppt in the time period 1700 - 1850, based on studies of Antarctic ice core and firn air analysis. Since then, mixing ratios have increased to 500 ppt.
Multiple studies present controversial findings about the atmospheric longterm trend of $OCS$ for the last $\sim$ 50 years: early studies with ground based remote sensing (e.g. Rinsland et al. (2002) for the period 1978 - 2002 and Mahieu et al. (2003) for the period 1988 - 2002) suggest a negative trend for tropospheric $OCS$ of 0.5 - 1 % per year. Coffey and Hannigan (2011) do not find significant trends in total column $OCS$ between 1975 and 2010, using observations from an airborne infrared spectrometer from the base to the stratosphere. In addition, there is no significant trend observed by Montzka et al. (2007) and Rinsland et al. (2008) at ground based sites throughout the globe from 2000 to 2005. However, a recent study by Kremser et al. (2015) identifies a significant positive increase of $OCS$ in the Southern Hemisphere using three ground based Fourier Transform spectrometer.
$OCS$ concentrations show a significant seasonality in the troposphere in both hemispheres (Kettle et al. (2002), Montzka et al. (2007)). While the lowest concentration in the Northern Hemisphere is seen in late summer (September) due to uptake by vegetation during summer, in the Southern Hemisphere lowest concentrations are detected during winter (July), due to high oceanic fluxes of $OCS$ (and $CS_2$, $DMS$) in the summer.

## 1.3 OCS observations

Nearly all trace gases, including $OCS$ have absorption features in the infrared region (IR). A spectroscopic setting with a long path length is needed to achieve sensitive measurements of gases with weak absorption features. Such long path lengths are e.g. achieved by satellite instruments,

looking at the sun with solar occultation, where the line of sight crosses hundreds of kilometers through the atmosphere. However, small scale processes e.g. chemical conversion rates are only accessible with high resolution in-situ measurements. The variety of remote sensing $OCS$ measurements, but also the development of infrared spectroscopy for highly sensitive in-situ $OCS$ observations, are explained below.

### 1.3.1 Remote sensing

The first space-borne instrument, allowing global measurements of $OCS$ was ATMOS (Atmospheric Trace Molecule Spectroscopy Experiment) on the space shuttle ATLAS (Atmospheric Laboratory for Applications and Science) that is described in Kaye and Miller (1996) and went on 4 shuttle missions in 1985, 1992, 1993 and 1994. Since 2004, the ACE-FTS instrument (Atmospheric Chemistry Experiment - Fourier Transform Spectrometer), an infrared solar occultation spectrometer, delivers space-borne $OCS$ data. First global UTLS $OCS$ concentrations from ACE have been shown in Barkley et al. (2008). The ACE-FTS $OCS$ data are used in this work and are discussed in Chapter 2. From 2002 to 2012 the infrared limb sounding instrument MIPAS (Michelson Interferometer for Passive Atmospheric Soundings) on board of the satellite ENVISAT (Environmental Satellite) also delivered $OCS$ data (Glatthor et al., 2015). While MIPAS has a much better global coverage, ACE has the main advantage that it is still measuring and delivering data. Another space-borne instrument providing $OCS$ data is the TES (Tropospheric Emission Spectrometer), from which a seasonal and latitudinal tropospheric variability can be derived (Kuai et al., 2014). The dataset was validated by NOAA ground based observations and the HIPPO (HIAPER Pole-to-Pole Observations) aircraft measurements. New $OCS$ measurements from the nadir-viewing instrument IASI (Infrared Atmospheric Sounding Interferometer) since 2014 are introduced in Vincent and Dudhia (2017).
At several locations ground based FTIR (Fourier transform infrared spectrometer) measure high resolution spectra, looking at the tropospheric and stratospheric column amount (http:www.ndacc.org).
The longest $OCS$ measurement record is given by Rinsland et al. (2008), who reanalyze infrared solar spectra back to 1951 at the Jungfraujoch.

### 1.3.2 In-situ observations

The first to measure atmospheric $OCS$, were Hanst et al. (1975) with a long path infrared absorption spectrometer. A few years later Inn et al. (1979) presented the first $OCS$ measurements in the stratosphere, also using long path infrared spectroscopy. For an improved sensitivity, Bandy et al. (1992) introduce a gas chromatographic approach, collecting airborne gas samples and analyzing them for $OCS$. Fried et al. (1991) were the first to present $OCS$ measurements with a multi-pass cell. Since then, some vertical profiles are measured during balloon flights in

the tropics and northern high latitudes (Krysztofiak et al., 2015b) and during aircraft flights throughout a year in the United States (Montzka et al., 2007). HIPPO is a sequence of global aircraft measurement programs, measuring multiple Greenhouse Gases with a QCL (Quantum Cascade Laser) from the surface up to 14 km, spanning all seasons (Wofsy, 2011). Stimler et al. (2010b) also describe highly sensitive $OCS$ measurements using a mid infrared QCL.
Common multi-pass cells achieve path lengths of several hundred meters. This can be increased significantly by cavity enhanced methods. Those methods all go back to the cavity ringdown spectroscopy first described by (O'Keefe and Deacon, 1988). The better the reflectivity of the mirrors, the longer the absorption path (this is also further discussed together with the measurement technique used in this work in Chapter 3.2). Cavity enhanced spectrometers in the near infrared and mid infrared region are commercially available for numerous trace gases. A cavity enhanced technique that is sensitive, robust and easy to implement is the Off-Axis Integrated Cavity Output Spectroscopy (OA-ICOS), suitable for in-situ measurements on moving platforms as research aircraft. OA-ICOS is now a well-established technique for ground based measurements producing successful measurements of e.g. $CO$, $CH_4$, $CO_2$ and water isotopes. ICOS measurements on high altitude research aircraft have been made (i.a. Provencal et al. (2005), O'Shea et al. (2013), Sayres et al. (2009)). In Chapter 3 the development of AMICA, measuring a variety of gases, including $OCS$ is presented.

### 1.3.3 Motivation for the Airborne Mid-Infrared Cavity enhanced Absorption spectrometer (AMICA)

Because $OCS$ is the main contributor to the stratospheric aerosol layer, which has a direct impact on the climate during volcanic quiescence, it is necessary to quantify and investigate transport processes of $OCS$ and the conversion processes of $OCS$ to $H_2SO_4$ and aerosol.
In-situ measurements can be used to study transport and conversion processes (i.e. conversion from $OCS$ to $H_2SO_4$) on much smaller spacial and temporal scales that are usually not accessible for remote sensing. For fast atmospheric processes, it is important to measure exactly at the point where conversion takes place, using an instrument with a higher spacial resolution than any remote sensing instrument provides. High altitude research aircraft are ideal platforms for that. A high sensitivity is required to detect small and steep gradients for different altitudes. The instrument needs to function under low pressure (down to 50 hPa) and low temperature (down to around -80 °C) conditions to perform measurements in the UTLS. Furthermore, the measurement technique has to be robust against vibrations of aircraft. All those features are considered during the development of the electronic and mechanical design of AMICA.
Another scientific question that is not well understood yet, is the quantification of biomass and biofuel burning in the Asian monsoon area as a source for $OCS$. For this purpose, specific air masses that can be traced back (using back trajectories) to biomass burning sources and are

directly transported to the tropical tropopause region are observed and investigated for a correlation between $OCS$ and other biomass burning tracers (i.e. $HCN$ and $CO$). AMICA also measures $CO$ and is in development to also measure $HCN$, as a biomass burning tracer. This will yield some insight about biomass burning as a possible source for $OCS$.
As discussed in Chapter 1.2.1 the Asian monsoon anticyclone holds enhanced aerosol concentrations (ATAL), which need to be investigated in more depth, ideally with in-situ measurements, during a tropical field campaign. Additionally, an investigation of the pathway of the sulfur compound $OCS$ into the stratosphere during the break down of the Asian monsoon anticyclone is necessary. Therefore, measuring $OCS$ with high resolution with AMICA in the Asian monsoon anticyclone is valuable. For the EU-project StratoClim such an in-situ aircraft campaign was conducted this summer July/ August 2017 in Kathmandu, Nepal.

### 1.3.4 M55 Geophysica observations during StratoClim

Stratospheric and upper tropospheric processes for better climate predictions (StratoClim), is a collaborative European project, with a planed time duration of 52 months, under the coordination of Marcus Rex (AWI: Alfred-Wegener-Institut). The project started in December 2013 and involves 28 partners from 11 countries. Goal of this project is the improvement of our understanding of changes of the chemical composition in the UTS, which has been shown to play a major role in changes of our surface climate. Results are intended to be implemented in Chemical Climate Models (CCMs) and Earth System Models (ESMs). A large scale tropical aircraft campaign around the Asian monsoon took place this year. During this phase of the StratoClim project, AMICA was one of the in-situ instruments, measuring on the research aircraft M55-Geophysica, a high altitude research aircraft. It reaches altitudes of 21 km at pressures down to 55 hPa and temperatures down to -90 °C. It was built originally 1987 as a military aircraft. Since 1995, it is used as a scientific research aircraft, currently holding 27 different atmospheric measurement instruments simultaneously. Until now, it performed 135 scientific measurement flights. Due to political and logistical constrains the first phase campaign and the main tropical aircraft campaign of StratoClim have been shifted multiple times. The first phase campaign took place in Kalamata, Greece in August/September 2016. In the summer of 2017 the main campaign took place. AMICA data from the Kathmandu campaign are currently processed. Therefore, this work presents the first measurement flights, the performance of AMICA and first scientific results from the campaign in Kalamata 2016, but does not include a scientific dataset from the main StratoClim campaign in the Asian monsoon region.

# Chapter 2

# Stratospheric OCS with ACE-FTS

ACE-FTS is the Atmospheric Chemistry Experiment – Fourier Transform Spectrometer (Bernath et al., 2005). With the ACE-FTS data set it is possible to obtain a global, vertical and horizontal *OCS* distribution, as it was already shown in Barkley et al. (2008). In this Chapter the ACE-FTS data set is used to calculate the stratospheric *OCS* burden and trend, together with an investigation of *OCS* mixing ratios in the Asian monsoon region. Due to the sparse sampling pattern of the solar occultation instrument ACE-FTS, a sampling bias appears that might alter the burden trend analysis. To determine representative annual and seasonal burden values, a correction procedure is developed by fitting a smooth 2-D array onto the ACE-FTS dataset, considering an annual cycle of *OCS* for the fit coefficients. This procedure is analyzed and applied.

## 2.1 ACE-FTS OCS data product

ACE-FTS is an infrared solar occultation spectrometer, providing remote sensing trace gas profiles of the Earth since February 2004. It is the main instrument on the Canadian satellite SCISAT-1, which was launched in August 2003. ACE-FTS still delivers data. The design lifetime for ACE was 2 years. ACE-FTS measures sequences of atmospheric spectra in the limb viewing geometry at different tangent heights, during sunset and sunrise, pointing towards the sun, with a vertical field of view of 3 - 4 km. Absorption features of over 30 chemical species (i.a *OCS*) are measured together with temperature and pressure. It is in an orbit at 650 km altitude and operates in the wavelength range from 2.2 to 13.3 $\mu$m (750 - 4400 cm$^{-1}$). The spectral resolution is 0.02 cm$^{-1}$.
Vertical distributions are provided (on a 1 km grid), reconstructed from the retrieval. Altitude profile information from around 5 km (or cloud top) to 150 km are provided. ACE-FTS samples the atmosphere vertically at around 2 - 6 km intervals. The horizontal weighting function of a measurement has typically a width of $\sim$ 300 km. The vertical resolution is $<$ 4 km.

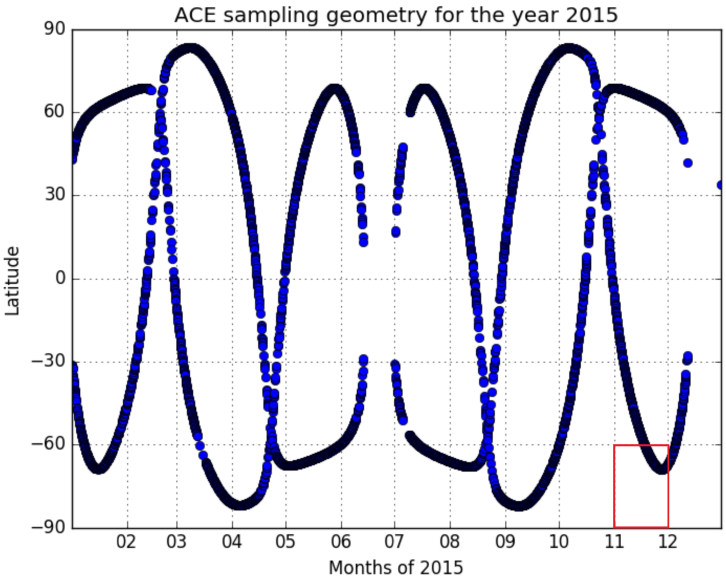


**Figure 2.1:** The annual repeating latitudinal coverage of the ACE-FTS data set, here for the year of 2015. The red box is later on used as an example.

30 measurements (15 sunrises, 15 sunsets) are made per day. The polar regions to the tropics (85°N to 85°S) are covered. The annual coverage is shown in Figure 2.1. It is evident that the densest coverage of ACE-FTS is close to the poles, while the tropics exhibit a lower coverage. However, directly at the poles, no measurements are available.
During each three months season the full latitude range is covered. A detailed description of the ACE-FTS and its measurement technique is given in Bernath et al. (2005). Data from March 2004 until October 2016 were available and used in this work.
The sparse coverage of the ACE-FTS data set results in a sampling bias that needs to be considered. The occurring sampling bias and an approach of correcting it, is introduced in Chapter 2.2.

## 2.2 ACE-FTS satellite sampling bias correction

### 2.2.1 Motivation

Analyzing satellite data, is often done by collecting available observations into latitudinal and monthly bins and calculating the respective mean (or budgets). The sampling of occultation based satellite instruments along an orbit show patterns that are not randomly distributed and follow the same latitudinal coverage every year, leading to a sampling bias. For the example of the red box in Figure 2.1, taking a mean concentration of the few values in the box (all situated in the

upper right corner of the box) will not be representative for the whole area. $OCS$ mixing ratios decrease towards the poles, therefore lower mixing ratio values are missing for the example of the red box in Figure 2.1 and the real respective mean concentration value is consequently lower, than the mean value of only the few measurement points in the box. Therefore, the sampling density and distribution of a chosen box for average calculations, is strongly connected to the sampling bias that consequently occurs. The additional error of the sampling bias to the natural sensitivity of the measurement itself needs to be considered when dealing with space-borne data sets (Toohey and von Clarmann (2013), Toohey et al. (2013)). While the largest fraction of the error still results from the measurement uncertainty itself (Toohey and von Clarmann, 2013), sampling bias from measurements of satellite borne instruments account for an additional significant error (e.g. Toohey and von Clarmann (2013) and Toohey et al. (2013)). For instruments like ACE-FTS with sparse sampling density (with only 30 measurements per day), the sampling bias is higher than for instruments with a denser sampling.
The overall 12 monthly sampling bias estimate in % for ACE-FTS is shown in Figure 2.2 for the example of $O_3$. $O_3$ exhibits similar strong latitudinal gradients in the stratosphere to $OCS$ so that a comparable extent of a sampling bias for $OCS$ is possible. The sampling bias for $O_3$ is generally weaker below 70 hPa altitude pressure in the tropics (roughly equivalent to $>$ 18 km altitude), this is due to weaker intra-monthly variability in that region. A strong variability, as it appears in the Southern Hemispheric spring months at 80 - 85° latitude during the polar vortex, associated with steep gradients (Toohey et al., 2013), can lead to a sampling bias of $O_3$ in ACE-FTS of up to 40 % (Toohey et al., 2013).
Current literature have raised awareness and have quantified the error resulting from the sampling bias, however, they have not presented solutions on how to correct space-borne data with respect to this problem. Here, one possible approach is developed together with Bodeker Scientific in New Zealand to find a solution that deals with the sampling bias of ACE-FTS, using only ACE-FTS data and no additional information. With a full global climatological field of $OCS$ it is possible to estimate the real mean value of a specific time period and latitude range. A smooth 2-D regression is fitted to the ACE-FTS $OCS$ data, filling the large data gaps. This is a reasonable approach, considering that $OCS$ has a long lifetime (2 - 7 years in the troposphere (Xu et al., 2002)), 64 years in the stratosphere (Barkley et al., 2008)) and no diurnal (only annual) cycle, thus no sudden changes in $OCS$ mixing ratios are expected. Chapter 2.2.2 introduces the model. The 2-D regression field is used to adjust the mean value that is calculated from the biased data so that it is more representative for a chosen period and region.

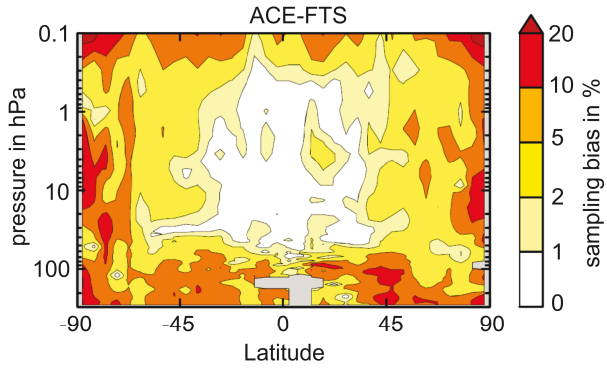


**Figure 2.2:** Latitude height plot of the 12 monthly root-mean-square (RMS) of the sampling bias for the example of $O_3$ in percent for the sampling pattern of ACE-FTS, from Toohey et al. (2013)

### 2.2.2 Bodeker Scientific Regression Model (BSRM)

The BSRM was specifically designed to model global atmospheric conditions. The BSRM can be used in different dimensions of space, time and height. Here, it is used to fit a smooth 2-D surface onto the annual measured $OCS$ ACE-FTS data per latitude at one specific altitude. The method described here is a statistical approach that can only describe large-scale features, but not small-scale variabilities and is suitable for substances with long lifetimes, as $OCS$. The BSRM uses a combination of Legendre polynomials and Fourier expansions. A detailed description of the regression is given in Hassler (2009) and Bodeker et al. (2013). The Fourier expansion describes the temporal development and variations such as seasonal dependencies (1 Fourier expansion: annual cycle, 2 Fourier expansions: half-year cycle), with a sum of sine and co-sine functions. Associated Legendre expansions describe the latitudinal change also with sine and cosine functions. Therefore, seasonal variability, but also latitudinal variations seen in the global $OCS$ ACE-FTS data set can be represented in this regression, using both Legendre polynomials and Fourier series. The number of Fourier and Legendre expansions can be selected individually for different substances and constrain the possible modeled climatological field of $OCS$. For substances, which exhibit no diurnal but annual changes (e.g. $OCS$), 1 Fourier expansion is chosen. The number of Legendre expansions is chosen according to expected (and observed) changes in latitude. The selection of suitable number of Fourier and Legendre terms for the $OCS$ ACE-FTS application is introduced in Chapter 2.2.3.

Equation 2.1 describes the regression model distribution depending on day and latitude (OCS(lat,day)) and the fit coefficients. The number of fit coefficients is determined by: $(2 \cdot$ number of Fourier $+ 1) \cdot$ (number of Legendre $+ 1$). For example, using 1 Fourier and 4 Legen-

dre terms, results in a total of 15 coefficients ($a_{00}$ to $a_{24}$). The Legendre expansions ($a_0$ to $a_2$) are inserted in the Fourier series. $P_1$ to $P_4$ are the Legendre polynomials.

$$OCS(day, lat) = a_0(lat) + a_1(lat) \times sin(2\pi day/365.25) + a_2(lat) \times cos(2\pi day/365.25) \quad (2.1)$$

$$\begin{aligned} a_0 &= a_{00} + a_{01} \cdot P_1 + a_{02} \cdot P_2 + a_{03} \cdot P_3 + a_{04} \cdot P_4 \\ a_1 &= a_{10} + a_{11} \cdot P_1 + a_{12} \cdot P_2 + a_{13} \cdot P_3 + a_{14} \cdot P_4 \\ a_2 &= a_{20} + a_{21} \cdot P_1 + a_{22} \cdot P_2 + a_{23} \cdot P_3 + a_{24} \cdot P_4 \end{aligned}$$

The BSRM takes the information of all measured ACE-FTS $OCS$ mixing ratio data, determines coefficients $a_{00}$ - $a_{24}$ (for the Fourier and Legendre polynomials) that describe the measurements best and thus provides a mixing ratio distribution with no temporal and spatial gaps.
A possible limitation of the BSRM is the existence of too many data gaps: if there are too many data gaps in the data set that is used as input to the BSRM, the regression model is not able to fit the Fourier and Legendre expansions properly, and this can lead to unrealistic fit coefficients (Hassler, 2009). Especially ACE-FTS, as a solar occultation spectrometer with only 30 measurements per day, exhibits large data gaps compared to other satellite products (e.g. MIPAS). This leads to large data gaps in specific regions (as seen in Figure 2.1) so that it is assumed that those gaps limit the performance of the BSRM.

### 2.2.3 The BSRM performance with the OCS ACE-FTS data set

The numbers of Fourier and Legendre terms can be chosen individually for the specific tasks and substance and constrain the possible output distribution. Figures 2.3a, c, e and Figure 2.4 show examples of the BSRM output for four different choices of Fourier and Legendre expansions. The higher the chosen number of Fourier terms, the higher the temporal and latitudinal variability of the BSRM output distribution. Using 1 Fourier and 1 Legendre expansion is presented in Figure 2.3a and exhibits an annual cycle but not enough latitudinal variability. Therefore, the choice of 1 Fourier and 1 Legendre expansions does not represent the observed ACE-FTS $OCS$ values in the altitude range 15.5 - 16.5 km well enough. In Figure 2.3c, the choice of 4 Fourier and 1 Legendre shows multiple minima and maxima throughout the year and the same insufficient latitudinal variability as see in Figure 2.3a. The use of 4 Fourier and 4 Legendre expansions looks much more like the annual $OCS$ mixing ratio distribution observed at 15.5 - 16.5 km altitude, higher mixing ratios in the tropics, lower mixing ratios closer to the poles. The difference between the BSRM output distribution in Figures 2.3a, c and e, and the original ACE-FTS $OCS$ data set (for all measured years in the altitude range 15.5 - 16.5 km), is shown in Figures 2.3b, d and f (respectively to Figures 2.3a, c and e). It was investigated that using two Legendre terms or higher ($\sim 10$), does not significantly change the result. The mean of the absolute values of the

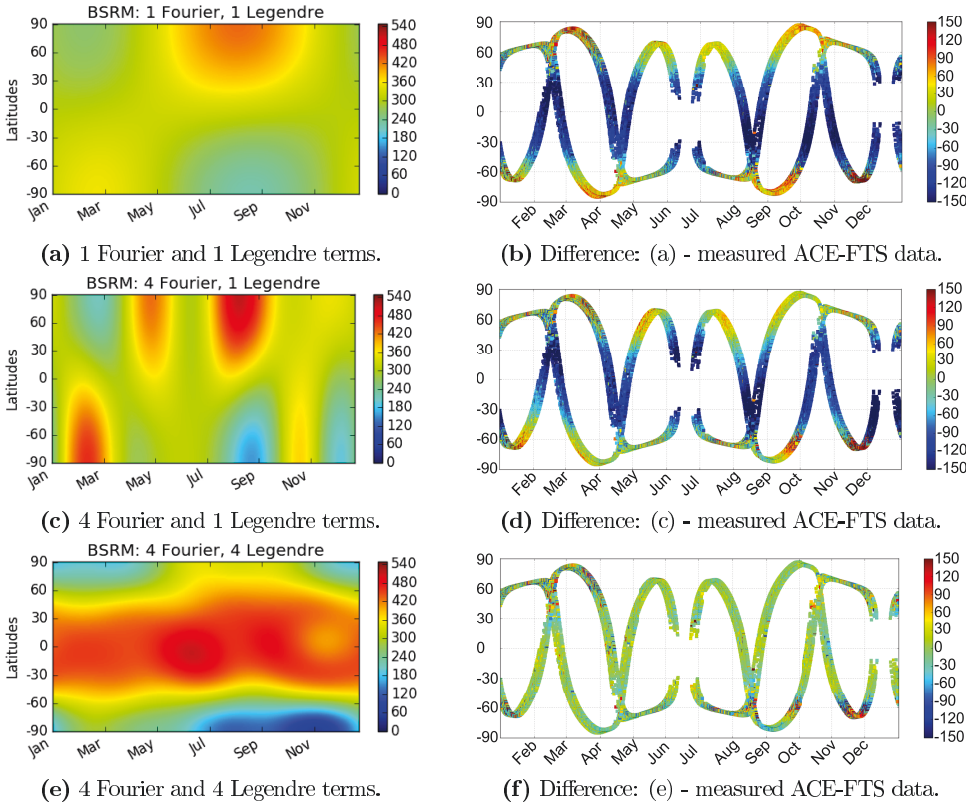


**(a)** 1 Fourier and 1 Legendre terms.

**(b)** Difference: (a) - measured ACE-FTS data.

**(c)** 4 Fourier and 1 Legendre terms.

**(d)** Difference: (c) - measured ACE-FTS data.

**(e)** 4 Fourier and 4 Legendre terms.

**(f)** Difference: (e) - measured ACE-FTS data.

**Figure 2.3:** A comparison of the BSRM output distribution of *OCS* mixing ratios in ppt in (a), (c) and (e), using different numbers of Legendre and Fourier terms and the respective difference plots between the BSRM output fit and the ACE-FTS *OCS* dataset in (b), (d) and (f) (15.5 - 16.5 km altitude).

difference between the BSRM output and the ACE-FTS measurements is 37.3 ppt when using 10 Legendre expansions and 41.2 ppt, when using 2, respectively. A comparison between the BSRM output and the ACE-FTS *OCS* measured data distribution determines which numbers of Fourier and Legendre terms are chosen for the correction procedure. The difference between the BSRM output distribution and the ACE-FTS measurements at the 15.5 to 16.5 km altitude range, using 1 Fourier and 4 Legendre terms is presented in Figure 2.5 (respective plots for 4 Fourier and 1 Legendre terms, 4 Fourier and 4 Legendre terms and 1 Fourier and 1 Legendre terms are presented in Figure 2.3d, Figure 2.3f and Figure 2.3b). The mean of the absolute values of the displayed differences is an indicator for the performance of the BSRM output distribution. The mean of the absolute differences for the four presented cases are 57.5 ppt (with 4 Fourier and 1 Legendre terms), 66.6 ppt (with 1 Fourier and 1 Legendre terms), 37.5 ppt (with 4 Fourier and 4 Legendre terms) and 38.2 ppt (with 1 Fourier and 4 Legendre terms), which is equivalent to 10 % of the mean global *OCS* ACE-FTS mixing ratio. Although using the BSRM output with 4 Fourier and 4 Legendre terms seems to represent the ACE-FTS *OCS* data set best (with a lowest value of the mean of the absolute differences), a high variability is noted in the tropics in the output distribution in Figure 2.3f. Especially in seasons with no ACE-FTS measurements, minima and maxima appear in the BSRM output distribution. Taking into account our knowledge of atmospheric dynamics and *OCS* distribution, the best regression fit was found to be using one Fourier (representing an annual cycle) and four Legendre expansions. The regression results describe the measured ACE-FTS data set best in the tropics, where the ACE-FTS latitudinal coverage is the densest. In the polar regions in November/December the model over- and underestimates the ACE-FTS data (-100 ppt to +100 ppt difference). In this region ACE-FTS *OCS* point to point measurements vary on a day to day basis. The day to day variability at 60° to 90°S in the month of November is more than 50 % higher than the variability observed in the reference month April. For the example year 2015, the standard deviation of the *OCS* mixing ratios at 15.5 - 16.5 km altitude, 60° to 90°S in November is 88 ppt, the respective standard deviation in April is 40.8 ppt. This high day to day variability observed during the southern polar vortex could be caused by retrieval artifacts at very low temperatures and therefore, cannot be well represented by the BSRM fit. Lower mixing ratio values in the southern latitudes in the BSRM output distribution in Figure 2.4 from July to December point to a reasonable representation of the southern polar vortex.

With the BSRM, a smooth periodic surface is fitted to the ACE-FTS *OCS* data. Atmospheric dynamics and transport processes are not considered in the BSRM. The BSRM is not based on an atmospheric model, but rather a 2-D fit, best describing the data. The large scale coverage of the model, including the ACE-FTS annual information from 12 years of measurements, is used to correct mean mixing ratio and budget values of a chosen latitude and time frame for the sampling bias. The BSRM output, using 1 Fourier and 4 Legendre terms is used for the sampling bias correction procedure, described in Chapter 2.2.4.

Not only the mixing ratio values of the *OCS* ACE-FTS dataset, but especially the stratospheric seasonal burden values are of interest. Therefore, the BSRM modification procedure (described in Chapter 2.2.4) is also applied to the calculated stratospheric *OCS* burden values. Figure 2.6 presents the model performance for the burden application. The ACE-FTS stratospheric *OCS* burden values of all years are displayed in Figure 2.6b. Lower burden values appear in the tropics and higher values closer to the poles. As for the *OCS* mixing ratio distribution at 15.5 - 16.5 km altitude, using 1 Fourier and 4 Legendre expansions was also found to yield the best BSRM output performance for the stratospheric burden distribution. The BSRM stratospheric burden distribution is displayed in Figure 2.6a. Even though it is not so clearly seen in the real ACE-FTS dataset in Figure 2.6b, the southern polar vortex is represented in the model output, with lower burden values during June to October close to the poles. The difference between the BSRM output and the burden calculated from the ACE-FTS data set, is shown in Figure 2.6c. As seen in Figure 2.6c the model performance is best close to the equator, with differences between the BSRM output and the ACE-FTS *OCS* data of around 0. In the tropics the tropopause and therefore the stratospheric *OCS* burden show the lowest variability throughout the year and the best ACE-FTS data coverage.
With the high variability in the stratospheric budget data, particularly close to the poles, the BSRM fit cannot produce a fit that represents and accounts for variability and gradients well enough. The high variability is not an annual repeating atmospheric feature, but rather caused by a moment to moment variability of the ECMWF dynamical tropopause height.
In Chapter 2.3.1 the application of the BSRM to stratospheric burden calculations is presented.

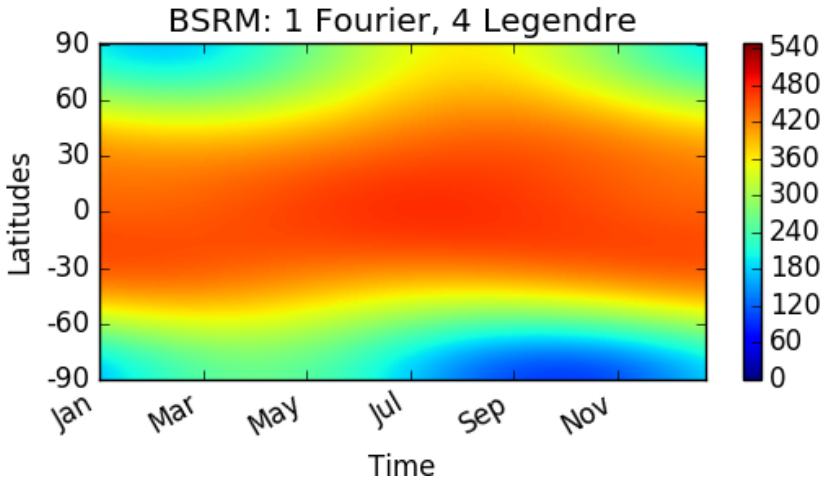


**Figure 2.4:** BSRM output, using 1 Fourier and 4 Legendre terms, chosen for the correction procedure. OCS mixing ratios in ppt, at an altitude range of 15.5 - 16.5 km.

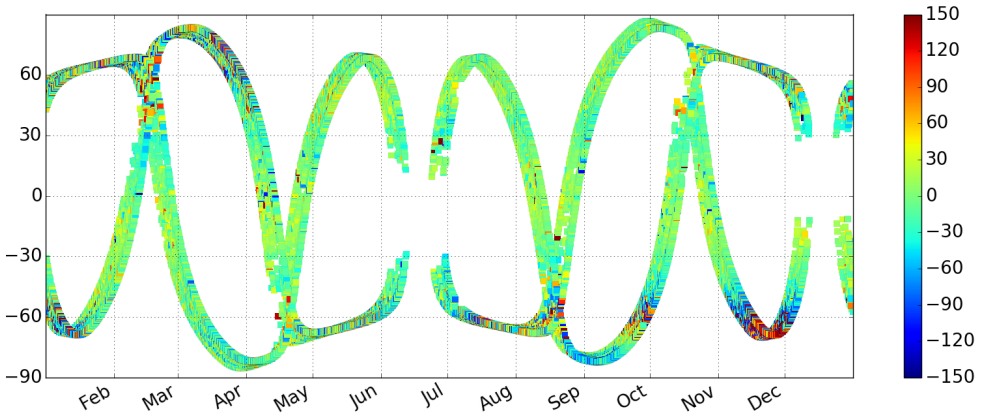


**Figure 2.5:** The difference between the BSRM output fit and the ACE-FTS *OCS* dataset in ppt (15.5 - 16.5 km altitude).

### 2.2.4 Sampling bias correction procedure

The correction procedure for shifting the ACE-FTS data to account for the sampling bias to calculate a certain budget or mean concentration at chosen times, latitudes and heights, is presented below and visualized in Figure 2.7. The procedure can be applied to any latitude/longitude/altitude/time frame. Here, two examples are chosen and further presented: one at 30 - 60°N for JJA (red box) and one for 60 to 90°S for DJF (black box), each at an altitude range from 15.5 to 16.5 km.

1. A well represented global picture from the BSRM needs a measurement data set that is as dense as possible. Therefore, all available ACE-FTS *OCS* data from 12 years from a chosen altitude range are assembled in one year, to give the best possible representation of the annual *OCS* distribution (Figure 2.7a).
   Comparing Figure 2.7a and Figure 2.1 shows that the annual latitudinal coverage of ACE-FTS is not exactly the same each year, but is slightly shifted. Hence, it makes sense to use all ACE-FTS years combined in one data set over the seasons of one year, to form a picture, as dense as possible, as the input for the BSRM. The red and black boxes in Figure 2.7 present the chosen time and latitude frames, used for the application of this process.

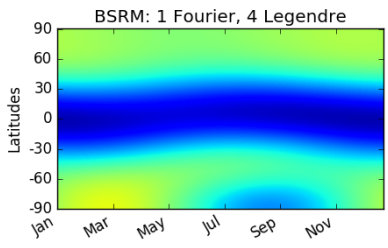


**(a)** BSRM output distribution

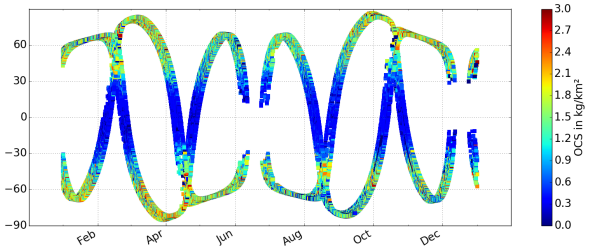


**(b)** Calculated burden values from the ACE-FTS data set.

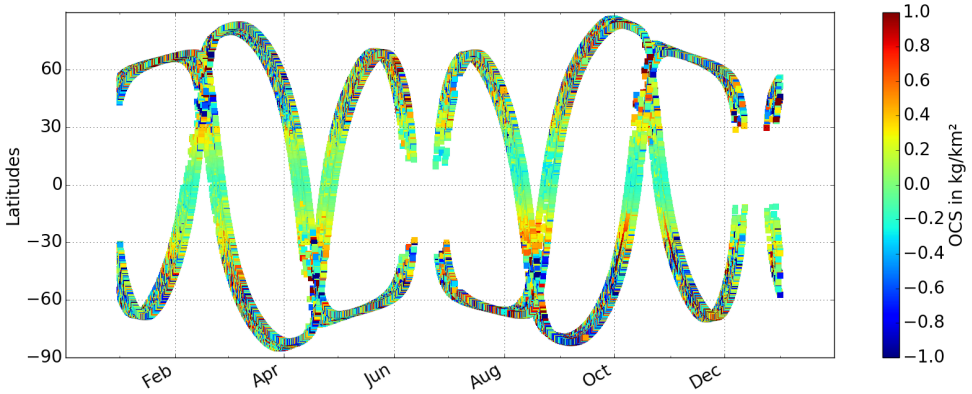


**(c)** The difference between the stratospheric $OCS$ burden from the BSRM output fit and the ACE-FTS dataset (a - b).

**Figure 2.6:** BSRM output distribution performance of $OCS$ in kg/m$^2$, using the calculations of the stratospheric (using the ECMWF dynamical tropopause height) $OCS$ burden.

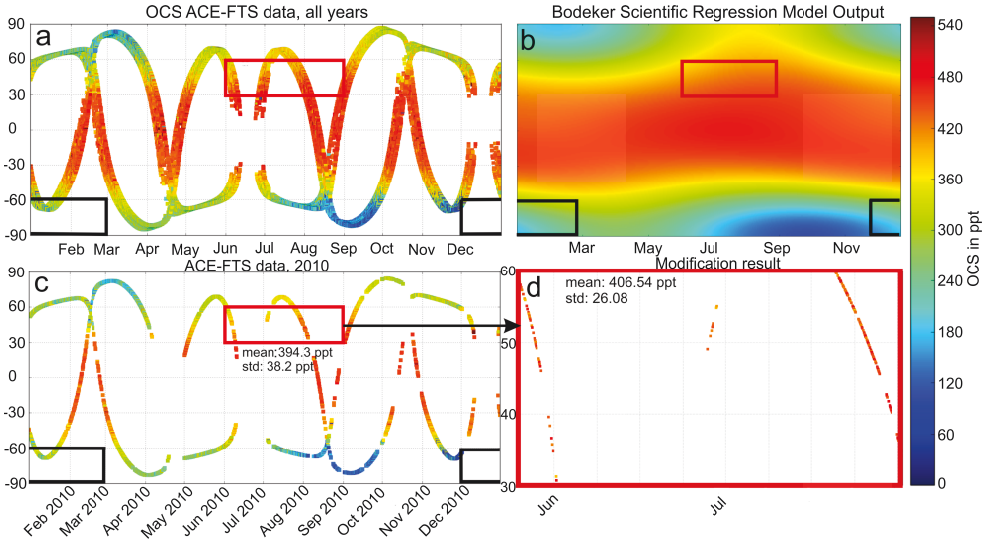


**Figure 2.7:** Schematic explanation of how the sampling bias is accounted for mean mixing ratio (or budget) calculations of any chosen time/latitude/altitude range. Two examples are further analyzed, indicated by the red and black boxes. (a) is a combination of all ACE-FTS measurements (2004 - 2016) in one year. (b) shows the BSRM fit to the ACE-FTS data. (c) represents the ACE-FTS measurements throughout the year 2010. (d) shows the modified dataset, after the correction procedure for the red example box.

2. All *OCS* ACE-FTS data from step 1 are used in the BSRM to create a global *OCS* distribution, presented in Figure 2.7b, filling the measurement gaps, which are a result of the ACE-FTS sampling pattern. From this regression model fit, the desired, respective time frames and latitudinal ranges during one year (red and black boxes) are extracted and a mean value of all values inside the box for the altitude range 15.5 - 16.5 km is taken.

3. ACE-FTS data are extracted for the chosen time frame and latitude band for the planned analysis (red box: 30 - 60°N, JJA, 2010), as seen in Figure 2.7c.

4. The exact spatial and temporal information of the ACE-FTS measurements is extracted from Figure 2.7c (here for the year 2010) and the mixing ratio values at the exact same latitudes and time during the year are taken from the regression model results, which represents the *OCS* mixing ratio distribution for all years (Figure 2.7b).

5. In effect, each single ACE-FTS measurement point (per measured profile) is modified, using this procedure. Equation 2.2 is used to modify each point.

$$ACE_{mod} = ACE_{MEASpoints} \cdot \frac{Model_{MEAN}}{MODEL_{ACEpoints}} \tag{2.2}$$

$ACE_{MEASpoints}$: the ACE-FTS measurements of the chosen period, latitude band and height

$Model_{MEAN}$: the mean value of the BSRM fit of the chosen latitude band and season.

$MODEL_{ACEpoints}$: the regression results at the locations of the ACE-FTS measurements.

Each ACE-FTS measurement point is multiplied by a factor, considering the one mean value of the chosen spatial and temporal region and the respective regression result at the ACE-FTS measurement location. Consequently, each point is shifted towards the mean value of the box. Figure 2.7d presents the 'modified' ACE-FTS data set for the chosen example. However, it should be noted that only the calculation of the mean mixing ratio (or budget) of all data points in the red box is corrected towards the sampling bias, not the single data points (i.e. the mean value of all $ACE_{mod}$ from the red box, is now corrected for the sampling bias).

### 2.2.5 Evaluation of the correction procedure

Figure 2.8 visualizes the distribution of the ACE-FTS *OCS* mixing ratio data, for the 2004 - 2016 period for the respective chosen seasons (DJF at 60 to 90°S and JJA at 30 to 60°N) with histograms. The green histogram in the background represents the value distribution of all ACE-FTS measurements for the chosen criteria, the blue histogram the data distribution of the ACE-FTS data that were adjusted with the BSRM output data set, referred to as 'modified'. The shifts in standard deviation and mean values between the green and blue histograms are an indicator on how the described method affects the ACE-FTS data.

Figure 2.8a represents the data distribution for DJF of all 12 years of ACE-FTS data, for the latitudes 60 - 90°S, which is presented in Figure 2.7 as a black box. This example was chosen, because it shows the clearest shift in mean *OCS* mixing ratios between the 'modified' dataset and the original ACE-FTS data. The mean *OCS* mixing ratio value for the 'modified' data set (265 ppt) is 28 ppt lower than for the actual ACE-FTS data set (293 ppt). The standard deviation for the 'modified' data set decreased by 7.2 ppt (= 11 %). The decrease of the mean value is understood: The latitude band from 60 to 90 °S shows that ACE-FTS exhibits large measurement gaps towards the south (especially in DJF). Following the global distribution of *OCS* (Barkley et al., 2008), mixing ratios decrease with altitude and latitude. It is therefore expected that the ACE-FTS measurement gaps exhibit lower *OCS* mixing ratios at a specific altitude (here 15.5 - 16.5 km), which lower the total mean. Therefore, the clear shift of the mean value, seen in Figure 2.8a is real, as expected.

The histograms in Figure 2.8b show the data distribution for the red box in Figure 2.7, JJA, 30 - 60°N. This example was chosen, because of the clear decrease in standard deviation of the 'modified' data set. The mean value of the original ACE-FTS *OCS* data is 412 ppt and is shifted by 6 ppt (1.5 %) for the 'modified' version (418 ppt). All latitudes of the chosen range (30 -

60°N) are covered so that the measured ACE-FTS data in this example (red box in Figure 2.7) represent the whole area much better, than for the previous example (black box in Figure 2.7). The standard deviation is decreased by 32 % for the 'modified' version. Following Equation 2.2, it becomes evident that each measurement point is shifted towards the BSRM mean value for the chosen box. Hence, it is expected that the standard deviation decreases with the correction procedure.

### 2.2.6 Comparison with MIPAS

To investigate, whether or not the calculated magnitude of the sampling bias is realistic, a comparison is made with a satellite data product with a much denser latitude sampling coverage, the Michelson Interferometer for Passive Atmospheric Sounding (MIPAS).
MIPAS is a mid-infrared spectrometer, on board of the ESA (European Space Agency) satellite ENVISAT and operated from 2002 - 2012, measuring multiple trace gases, including *OCS*. It is a limb sounding instrument, scanning across the horizon, measuring atmospheric spectral radiances, emitted by the atmosphere. MIPAS covers the spectral region between 685 - 2410 $cm^{-1}$ (4.1 - 14.6 $\mu$m), at a spectral resolution of 0.025 $cm^{-1}$ (from 2002 - 2004) and 0.065 $cm^{-1}$ (2005 - 2012) (Fischer et al., 2008). The vertical resolution is around 3 km, with an altitude coverage above the clouds ($\sim$ 5 - 150 km) and a horizontal resolution of 300 km. With a horizontal sampling of $\sim$ 150 km, MIPAS has a much denser global coverage than ACE-FTS. The occurring sampling bias with MIPAS is shown in Figure 2.9 and is much lower and negligible compared to ACE-FTS (seen in Figure 2.2).
The magnitude of the sampling bias for all ACE-FTS years DJF, 60°S to 90°S is analyzed in Chapter 2.2.5. The mean value of the modified data set was found to be 10 % lower than the mean value from the original ACE-FTS data. With the MIPAS data set from December 2009 to February 2010, a similar study is made. Figure 2.10 shows MIPAS data for DJF 2009 - 2010 from 60°S to 90°S for the altitude range 15.5 - 16.5 km, with two standardized histograms: the blue histogram represents all MIPAS data for the chosen time and latitude frame, the green histogram represents the measured MIPAS data for an equivalent time and latitude frame, as detected with ACE-FTS. The difference between the mean values of both histograms is 46 ppt, equivalent to a relative deviation of $\sim$ 11 %. This is in good agreement with the relative deviation found between the ACE-FTS data set and the modified data set (10 %) in the same chosen time and latitude range. This gives confidence for the applied correction procedure.
The ACE-FTS mean value is 115 ppt (28 %) lower than the mean value of MIPAS. A similar difference between MIPAS and ACE-FTS *OCS* measurements has already been observed in Glatthor et al. (2017) and was found to be highest at 14 km altitude, with 75 - 100 ppt difference.

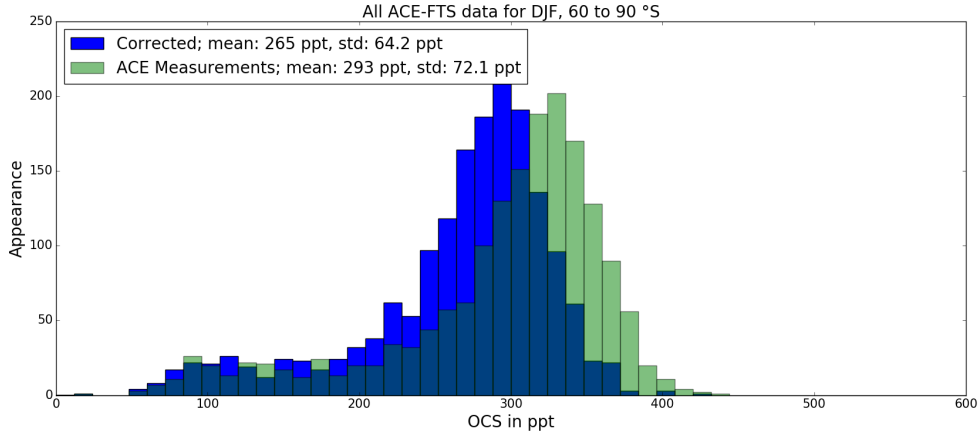


**(a)** DJF, 60 - 90°S; black box from Figure 2.7

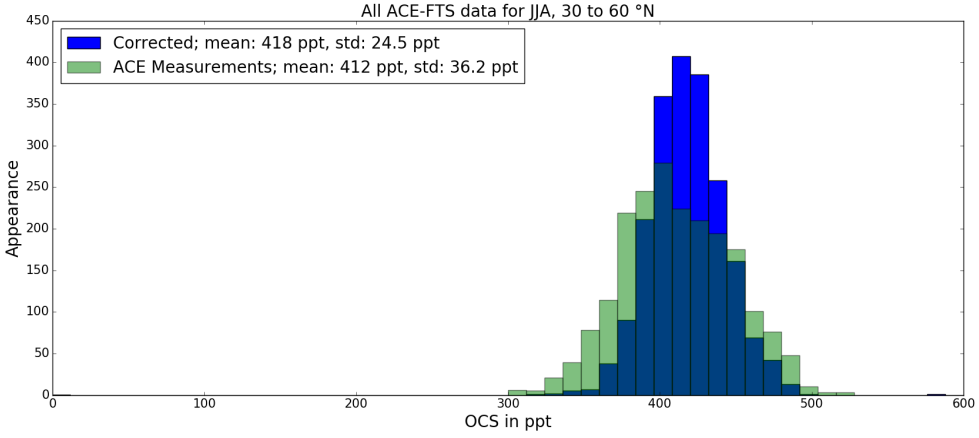


**(b)** JJA, 30 - 60°N; red box from Figure 2.7

**Figure 2.8:** A comparison between the standard deviation and mean values of the measured *OCS* data and the 'modified' data, for the same chosen criteria as indicated with the black and red boxes in Figure 2.7 for DJF and JJA and all 12 years of ACE-FTS data. The green bars represent the *OCS* mixing ratio distribution (at 15.5 - 16.5 km altitude) from the ACE-FTS measurements, the blue bars represent the data distribution after applying the correction procedure.

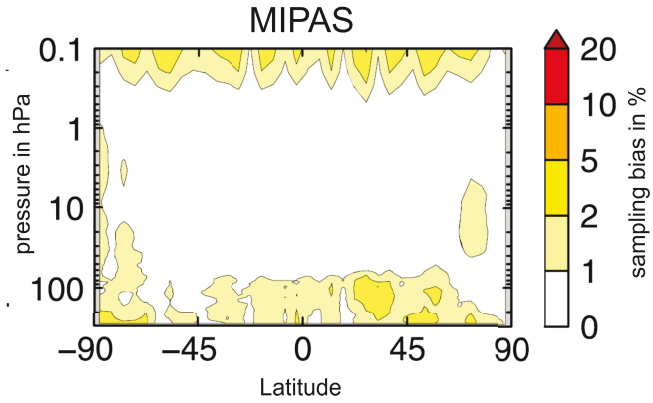


**Figure 2.9:** Latitude height plot of the 12 monthly root-mean-square (RMS) of the sampling bias for the example of $O_3$ in percent for the sampling pattern of MIPAS, from Toohey et al. (2013). The equivalent illustration for ACE-FTS is seen in Figure 2.2.

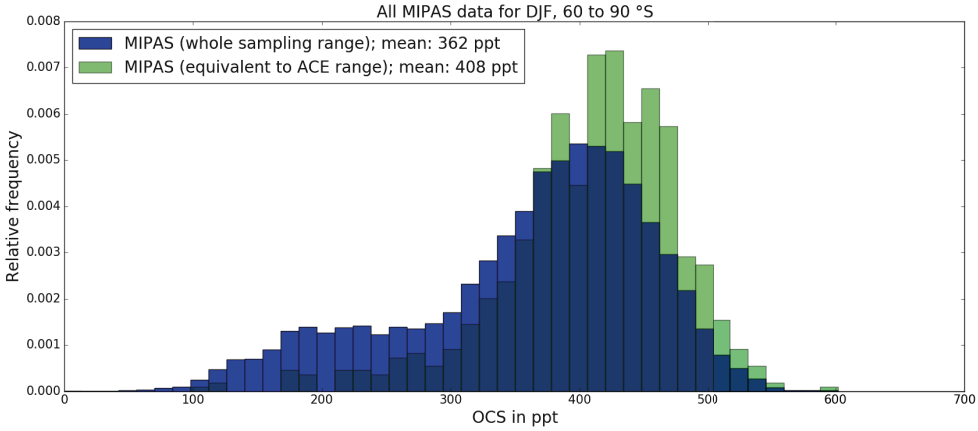


**Figure 2.10:** Standardized histograms, demonstrating the MIPAS data distribution for DJF 2009 - 2010, 60°S to 90°S, for all available MIPAS measurement profiles (blue) and for MIPAS measurement profiles in a comparable latitude and time frame as ACE-FTS measurements. The respective ACE-FTS plot, considering all years during DJF of ACE-FTS (to establish a reasonable statistic) is shown in Figure 2.8a.

## 2.3 OCS burden

### 2.3.1 Seasonal and zonal variations

For the available time period of the ACE-FTS *OCS* data set a possible trend and seasonal variability of the stratospheric *OCS* burden was investigated. Figure 2.11 shows the calculated *OCS* stratospheric burden, using the dynamical tropopause (for further explanation of the selection criteria see Chapter 2.3.2). The 'correction' procedure (described in Chapter 2.2.4) towards the sampling bias was applied, represented by the red crosses. The blue crosses represent the stratospheric *OCS* burden calculations from the ACE-FTS data set without bias correction. In Figure 2.11, each point represents the zonally averaged stratospheric *OCS* burden (kg/km$^2$) over all longitudes, per season (MAM, JJA, SON, DJF) in the respective 30° latitude band. Almost all seasons and 30° latitude bands exhibit data points allowing *OCS* burden calculations (in theory only one data point per season is sufficient for a burden calculation).
Generally, the stratospheric burden values are lower in the tropics and higher at the poles. At the poles the tropopause is much lower and altitude ranges with higher pressures are considered for the budget calculations, resulting in increasing stratospheric columns towards the poles.
Close to the equator no seasonal cycle in stratospheric, seasonal *OCS* burden is observed. The highest seasonal variation in stratospheric *OCS* burden is seen between 60 - 90°S. Seasonal dependencies are expected to be dominated by tropopause height variations, c.f. Chapter 2.3.2. However, there is another explanation for a higher seasonal cycle at the poles: At the winter pole (e.g. JJA in the SH), the upper branch of the Brewer-Dobson Circulation (BDC) transports more air masses descending towards the poles than the lower branch. This means that air masses with a higher mean age of air are detected at the poles. *OCS* mixing ratios decrease with time; thus a lower *OCS* mixing ratio is expected with a higher mean age of air of *OCS* at the winter pole in the stratosphere. During winter, the stronger polar vortex in the Southern Hemisphere enhances the descent of more *OCS* depleted air masses at the pole and therefore the seasonal effect is stronger in the SH than in the NH.
For the majority of points, from 60°N to 60°S the modification with the BSRM towards the sampling bias has only a minimal effect and is within the measurement uncertainty, calculated using the ACE-FTS species error data set. The given species error from the ACE-FTS data set is a pure statistical error for the species retrieval from the fitting process and is between 1 and 3 %. The small difference between the modified burden values and the values calculated from the ACE-FTS data set in the tropics is due to the better latitudinal coverage and also lower stratospheric column variability throughout the year. However, the region close to the poles (polewards 85°S and 85°N) is never covered by the ACE-FTS dataset. Since the tropopause is lowest over the poles, higher resulting burden columns are observed.

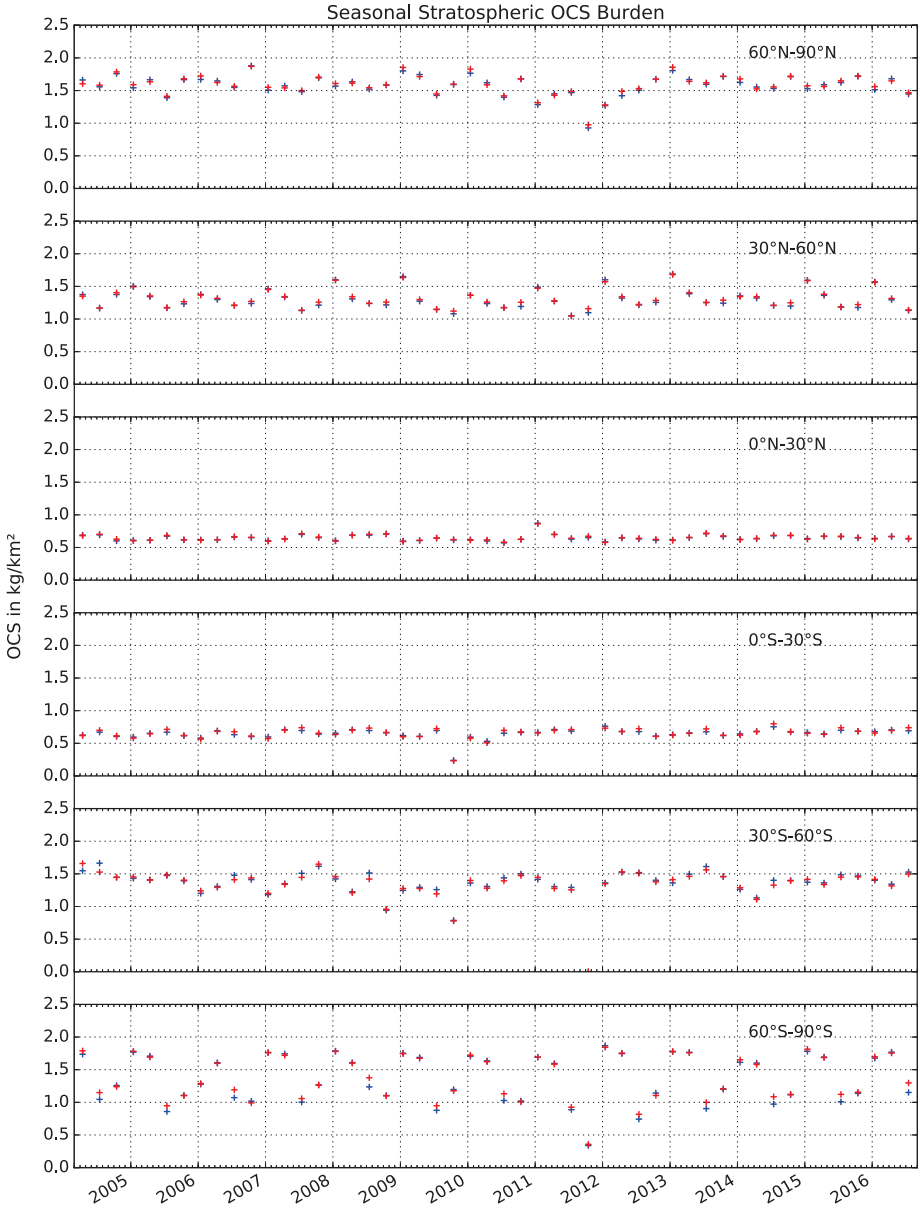


**Figure 2.11:** Seasonal stratospheric *OCS* burden (in kg/km$^2$) for the available ACE-FTS time frame 2004 - 2016, calculated using the ECMWF dynamical tropopause (blue points). The burden correction values are indicated in red.

Because in the original ACE-FTS data set, exactly the higher burden columns (closer to the poles) are missing in the 30° latitude band burden calculations, the real stratospheric $OCS$ budget values are expected to be higher. This would therefore result in a positive shift in stratospheric $OCS$ burden in the 60 - 90° latitude band. Most of the red points in Figure 2.11 in the 60 - 90°S bin are higher compared to the (original) blue points. However, the differences are within the ACE-FTS measurement sensitivity.
No statistical significant long-term trend of stratospheric $OCS$ burden is seen with the ACE-FTS burden values and also the burden values corrected for the sampling bias (with a calculated probability test). However, this is in disagreement with Kremser et al. (2015), who detect a significant positive trend in $OCS$ column at three different sites in the Southern Hemisphere.
There is only a small shift between the sampling bias corrected burden calculations and the burden values without the correction. Hence, although the sampling bias has been corrected for, scientific conclusions and analysis do not change. Possible weaknesses in the representation of the BSRM output distribution, have no significant impact on the scientific outcome.
For a quantification of the contribution of $OCS$ to the stratospheric sulfur budget, the sulfur content of $OCS$ is of interest. The stratospheric sulfur burden from $OCS$ is a simple multiplication of the $OCS$ burden values by the factor 0.534, according to the atomic weight of Oxygen, Carbon and Sulfur and is presented in Figure 2.12. In Figure 2.12 the seasonal stratospheric sulfur burden from $OCS$, calculated with the MIPAS and ACE-FTS data set, is shown. To be consistent, only seasonal burden points are shown from MIPAS, with measurements throughout the whole respective season. MIPAS sulfur burden values are consistently larger by $\sim$ 28 % in the 60°S to 90°S bin (lowest panel) and higher by $\sim$ 15 % around the equator. The low bias of ACE-FTS (or high bias of MIPAS) have already been observed in Chapter 2.2.6 with the same magnitude of 28 % in the south. Seasonal variations closer to the poles, are observed with both instruments, but stronger variations are observed with the ACE-FTS data set. MIPAS and ACE-FTS sulfur seasonal burden calculations are in good agreement with the systematic positive shift of the MIPAS data.

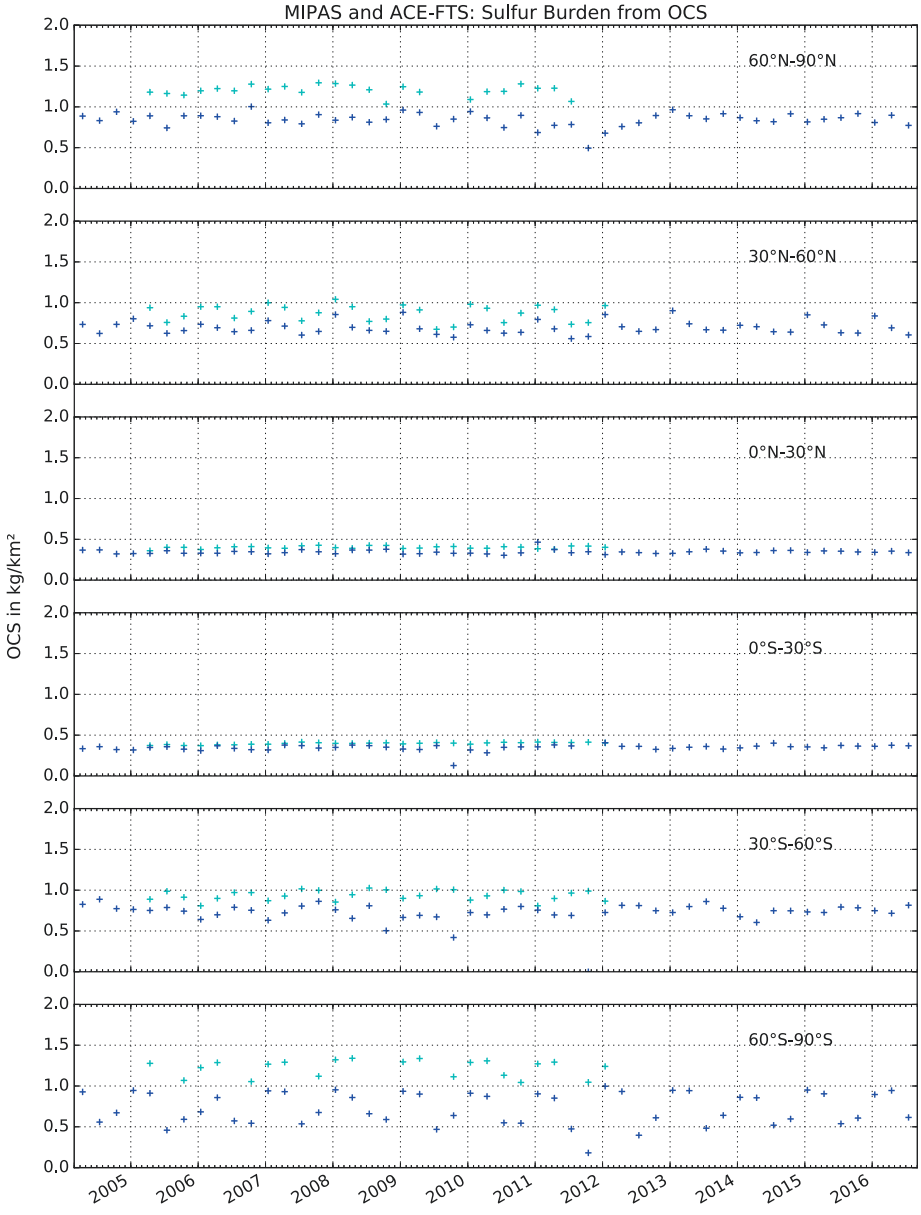


**Figure 2.12:** Seasonal stratospheric Sulfur burden from $OCS$ (in kg/km$^2$) for the available ACE-FTS time frame 2004 - 2016 (blue), and the respective available MIPAS seasonal burden data (cyan), presented in 30° latitude bins from 60 - 90°N on the top to 60 - 90°S on the bottom.

### 2.3.2 Tropopause effects

For stratospheric $OCS$ burden calculations only data above the tropopause are considered, therefore a definition for the tropopause is necessary, which can result in different burden calculations. The thermal tropopause is the easiest definition to bring into use, because it is a clear temperature defined altitude that is easily calculated with the provided ACE-FTS data set. However, the dynamical tropopause considers the dynamics of an air parcel and represents the transport barrier best. For the definitions of the different tropopauses see Chapter 1.1. In the following both tropopause definitions (dynamical and thermal) are compared.
With temperature and pressure values, given from ACE-FTS, the thermal tropopause was calculated and compared with the ERA-interim ECMWF thermal tropopause. In the ACE-FTS retrieval $CO_2$ is analyzed to determine temperature and pressure values (Boone et al., 2005). Figure 2.13 shows the thermal tropopause calculated with ACE-FTS, the ECMWF thermal tropopause and the ECMWF dynamical tropopause averaged over the year 2012.
The thermal tropopause and the dynamical tropopause have been compared and investigated, to quantify the suitability and differences of both tropopause definitions for stratospheric burden calculations. Especially in the Southern Hemisphere the thermal tropopause is located $\sim$ 2 km above the dynamical tropopause (Figure 2.13).

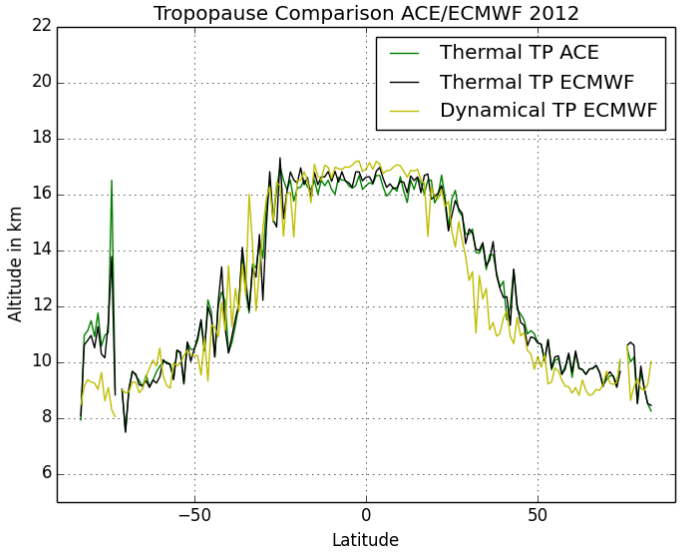


**Figure 2.13:** Comparison between the calculated thermal tropopause using the ACE-FTS dataset, the ECMWF thermal tropopause and the ECMWF dynamical tropopause.

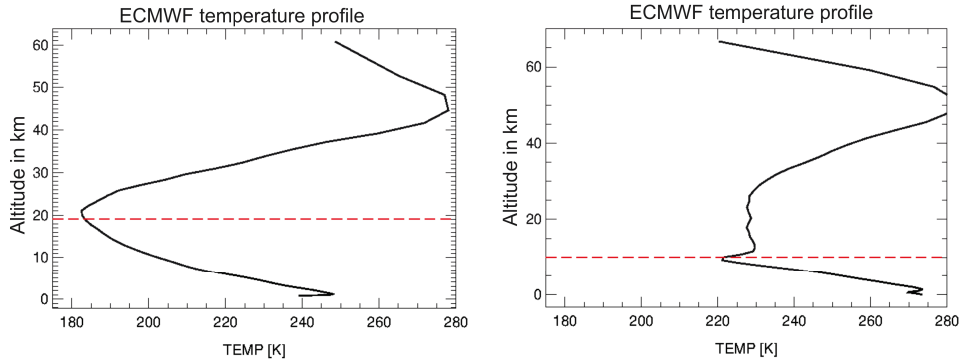


**(a)** False determination: 76°S, 173°E.

**(b)** Correct determination: 60°S, 0°E.

**Figure 2.14:** ECMWF thermal tropopause determination (red) and temperature profile (black) for two chosen cases from August $15^{th}$ 2012.

Such high tropopause altitudes lead to an underestimated stratospheric burden and are thought to represent the transport barrier not as well as the dynamical tropopause height. It becomes evident that the use of the thermal tropopause for stratospheric burden calculations is not suitable. Figure 2.14 shows two examples of ECMWF temperature profiles in high latitudes in the Southern Hemisphere, together with the given ECMWF thermal tropopause height. The strong overestimation of the tropopause using the WMO criteria is associated with the polar vortex. While in Figure 2.14b the tropopause definition seems plausible, Figure 2.14a shows an example where the WMO criteria clearly yields a much higher tropopause altitude than expected, due to the polar vortex.

Seasonal oscillations of the stratospheric $OCS$ burden as shown in Figure 2.15 (especially at 90°S - 60°S), using the thermal tropopause, are dominated by variations of the tropopause height. The higher the tropopause, the lower the $OCS$ stratospheric burden estimation. The lower values (JJA and SON, southern hemispheric winter and spring) of the burden calculation, using the thermal tropopause definition (in red), are repeatedly lower each year by $\sim 0.5$ mg/m$^2$ as compared to data obtained with the dynamical tropopause definition (in green), seen in Figure 2.15, due to the high thermal tropopause during the southern polar vortex. Because it is assumed that the definition of the dynamical tropopause represents the transport barrier better than the thermal tropopause, it is expected that an under- and overestimation of the tropopause and the stratospheric column burden does not occur using the ECMWF dynamical tropopause. Hence, in this work the ECMWF dynamical definition of the tropopause was used for burden calculations (section 2.3.3).

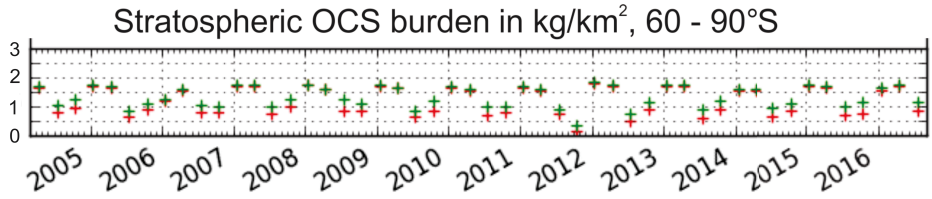


**Figure 2.15:** A comparison for the stratospheric $OCS$ burden calculations, using the thermal tropopause (in red) and the dynamical tropopause definition (in green).

### 2.3.3 Stratospheric global OCS burden

Figure 2.16 shows the $OCS$ mixing ratio distribution of the whole year of 2015 per latitude and altitude. All latitudes from 82°S to 83°N are covered. The ECMWF, ERA-interim dynamical tropopause is indicated with the black line, surrounded by the mean standard deviation of the whole year 2015 per latitude in green. The dynamical tropopause is lowest over the poles (at around 9 km) and highest in the tropics (at around 16 km). The mean of the visible standard deviation for all latitudes in Figure 2.16 for the whole year 2015 is 2.9 km. Decreasing $OCS$ mixing ratios with stratospheric age (increasing altitude and latitude) are detected, as already reported in Barkley et al. (2008). In the well mixed troposphere, $OCS$ mixing ratios are relatively constant at around 500 ppt. Concentrations decrease in the stratosphere, where higher UV radiation foster photochemical conversion to $H_2SO_4$. Sources and sinks of $OCS$ are discussed in Chapter 1.2.2. However, a stratospheric burden for $OCS$ has not been derived from observations so far.

The total stratospheric $OCS$ burden is calculated with Equation 2.3.

$$OCS_B = \underbrace{\sum_{h>Tp_D}^{50} \sum_{-90<lat<90} (OCS_{strat} \cdot TND) \cdot \underbrace{\frac{60.07 \frac{g}{mol}}{6.02 \cdot 10^{23} mol^{-1}}}_{\text{mass of one OCS molecule in g}} \cdot 10^5 \cdot}_{\text{OCS burden in } \frac{g}{cm^3} \text{ for 1 km height interval}} \underbrace{2\pi \cdot 6360.3km \cdot 10^{5^2} \cdot cos(lat \cdot \frac{\pi}{180}) \cdot \frac{111km}{360} \cdot 360}_{\text{surface area of each 1° latitudinal ring dependent on latitude, the sum over all latitudes gives the complete earths surface.}} \tag{2.3}$$

$lat$: latitude values

$OCS_{strat}$: all $OCS$ mixing ratio values from ACE-FTS above the ECMWF dynamical tropopause height per 1° latitudes x 1° longitudes and 1km altitude boxes at $lat$

$TND$: total number density in $\frac{1}{\text{cm}^3}$ at $lat$.

To estimate the stratospheric $OCS$ burden, all available $OCS$ profiles from ACE-FTS for the respective year are considered. A specific time frame and a specific area (latitudes, longitudes) are chosen in a 1° latitude x 1° longitude grid. For each $OCS$ profile, the ECMWF dynamical tropopause height is rounded and the data below the tropopause excluded. Depending on latitudes, for each vertical profile the burden is calculated considering the size of each profile volume. In case of multiple burden values in one bin, the respective mean value is taken. Missing bins are interpolated and the missing bins close to the poles ($\sim$ 85° - 90°) are extrapolated with the mean value of the closest two bins to the poles, to achieve a global coverage. The sum of all bins represent the total stratospheric burden of each year, presented in Figure 2.17. The annual burden varies by 6 %. As for the seasonal burden, no obvious trend is observed for the annual stratospheric $OCS$ burden. The burden values calculated for the years 2004 and 2016 do not consider the whole year, because the ACE-FTS data set is available from February $23^{rd}$ 2004 to September $28^{th}$ 2016. The presented error in Figure 2.17 is a result of using the so called 'species error' available for each measured substance from the ACE-FTS data set. However, it should be noted that this error is a purely statistical fitting error (assuming a normal distribution of random errors) and does not include any estimate of systematic errors (Toohey et al., 2010).

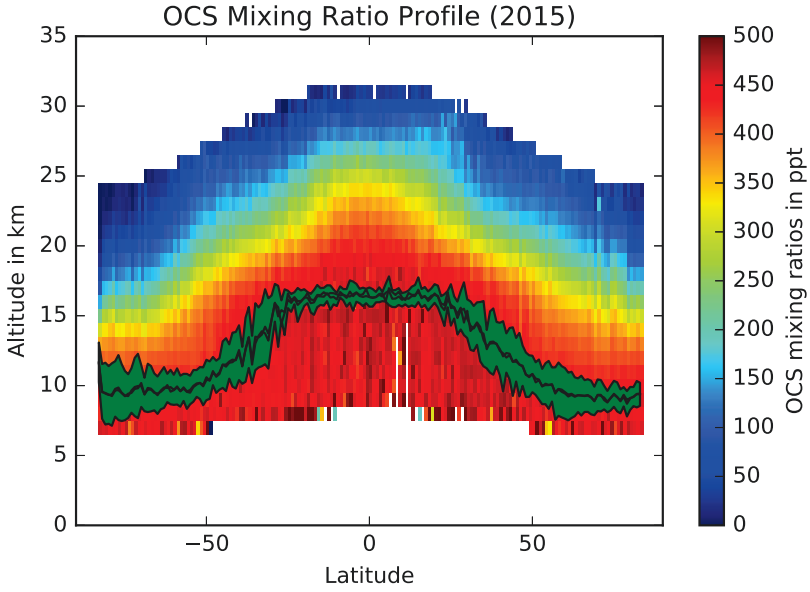


**Figure 2.16:** The $OCS$ mixing ratio latitude, altitude profile for the year 2015. The mean of all profiles along all latitudes from 2015 is taken. In green the ECMWF dynamical tropopause is indicated with standard deviation.

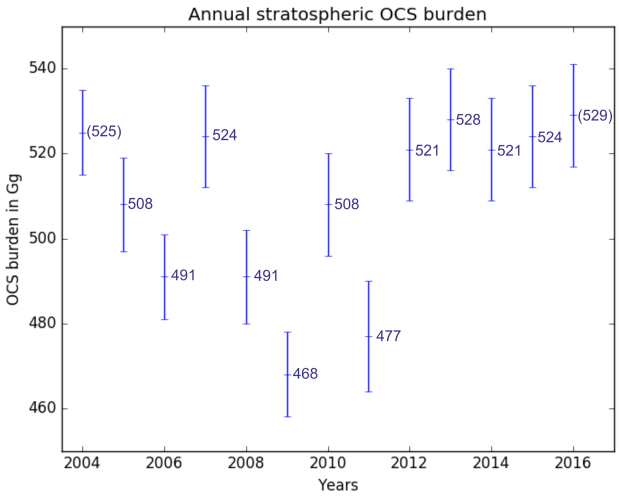


**Figure 2.17:** Annual stratospheric $OCS$ burden values, calculated with the ACE-FTS data set, for the years 2004 - 2016 together with the errors calculated using the 'species error', given by the ACE-FTS data set.

The average stratospheric $OCS$ burden for the year 2015 is 524 Gg, which is equivalent to a sulfur burden from $OCS$ of 280 Gg S. 2015 was chosen as an example year, because it is the last whole available year from the ACE-FTS data set for this work. This value is in excellent agreement with the value 283.1 Gg S from $OCS$ in the stratosphere, given by the recent global sulfur budget model by Sheng et al. (2015). The global $OCS$ distribution seems to be well represented in the model.
The estimate of the total atmospheric $OCS$ burden by Barkley et al. (2008) is 5.34 Tg. Hence, 10 % from the total atmospheric $OCS$ resides in the stratosphere.
Early studies gave a comparable estimate for an atmospheric $OCS$ burden of 5.2 Tg, 4.63 Tg in the troposphere and 0.57 Tg in the stratosphere (9 % higher than what is calculated with the ACE-FTS data set for 2015) (Chin and Davis, 1995).

## 2.4 Asian monsoon

As introduced in Chapter 1.2.1 the Asian monsoon is a significant pathway for tropospheric air into the stratosphere. Due to the isolation in the Asian monsoon anticyclone, tropospheric tracers like $CO$ and $HCN$ show elevated mixing ratios, mixing ratios of stratospheric tracers like $O_3$, $HNO_3$ and $HCl$ are lower, as shown in Park et al. (2008). Figure 2.18 visualizes this enhancement in the Asian monsoon anticyclone with $HCN$ and $CO$ as seen in Park et al. (2008), except with a larger dataset (12 years instead of 3).

As seen in Figure 2.19, $OCS$ mixing ratios are also significantly increased in the Asian monsoon anticyclone (June to August) at 15.5 - 16.6 km altitude. At this altitude range (15.5 - 16.5 km) the mixing ratio increase is best visible and a good comparability to Park et al. (2008) is given. Other than for $CO$ and $HCN$, the gradients in the anticyclone region are not as distinct for $OCS$. This is due to the longer photochemical lifetime of $OCS$, which is much higher than for $HCN$ and $CO$: The tropospheric, photochemical lifetime for $OCS$ is around 36 years (4.63 Tg $OCS$ burden in the troposphere divided by 0.13 Tg/a tropospheric sink (Chin and Davis, 1995)). For $HCN$ the dominant sink is ocean uptake with a tropospheric lifetime of 5 months and stratospheric lifetime of a few years (Li et al., 2009). $CO$ is mainly removed with oxidation of hydroxyl radicals ($OH$) and the lifetime is latitude dependent, with around one month in the tropics and more than 1 year at the poles during winter (Staudt et al., 2001).
Figure 2.18 and Figure 2.19 show that there are noticeable measurement gaps in southeast Asia at 15.5 to 16.5 km altitude during the Asian monsoon season with the ACE-FTS instrument. This is likely due to cloud formation during the Asian monsoon in those heights. A selection of higher altitudes decreases those gaps.
The Asian monsoon anticyclone is supplied with tropospheric and boundary layer air masses. Southeast Asia and northern India were identified to be main source regions for the Asian monsoon anticyclone (Vogel et al., 2015). Two main convection areas at the Tibetan plateau and at the Bay of Bengal are discussed to transport those air masses directly into the Asian monsoon anticyclone (Pan et al. (2016), Park et al. (2009), Fu et al. (2006)). In Bergman et al. (2013) it is discussed that the strong convection at the Bay of Bengal is transported south of the center of the anticyclone and air masses are carried around the Asian monsoon anticyclone at the southern boundary. In this work, an approach was made to explore if this can also be demonstrated with the ACE-FTS dataset: Figure 2.20a shows $OCS$ against $HCN$ in ppt and $CO$ in ppb, respectively. As discussed in Notholt et al. (2003), all three gases are biomass burning tracers. One important difference for further discussion is that $HCN$ has a strong ocean sink, in contrast to $CO$ and $OCS$. Figure 2.20b shows a Potential Vorticity (PV) based border definition of the anticyclone for the year 2011 from Ploeger et al. (2015). This plot is taken as guidance to define areas that are more and less likely to be situated in the Asian monsoon anticyclone during JJA. The colored boxes (green, magenta and black) in Figure 2.20b represent the color coding in Figure 2.20a.

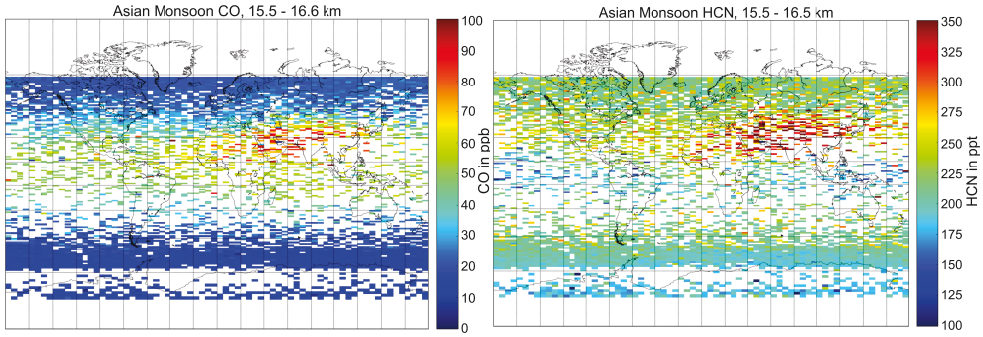


**(a)** CO **(b)** HCN

**Figure 2.18:** A global mixing ratio distribution plot at 15.5 - 16.5 km altitude, showing the enhancement of $CO$ and $HCN$ in the Asian monsoon anticyclone. The plots consider all available ACE-FTS data, during each year in the Asian monsoon time period. Figures like this have already been shown in Park et al. (2008), except here data from the year after 2008 to 2016 are additionally included.

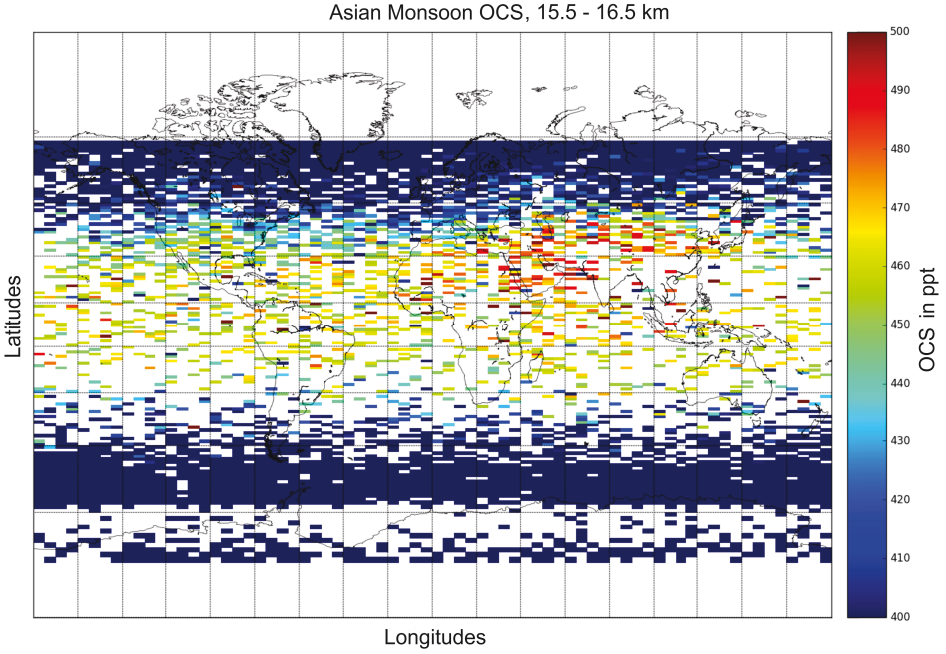


**Figure 2.19:** Averaged $OCS$ mixing ratios during the Asian monsoon season (June to August) from 2004 - 2016 at 15.5 to 16.5 km altitude.

The magenta area represents a region, mostly outside of the anticyclone, on the southern border. The green area is mostly inside and a remaining field is shown in black in the area of the Asian monsoon. The probability of a marine history of the air masses is higher for the Bay of Bengal convection and therefore lower $HCN$ mixing ratios are expected. Hence, if the Bay of Bengal convection is mostly transported outside the isolated anticyclone along the southern border, lower $HCN$ mixing ratios are expected, compared to $OCS$ and $CO$ mixing ratios. From Figure 2.20a it is seen that the magenta triangles for $HCN$ (symbolizing the area on the southern border of the anticyclone) are significantly lower than the other points (and especially the green points from a region closer to the center of the anticyclone). Hence, compared to $OCS$, $HCN$ mixing ratios observed outside on the southern border of the Asian monsoon are lower than inside. This is not observed for the $OCS$ $CO$ dependence. This supports the suggestion that convection originated from the Bay of Bengal is mainly transported outside along the southern border of the Asian monsoon anticyclone.
With the newly developed in-situ instrument AMICA (further discussed in Chapter 3) this correlation between $HCN$, $CO$ and $OCS$ can be further investigated with the measured data from the StratoClim Asian monsoon Campaign phase 2 in Nepal, summer 2017. The high resolution in-situ instrument AMICA, with the possibility of tracing back specific measured air masses, will be able to contribute to the following subjects concerning the Asian monsoon:

- A more precise quantification of the enhanced $OCS$ mixing ratios in the Asian monsoon anticyclone.
- A quantification of biomass burning as a source for $OCS$.
- A better insight into the role of $OCS$ for stratospheric aerosol contribution via an increased understanding of $OCS$ transport (and conversion) processes.
- A better understanding if theory and measurements agree on where the air masses in the Asian monsoon anticyclone originate from.

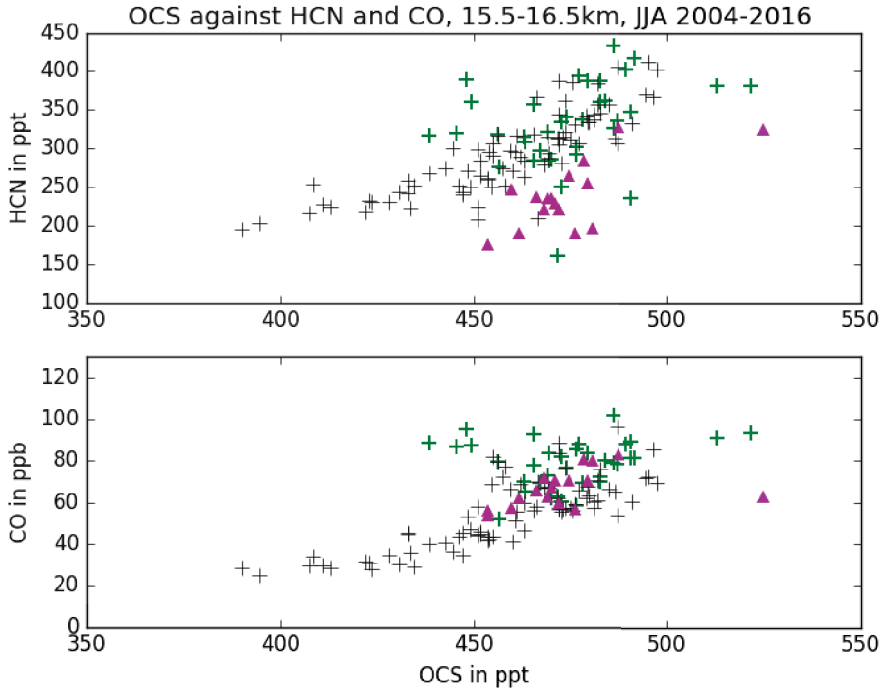


(a)

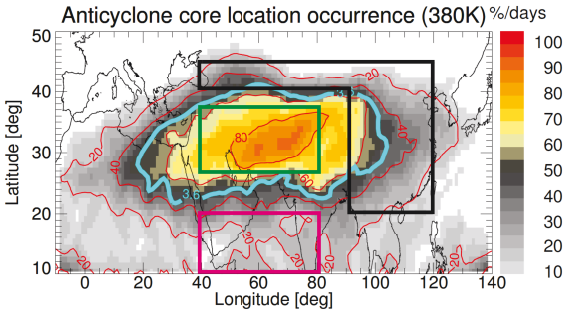


(b)

**Figure 2.20:** Comparison of *CO* and *HCN* mixing ratios to *OCS* inside and at the southern border of the Asian monsoon anticyclone. Figure 2.20a shows all available ACE-FTS *OCS* data (2004 - 2016) for the Asian monsoon period JJA, at 15.5 - 16.5 km altitude. Each point represents a separate 1° latitude x 1° longitude grid box. The rough positions of the points are indicated with colors, explained in Figure 2.20b. The underlying plot in 2.20b, from (Ploeger et al., 2015) presents a PV based Asian monsoon anticyclone structure definition in average for the year 2011. The color boxes illustrate the color choices in 2.20a.

# Chapter 3

# AMICA development

AMICA is the Airborne Mid-Infrared Cavity enhanced Absorption spectrometer. AMICA measures multiple trace gases in the Mid-Infrared region (MIR) with the Integrated Cavity Output Spectroscopy (ICOS) method, yielding high resolution in-situ measurement data. The prototype of AMICA is MICA (Mid-Infrared Cavity enhanced Absorption spectrometer), a ground based instrument using the same measurement technique as AMICA, which performs successful measurements since 2012. Some of the MICA data were used for evaluations in this work. $OCS$ is the main focus of the work presented here. With high resolution in-situ measurements of $OCS$, AMICA has the potential to improve the general understanding of transport processes and $OCS$ conversion processes in the atmosphere. In this Chapter, basics about the IR-absorption spectroscopy and the ICOS method are outlined together with relevant steps for the development and manufacturing of AMICA to its current state, including calibrations and component tests. Additionally, the performance of AMICA during first measurement flights is evaluated.

## 3.1 Infrared spectroscopy

To measure $OCS$ and other gases with absorption spectroscopy, the property of a gas to absorb light at discrete wavelengths, corresponding to distinct energy levels, is used. For absorption spectroscopy, distinct absorption lines of molecules and atoms are used to detect trace gases quantitatively.
A photon, which matches the energy level and therefore wavenumber that is required to move a specific molecule into a 'higher' state, is absorbed by the molecule. The distinct energy that is absorbed, is measured. The energy gained at the molecule, can be released via spontaneous emission of a photon or by collision with other molecules. Molecules can have various degrees of freedom, depending on the number and arrangement of the atoms, which determine their rotational and vibrational features (linear molecules of vibrational modes: $3 \cdot N - 5$ and non-linear molecules: $3 \cdot N - 6$; N: the number of atoms in the molecules; Number 3: each atom has

three degrees of freedom for the x, y and z component; Number 5 and 6: the sum of the rotational and translational modes, 3 reserved for translation and 2 or 3 reserved for the rotational modes). The number of vibrational modes determines the number of transitions possible in the molecule. In this work, spectroscopy in the IR region (vibrational spectroscopy) is performed. The main measurement substance of interest is $OCS$.
$OCS$ is a linear molecule with one oxygen, one carbon and one sulfur atom. Each atom has 3 degrees of freedom (for x, y and z component). $OCS$ exhibits $3 \cdot N - 5 = 4$ principal vibrational modes, all illustrated in Figure 3.1 (symmetric stretch, asymmetric stretch and two degenerate bends). Each vibrational mode is responsible for a number of vibrational states accessible in the IR-region. In this work, a spectrum resulting from the asymmetric stretch (see Figure 3.1) is chosen. The band for the asymmetric stretch of $OCS$, including all $OCS$ lines (and also other relevant gases for atmospheric sciences in this spectral region) is shown in Figure 3.2a.

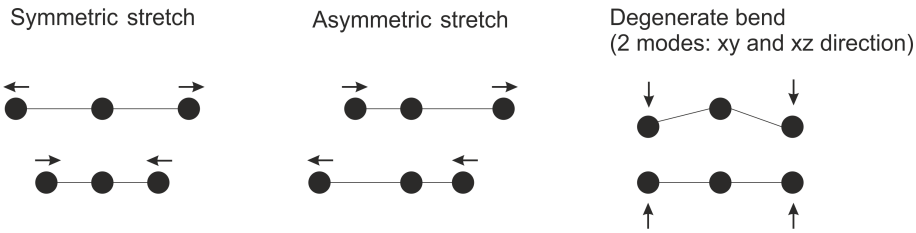


**Figure 3.1:** A schematic view of all principal vibrational states for all 3-atom, linear molecules, including OCS.

The density of absorption lines originates from the different rotational and vibrational transitions, forming multiple absorption bands. In this work (for both $OCS$ instruments, included in this work: AMICA and MICA), the strong $OCS$ absorption line at 2050.396634 $cm^{-1}$ is chosen. Therefore, a laser is selected, emitting at this wavenumber (with a wavenumber range from 2050.3 to 2050.9 $cm^{-1}$). The $OCS$ asymmetric stretch band contains the strongest absorption lines. The respective wavenumber range together with the absorbing gases in this range are shown in Figure 3.2b. The stronger the absorption line of a substance, the better the detectability and the higher the sensitivity for the measured gas. The absorption strength/ attenuation depends on the absorption coefficient and concentration of the absorbing substances in the measurement gas as well as the length of the measurement cell. This relation is described by the Beer-Lambert Law as presented in Equation 3.1.

$$\begin{aligned} A &= log_{10}(\frac{I_0}{I}) = \epsilon_\lambda \cdot conc \cdot L \\ I &= I_0 e^{-A} \end{aligned} \tag{3.1}$$

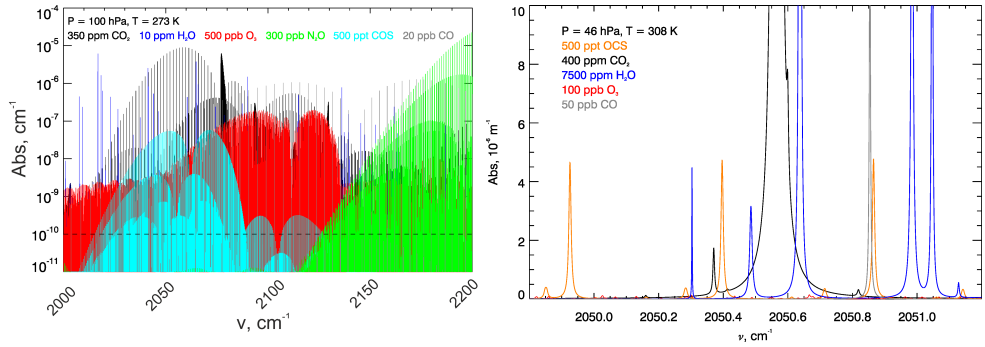


(a) (b)

**Figure 3.2:** Wavenumbers against absorption, for $OCS$, $CO_2$, $H_2O$, $O_3$ and $CO$. (a) All vibrational bands of the absorbing gases of interest, of the asymmetric stretch, vibrational band of $OCS$. (b) The enlargement for the exact wavenumber range, used in MICA and AMICA.

$A$: absorbance of the material at wavelength $\lambda$

$I_0$: incoming light intensity

$\frac{I}{I_0}$: transmission

$conc$: concentration of the absorbing species

$I$: transmitted intensity, light intensity after passing through the absorbing substance

$\epsilon_\lambda$: extinction coefficient at wavelength $\lambda$

$L$: absorption path length

The Beer-Lambert law describes the attenuation of light in a substance, passing through a specific length of measurement cell. When the measurement cell length and extinction coefficient are constant, the absorbance is proportional to the concentration of the gas. The transmitted light intensity decreases exponentially.

The main limiting factor for the spectral resolution in IR spectroscopy is the line width. It is described as the HWHM (half-width-half-maximum) of an absorption line. A higher spectral resolution results in a smaller line width. Therefore, it is favorable to minimize the extent of the line broadening as much as possible. Besides the natural line broadening of a molecule, two broadening mechanisms contribute to the peak broadening.

Pressure/Collisional broadening: because of collisions between molecules in the gas phase, there is an energy exchange and shift of the respective molecules, leading to a broadening of energy levels. The degree of the broadening effect depends on density and temperature of the measurement gas. For the two instruments, introduced in this work (MICA and AMICA), this is by far the highest contributer to the peak broadening. A reduction of the pressure broadening effect can be achieved by reducing pressure and temperature in the measurement cell at the expense of reduced sensitivity.

Doppler broadening: this is a process leading to peak broadening explained by the Doppler-effect. For non moving molecules and detector the absorbed frequency is distinct. However, due to the Brownian motion of molecules the Doppler-broadening arises.

## 3.2 The ICOS method

The general set up of ICOS consists of a laser, cavity and a detector as seen in Figure 3.3. The laser is pointed off-axis into a cavity, enclosed with two high reflectivity mirrors. Off-axis means that the laser beam has no specific exit point from the cavity and the light is bundled with a collimator lens behind the cavity and focused onto the detector. Therefore, the system is robust against vibrations and ideal for moving measurement platforms like research aircraft. A cavity entry point in the middle of the mirror could lead to unwanted cavity resonance effects, therefore the entry point is not chosen to be centric. The mirror at the side of the laser, has an Anti-Reflection coating.
The laser is stabilized to a certain temperature that determines the wavenumber range over which it can potentially emit. Figure 3.4 shows the respective emitted wavenumber range for temperature and current settings for the laser used in the MICA instrument, which is the prototype of AMICA with the same measurement technique. MICA was investigated in more detail in Schrade (2011). An increasing laser input current leads to a decreasing output wavenumber. Lower temperatures of the laser result in an increasing laser output wavenumber. For example, for the temperature stabilized MICA laser (LC0107) at 50 °C, operated at 0.72 A, the wavenumber output is 2044 $cm^{-1}$ (= 4.89 $\mu$m). Because the laser output wavenumber is sensitive towards minor temperature changes in the laser (as seen in Figure 3.4), a good temperature regulation at the laser is necessary. The laser itself has a temperature stabilization unit (optimized by the internal software), which, however, cannot account for large temperature fluctuations around the measurement set up. Therefore, a pressure and temperature stabilized measurement set up is crucial to ensure a sufficiently working temperature regulation at the laser. For the instrument AMICA, longterm drifts in the obtained spectrum due to e.g. temperature changes of the laser or in the cavity are possible, because the internal software unit, regulating the temperature at the laser is not optimized yet. The higher the reflectivity of the mirrors, the longer is the maximum possible absorption path length and thus the lower the detection limit towards absorbing gases. Substances with high absorption coefficient and mixing ratios, however, can reach the state of saturation for long path lengths.


**Figure 3.3:** ICOS setting, the way of light for a single cavity.

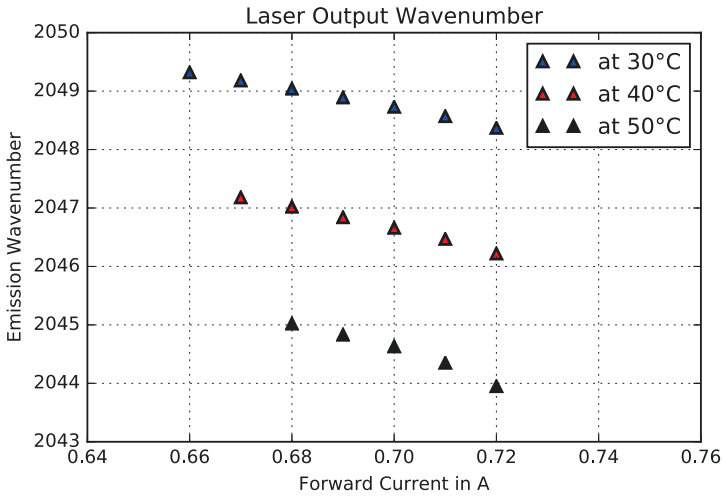


**Figure 3.4:** Emitted laser output wavenumber in $cm^{-1}$ at a certain temperature (in °C) and current (in A) for the laser LC0107, used in the MICA instrument, data from HAMAMATSU PHOTONICS K.K. (2009).

The laser light is reflected back and forth, filling the cavity with light until the light retraces the path through the cavity. The average time that light at a certain wavelength is trapped in the cavity, equivalent to the ringdown time, depends on the mirror reflectivity, cell length and concentration of the absorbing gases at this wavelength, this is calculated in Equation 3.2 (taken from Sayres et al. (2009)).

$$\tau = \frac{L}{c\underbrace{[1 - R + \alpha(\nu)]}_{\mathrm{A}}} \tag{3.2}$$

$\tau$: cavity-ringdown time
$c$: speed of light
$R$: mirror reflectivity
$L$: cell length
$\alpha(\nu)$: single pass absorption, optical depth of the measurement gas at frequency $\nu$
The term A in Equation 3.2 describes the total loss rate of light at a single pass through the cell due to absorption and loss at the mirror. The length of the cell L divided by the speed of light represents the time per one pass through the cell. The ratio of both terms, describes the decay time, the average time that the light is trapped in the cavity, the cavity-ringdown time (Equation 3.2). With the known values of mirror reflectivity and absorption, the effective path

length can be extracted.
The Gain factor G is described in Equation 3.3 (O'Keefe et al., 1999). It is the average number of passes through the measurement cell, depending on the reflectivity R of the mirrors and describes the increase in the measured absorption, compared to a standard cell (without mirrors and only one path through the cell) and therefore describes an increase in sensitivity.

$$G = \frac{R}{1-R} \tag{3.3}$$

Equation 3.4, taken from Sayres et al. (2009), describes the light intensity measured at the detector (i.e. the laser intensity from one side of the cavity):

$$I_{out}(t) = \sum_{t'=-\infty}^{t} \underbrace{\frac{1}{2}}_{\text{B}} \underbrace{P(t')T\tau(t')}_{\text{C}} \underbrace{[1 - e^{\frac{-\Delta t}{\tau(t')}}]}_{\text{D}} \underbrace{e^{\frac{-(t-t')}{\tau(t')}}}_{\text{E}} \cdot \underbrace{T}_{\text{F}} \tag{3.4}$$

$I_{out}(t)$: light intensity that is emitted from the cavity at time $t$
$P(t')$: power emitted by the laser at time $t'$
$T$: transmission through the mirror on entry side
$\tau(t')$: decay time constant
$t'$: time when light enters cavity
$\Delta t$: small time step so that $P(t')$ and $\tau(t')$ can be considered as constant
The role of the terms B, C, D, E and F from Equation 3.4 are further explained. B: the factor $\frac{1}{2}$ comes from the fact that from both sides of the cavity light is emitted, $I_{out}(t)$ describes the intensity at the detector, so only emitted light from one side of the cavity. C describes the amount of transmitted laser power into the cavity. D represents the build up of light inside the cavity at $\tau(t')$. E accounts for the intensity evolution, considering the loss of intensity through both mirrors and absorption at the measurement substance. F: the factor of $T$ is inserted due to the transmission loss of light at the mirror before entering the cavity.
Figure 3.5 shows the data acquisition and atmospheric spectra analysis in three steps. The laser is switched on, the laser input current increases throughout the ramp scanning spectrum and the laser is switched off (Figure 3.5a). The laser cycles are continuously repeated $\sim$ 600 times per second. Each laser cycle has a time duration of 1.64 ms. In Figure 3.5a and Figure 3.5b the wavenumber decreases in x-direction and can be derived for the conversion to Figure 3.5c using an etalon fit.
During the spectrum scan, at each moment a different laser wavelength is emitted and coupled into the cavity with the absorbing gas. 600 cycles are conducted and detected per second and averaged (Figure 3.5b). This signal is equivalent to the measured laser intensity as described in Equation 3.4. The voltage is proportional to the laser intensity.

With ICOS, not the decay time of a laser pulse at a specific wavelength through a certain

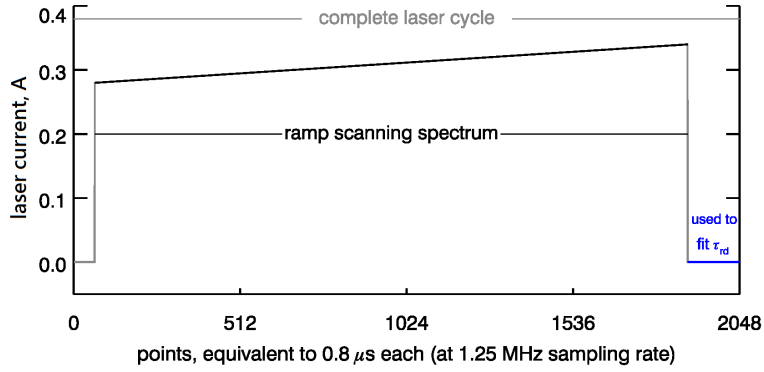


(a)

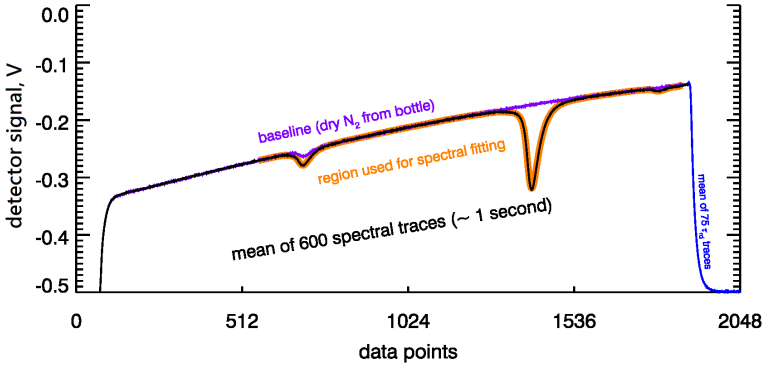


(b)

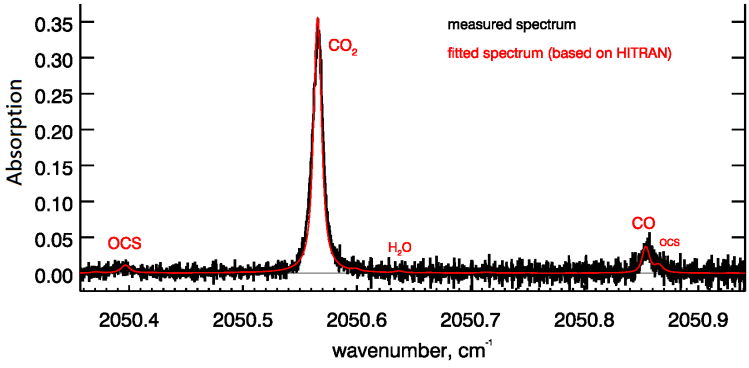


(c)

**Figure 3.5:** Data acquisition and atmospheric spectra analysis. (a) Laser input current. (b) Signal at the detector. (c) The obtained spectrum, fitted to the HITRAN (High Resolution Transmission, Cambridge, Massachusetts) data base.

medium is measured to obtain mixing ratios (e.g. Cavity-Ringdown Spectroscopy), but the light intensity along a wavelength range is measured at the detector and analyzed.
The baseline is defined by sending a pure gas through the system. In Figure 3.5b $N_2$ is used, $CO$ impurities can be seen (in purple). Points with no absorption are extracted so that an accurate baseline can be determined for the region of interest and used for spectral fitting. At the end of each laser cycle, the laser is switched off and the cavity-ringdown time $\tau$ is measured, by fitting an exponential decay to the decrease of the intensity indicated in blue in Figure 3.5b. The spectral scan points are translated into wavenumbers and the signal is converted from transmission into absorption, using Equation 3.1. The largest peak in Figure 3.5b at the data point $\sim$ 1350, represents $CO_2$ and is translated to the wavenumber 2050.56 $cm^{-1}$ in Figure 3.5c. The peak seen in Figure 3.5b at data point number $\sim$ 870 is translated to a wavenumber of 2050.8 $cm^{-1}$ and represents $CO$. $OCS$ is at a data point number of $\sim$ 1610, seen in Figure 3.5c at the wavenumber of 2050.39 $cm^{-1}$. In Figure 3.5c, the obtained signal (spectrum) per wavenumber from a dried standard of ambient air in black and the fitted spectrum based on the HITRAN data base in red. A theoretical spectrum is calculated, based on fixed HITRAN parameters and mixing ratios for the trace gases, absorbing in the wavenumber region. This theoretical spectrum is compared to the observed spectrum and an iterative optimization routine solves for the best fit mixing ratio. Here, the spectral range used for MICA and AMICA is displayed, measuring $OCS$ at 2050.39 $cm^{-1}$, $CO_2$ at 2050.56 $cm^{-1}$, $H_2O$ at 2050.6 $cm^{-1}$ and $CO$ at 2050.8 $cm^{-1}$.

## 3.3 Requirements for OCS measurements

### 3.3.1 MICA

MICA is the prototype of AMICA, a ground based ICOS instrument, measuring $OCS$, $CO_2$, $CO$ and $H_2O$ since October 2012 on the meteorological tower at Forschungszentrum Jülich GmbH. Prior to the construction and arrival of AMICA, tests e.g. the established $OCS$ calibration system, were carried out with the MICA instrument.
The ground based instrument MICA already contributed to multiple scientific projects: Lennartz et al. (2017) work with shipboard $OCS$ measurements of MICA. During StratoClim it was part of a ground based measurement station on Bhola Island and at the Palau station in the western Pacific.

### 3.3.2 Material criteria

Especially when calibrating the instrument, but also for qualitative measurements, all materials in the measurement system (that potentially have contact with the sampling air) need to be checked for suitability for $OCS$ measurements. Some valves have viton seals, which outgas $OCS$

and therefore interfere with $OCS$ measurements. A good replacement for viton, however, has not been found yet and for the magnitude of accuracy that AMICA shows at the moment, the viton sealing likely makes no significant difference. For the tested flow of 1 SLM (standard liter per minute), the out-gassing of the viton seal does not show any effect and is therefore considered negligible. For highly accurate measurements, it should be replaced in the future. Due to its polarity, the $OCS$ molecule interacts with surfaces of some materials, e.g. glass, metal and plastics. Materials used for AMICA, measuring $OCS$ need to be as inert as possible to avoid reaction with the wall material and absorption. Electropolished stainless steel, sulfinert treated steel (i.e. silcosteel), silanized glass and teflon (PTFE: Polytetrafluorethylene) are known to be most suitable for volatile sulfur compounds measurements (Wardencki, 1998). However, observations using MICA indicated that Teflon tubes might not be as suitable for $OCS$ measurements due to the porosity, 'sponge effect'. When a Teflon tubing (FEP: Perfluoroethylene propylene) was exposed to a constant flow of high $OCS$ mixing ratios ($\sim$ 50 ppb), then flushed and connected to AMICA, measurements showed that around 10 times higher mixing ratios are reached then expected in ambient air. The tube was exchanged to avoid that problem.

### 3.3.3 Calibration system for OCS

It is almost impossible to dilute an $OCS$ standard with a mixing ratio of around 500 ppt from a pure gas with sufficient accuracy, i.e. no primary standards at atmospheric concentration are readily available. Additionally, as described in Chapter 3.3.2, $OCS$ is emitted and/or absorbed by many surface materials so that caution has to be taken with all components used in the calibration system. A system, which is able to produce a wide range of $OCS$ concentration to test the AMICA output for a variety of mixing ratios, is beneficial and therefore developed:
Two complementary calibration systems were established and are used for the $OCS$ calibration of MICA and AMICA, a permeation device set up and a NOAA (National Oceanic and Atmospheric Administration) $OCS$ standard.
For the permeation system (optimized and described in von Hobe et al. (2008)), two permeation tubes ($OCS$ 15920 and $OCS$ 90F3) with different permeation rates were purchased from MACHEREY-NAGEL GmbH, Düren, Germany. The tubes contain pure $OCS$ ($>$ 99 %) and release $OCS$ at a specific rate at specific temperatures (here 25 °C). The weight of the tubes are regularly gravimetrically determined and the permeation rates calculated (26.0 $\pm$ 0.1 ng min$^{-1}$ and 142.0 $\pm$ 0.8 ng min$^{-1}$). While the tube with the lower permeation rate ($OCS$ 15920) shows a linear decrease of weight with time, the rate of loss of the other tube ($OCS$ 90F3) decreases with time. Therefore, only the $OCS$ 15920 is used for calibration purposes. For the gravimetric determination of the permeation rates an analytical balance (CPA225D, Sartorius Lab Instruments GmbH, Göttingen, Germany) is used, which was calibrated by the DKD (Deutscher Kalibrierdienst, Braunschweig, Germany). The display uncertainty, operated on a weighting ta-

ble, is $0.8 \cdot 10^{-5} g + 10^{-6} \cdot R$, where R is the scale display value. A special oven was developed to keep the sample air around the permeation tubes at a stable temperature of 25 °C, also at higher flows ($>$ 20 SLM). The air first passes through a long curled tube, temperature regulated in an oven, before it passes the permeation tube(s). With one or two (parallel) MFCs (Mass Flow Controller MC-10SLPM-D, NATEC Sensors GmbH, Garching, Germany), the dilution flow can be regulated to up to 40 SLM and together with the known permeation rates, the resulting concentration of the produced gas is calculated. A typical calibration set up with the permeation system, is shown in Figure 3.6. The advantage of the permeation device system is that a wide range of $OCS$ mixing ratios from $\sim$ 45 ppb down to $\sim$ 300 ppt can be scanned. This potentially reveals systematic deviations of the instruments output concentrations to the gravimetric calculated mixing ratios, but also non-linear behaviors of the instrument.
In addition to the permeation tube system, a NOAA $OCS$ standard was used. A 34 L electro polished stainless steel Essex container was filled with dried, atmospheric air to $\sim$ 62 bar, transfered from an Aculife-treated aluminum cylinder. The gas was analyzed by gas chromatography with mass spectrometric detection (GC-MS) at NOAA. The 'report of analysis' (from January $6^{th}$ 2015) gives a mole fraction for $OCS$ of 449.8 ppt with a standard deviation of 1.4 ppt. Based on the uncertainties and comparisons between NOAA and other labs, the scale accuracy for $OCS$ is approximately 4 %. Internally the standards are consistent to $\sim$ 2 %. A drift of $OCS$ mixing ratios of less than 5 ppt per four years in the cylinder is assumed. The air is humidified with $\sim$ 0.6 ml HPLC-grade water. The water content in the NOAA standard is $\sim$ 500 ppm, AMICA shows 283 $\pm$ 4 ppm $H_2O$. For $OCS$, however, the water content in the electro-polished stainless steel container is considered to improve stability (personal communication, Bradley Hall, NOAA). The standard is recommended to be recalibrated after three years. For calibrations with the NOAA $OCS$ standard, a stainless steel pressure reducer (Parker TDR 959, Richmond, California) was ordered and is used.
The developed permeation system in combination with the NOAA $OCS$ standard makes a comparison possible of our own wide calibration scale and the global NOAA network.

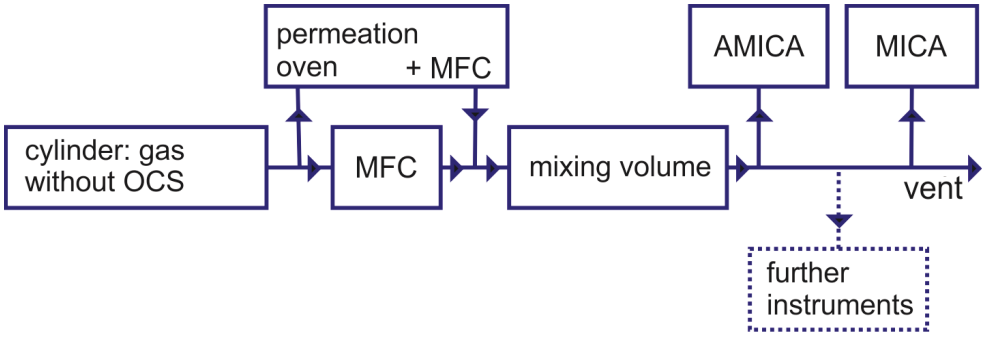


**Figure 3.6:** A typical set up for simultaneous comparison and calibration of potentially more than our two *OCS* instruments (AMICA and MICA).

### 3.3.4 OCS calibration and comparison with Mainz LGR

Two *OCS* instruments using the ICOS method are compared to each other and calibrated: one instrument, operated by the University of Mainz (referred to as 'Mainz LGR') and MICA. Both instruments are purchased and manufactured by LGR (Los Gatos Research, Mountain View, California). MICA was the first LGR *OCS* analyzer (2012), while the Mainz LGR instrument (2015) is a newer and further developed ICOS instrument. The Mainz LGR belongs to the 'Enhanced Performance' series, with a stronger laser, mirrors with a higher reflectivity and a 20 cm longer cavity (50 cm). Additionally, an improved analysis software and temperature stabilized Laser-Cavity-Detector system leads to an improved signal to noise ratio by more than one order of magnitude.

The set up chosen for the calibration and comparison of both instruments is the same as already shown in Chapter 3.3.3, Figure 3.6 (in this case 'further instrument' refers to the Mainz LGR ICOS instrument, AMICA was not included in this set up). Figure 3.7 shows the lowest 14 values of the MICA Mainz LGR ICOS comparison calibration. The MICA data are shown in green, the Mainz LGR measurements in cyan. A systematic error for the gravimetric values of 0.6 % and the observed *OCS* standard deviation of MICA are indicated with error bars. For the Mainz LGR *OCS* measurements, no standard deviations are calculates, but are around one order of magnitude lower than the ones observed with MICA. Each displayed measurement point corresponds to the mean value of a ~5 minute mixing ratio step, regulated via the amount of flow of the standard air (with no *OCS*), which is then mixed with the sample air from the permeation oven. With this system, mixing ratios up to 35 ppb are achieved, however a typical *OCS* mixing ratio in the troposphere is 500 ppt. Therefore, the lowest data points achieved with this method are best representative for atmospheric *OCS* mixing ratios and are shown in Figure 3.7.

MICA consistently overestimates the true (gravimetrically determined) values, while Mainz LGR underestimates them. For MICA a linear correction equation was determined (0.92x + 9.63 ppt)

to shift the measured values as close as possible to the true gravimetric line (black). A qualitative evaluation of the correction performance is shown in Figure 3.8. Before the correction, MICA showed a relative deviation to the gravimetric values of up to 9 % (red crosses), while after the correction the highest deviation is 5 % (black crosses). The red crosses in Figure 3.8 indicate the relative deviation of the green crosses in Figure 3.7 from the black 1- to 1 line and black crosses in Figure 3.8 indicate the respective deviation from the corrected values (using the correction equation) to the black line. Especially for high mixing ratios $> 2$ ppb, the deviation is below 1 %.

Even though the Mainz LGR instrument is much newer with a better precision compared to MICA, the accuracy of both instruments is comparable.

Compared with MICA, for AMICA many amendments have to be made in order to adapt for research aircraft requirements. The mechanical requirements are discussed in Chapter 3.4.

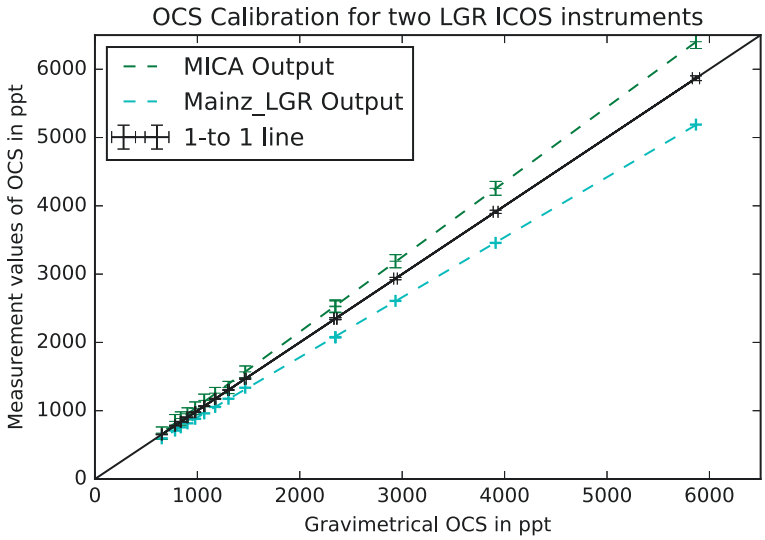


**Figure 3.7:** MICA (green) and Mainz LGR (cyan) *OCS* measurement values together with their linear fit. The black one- to- one line represents the desired measurement outcome of the instruments with no deviation from the gravimetric values. Error bars for the MICA *OCS* measurements and the gravimetric calculated values are indicated. The resulting correction function for MICA is: 0.92x + 9.63 ppt.

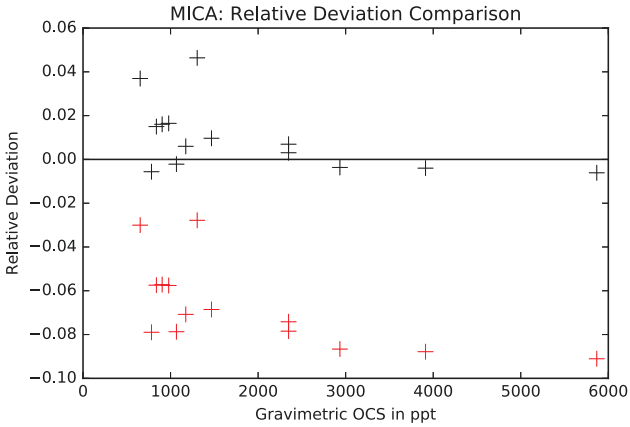


**Figure 3.8:** The relative deviation from the MICA *OCS* values to the gravimetric *OCS* values, before (red) and after (black) applying the correction function.

## 3.4 Mechanical requirements for AMICA on the research aircraft Geophysica

For AMICA to be integrated on the research aircraft Geophysica, two official tests had to be passed, an EMC test and a shaker test:

- EMC test: an official electromagnetic compatibility (EMC) certificate is needed, proving that the running instrument AMICA does not exceed the Geophysica threshold criteria, according to the environmental conditions and test procedures for airborne equipment (RTC-DO160 E, category M), to exclude the possibility of interferences with the aircraft electronics and other instruments. Before the actual certification test, AMICA was already tested at the EMC chamber at ZEA-2, Forschungszentrum Jülich GmbH. Here, major sources of interference (e.g. cockpit-control cable, an opening at the left thermoelectric cooler (TEC)) were identified and removed before the official test. The test carried out at steep GmbH, EMC Center Bonn, Germany on two days, two months prior to the first planned campaign, was directly passed.
- Shaker test: an official shaker test for aircraft requirements was carried out at MOOG, CSA Engineering, Mountain View, California. For this purpose a second, identical AMICA housing was manufactured. The vibe testing report states that the AMICA housing responds to a 0.5 g sine sweep, before and after the application of random vibe with no significant difference in isolation system behavior. AMICA was additionally laid out for elastic deformation at $> 7$ g with fully preserved functionality and plastic deformation at $> 10$ g. The test was successfully passed under the test procedure RTCA/DO-160G (elastic

deformation permitted for 7 g acceleration in X-, Y and Z direction). Three springs (Endine WR12-300-08) prevent damage to the instrument caused by excessive vibrations, selected based on finite element method (FEM) calculations. The maximum force per spring is 9 kN, resulting in a spring deflection of 32.5 mm and 7.5 kN with 39 mm deflection under shearing. The springs are designed for shearing forces up to 10 g in all directions.

Other criteria for aircraft suitability is a reduction of weight of the instrument. Therefore, a small, light weight pump, which fits into the instrument AMICA is crucial. At the same time, the pump has to maintain a sufficient flow through the measurement cells at changing outside pressure (55 hPa to 1000 hPa). Besides flow rate at different ambient conditions, other criteria for pump selection have to be considered: heat production during long term use, power draw, size and weight. Respective tests are described in Chapter 3.6.

As discussed in Chapter 3.2 the cavity pressure of the ICOS system is stabilized. A higher pressure results in a higher sensitivity of the instrument, but also in a higher pressure broadening. As a good compromise a typical LGR *OCS* Analyzer has a stabilized cavity pressure at 80 hPa (60 torr), for ambient pressures of 1000 hPa. However, on research aircraft ambient pressures change between 1000 and 55 hPa and because the cavity pressure cannot be stabilized at pressures exceeding ambient pressure, another compromise is found at 47 hPa in AMICA. Experiments for pump selection and flow set up are described in Chapter 3.6.1

Other requirements for trace gas measurements, the measurement set up of AMICA and the mechanical design are investigated during lab experiments. The results are presented in Chapter 3.6.

## 3.5 Mechanical design of AMICA

AMICA is a 104 cm × 40 cm × 30 cm (without feet and mounting hardware) instrument visualized in Figure 3.9 and was delivered in February 2016. The total weight of AMICA is 153.7 kg (141.1 kg without feet and mounting hardware). The power box weighs 19.4 kg (5.4 kg housing, 14 kg interior) and the pressurized box 134.3 kg (58.6 kg housing, 12.6 kg aircraft attachment, 63.1 kg interior including measurement set up). The pressurized box is made out of aircraft certified aluminum (EN AW6061 T651) and contains the measurement set up including laser, cell and detector. AMICA is powered with 115 V, 400 Hz with a maximum of 1.2 kVA.

The power box contains the pump, the AC-DC converters, electro-magnetic interference (EMI) filters and temperature controllers. Wireless access to the AMICA measurements and data (12 V electricity supply) is integrated and enables the communication and data download from the instrument, with a range of $\sim$ 200 m with AMICA situated under the MIPAS cover on the research aircraft Geophysica. Hence, during operation it is possible to monitor data and spectra on-line. The power supply for the wifi (on or off, via relais) is turned off, from the cockpit of Geophysica, during flight to avoid interferences with the aircraft electronics.

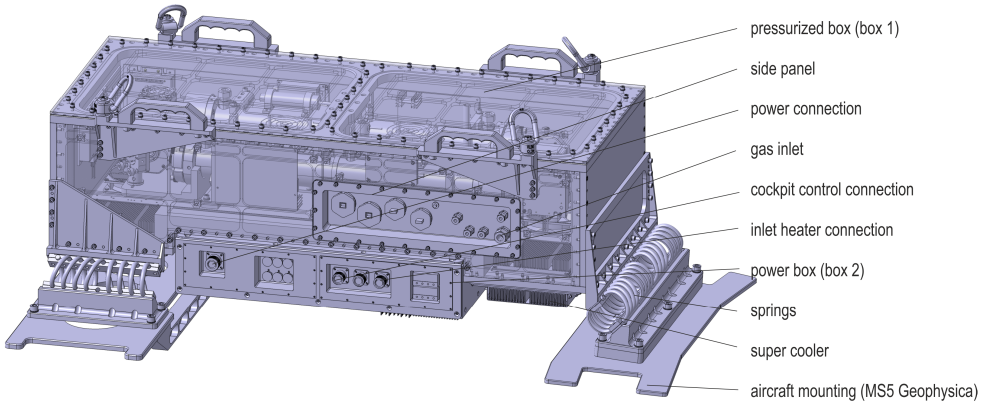


**Figure 3.9:** Rendered view of AMICA (by ZEA-1, Forschungszentrum Jülich GmbH) with part description.

The power box, attached underneath the enclosure, is not pressure tight and is made of aluminum sheet metal (EN AW 5052 H111). The enclosure with the measurement hardware is built pressure tight, see Chapter 3.6.2.
Figure 3.10 shows how AMICA is implemented on the top of the research aircraft Geophysica. Because of its weight and position on the aircraft, AMICA is equipped with handles, for short distance transportation and crane attachments, for lifting the instrument to the respective position on Geophysica.
In AMICA, two separate measurement cells are integrated in one single ICOS instrument. The individual set ups are exchangeable in order to tailor the trace gases measured to the relevant science question. A variety of gases can be measured simultaneously. The measurement configuration is shown in Figure 3.11 with the two measurement set ups implemented in AMICA.

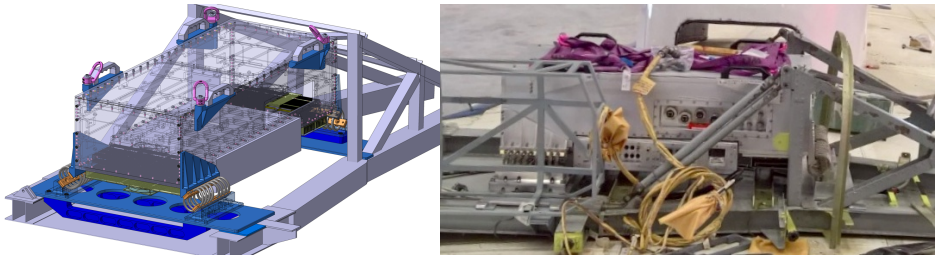

**(a)** **(b)**

**Figure 3.10:** Scematic view (by ZEA-1, Forschungszentrum Jülich GmbH) (a) and photograph (b) of the integration of AMICA on top of the research aircraft Geophysica.

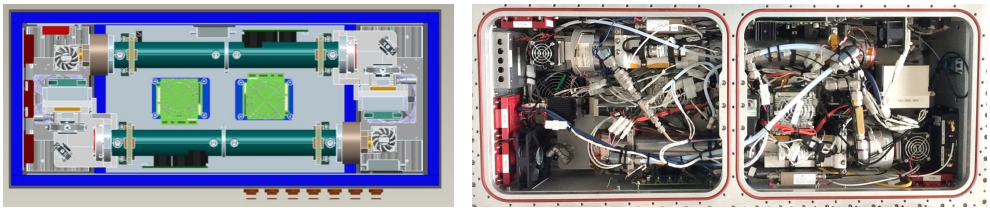

(a) (b)

**Figure 3.11:** One schematic (by Los Gatos Research, Mountain View, California) (a) and one photograph (b) of the top view of the interior of AMICA, showing both cavities.

The first set up includes a Quantum Cascade Laser (QCL), emitting in a wavenumber range of 20150.3 - 2050.9 $cm^{-1}$, measuring $OCS$ at 2050.39 $cm^{-1}$, $CO_2$ at 2050.56 $cm^{-1}$, $CO$ at 2050.80 $cm^{-1}$ and $H_2O$ at 2050.60 $cm^{-1}$. These compounds are measured in cavity 1 (c.f. Figure 3.12). The cavities are exchangeable and replaceable. Each measurement assembly is controlled by a dedicated computer. For cavity 2, two measurement configurations are currently possible: a QCL emitting in a wavenumber range from 1035.30 - 1035.90 $cm^{-1}$, measuring $O_3$, $NH_3$ and $CO_2$ and an Interband Cascade Laser (ICL) emitting in a wavenumber range from 3331.20 - 3331.80 $cm^{-1}$, measuring $N_2O$, $HCN$ and $C_2H_2$. The process of exchanging cavity two is too elaborate to be done between flights during a measurement campaign.
As described in Chapter 3.2 the cavity pressure is stabilized (for AMICA at 47 hPa; for selection criteria c.f. Chapter 3.4). The LGR data acquisition quality is strongly dependent on a constant temperature and pressure in the cavity. The flow set up in AMICA for regulating the cell pressure has been chosen according to the lab results, described in Chapter 3.6.1. Figure 3.12 shows a schematic set up of the flow system used in AMICA. The inlet is a 3/8" tubing connection. Before the sample air enters the enclosed system, it is filtered by a 7 $\mu$m sulfinert treated filter, (filter 1: SilcoNert2000 coated Swagelok SS-4FW7-7, SilcoTek GmbH, Bad Homburg, Germany). Inside the enclosure it passes through a two valve assembly designed to regulate the pressure inside the cavities. The development of this two valve system is described in Chapter 3.6.1. All surfaces are passivated to minimize wall interactions. A 2 $\mu$m filter (filter 2: SilcoNert2000 coated Swagelok SS-4FW4-2, SilcoTek GmbH, Bad Homburg, Germany) is placed in front of the cavity to prevent particles from the valve seals to enter the cell and contaminate the highly reflective mirrors in the cell. The cells are coupled in series and regulated to a constant pressure of 47 hPa in the first cell and due to the serial set up a 1.3 hPa decreased pressure in the second cell. The cells have a volume of 0.911 L and are 51 cm long.

- Time delay (from inlet to measurement cell): the volume between the inlet on Geophysica and cell is around 1 L (including the first cell of 0.911 L). This is equivalent to a measurement delay of 4 seconds with an ambient pressure at 1000 hPa and 0.4 seconds at an ambient pressure of 100 hPa (at an aircraft speed of 200 m/s this is a distance of around

800 and 80 m respectively). At a measurement rate of 1 Hz every 200 m one data point is acquired.

- Time lag (between both cavities): the time lag between both cells is 2.8 seconds (which is equivalent to 560 m at an aircraft speed of 200 m/s). The proportional Solenoids of the delivered instrument had orifices of 1 mm each (Parker), which were prove to failure (Chapter 3.6.1). For the first campaign the valves with orifices of 1 mm (valve 1: Parker Porter EPCA30SSVCAA, Hatfield, Pennsylvania) and 3.2 mm (valve 2: Posiflow SCB202A013T12VDC, ASCO Numatics GmbH, Ölbronn-Dürrn, Germany, Teflon sealed) were chosen.
- Flush time: Behind the cells a check valve is integrated to avoid any back flow into the system. The system works with a flow rate of 1 SLM at ground conditions, 1000 hPa ambient pressure at a gas temperature of around 30 °C. The flow rate is thought to be higher during flight when the outside pressure decreases. The flush time of one cell is 2.1 seconds. The pump (vacuubrand MD1 VARIO-SP, Wertheim, Germany) is installed outside of the pressure tight enclosure, integrated in the power box.

Temperature stabilization of the measurement set up is necessary to improve temperature regulation for the lasers and detectors. The interior of the AMICA enclosure is temperature regulated at 30 °C, using two banks of thermoelectric coolers (TEC). Each bank consists of 16 individual TEC elements ('supercoolers'), measuring approximately 30 mm square and is capable of producing 200 W of heating or cooling power. These supercoolers are attached underneath the enclosure seen in Figure 3.9. The walls are insulated on the inside with polyethylene foam (ETHAFOAM$^{TM}$ 4101 FR Polyethylene Foam, Midland, Michigan). Additional fans enhance air circulation inside the enclosure to improve temperature uniformity. The temperature regulation is implemented in the standard 'Enhanced Performance Analyzers' by LGR.
In addition to the measurement data of the different compounds, many housekeeping data are logged by the LGR software, and some additional loggers are attached. A logger (MSR165, Seuzach, Schweiz) is integrated, monitoring the enclosure pressure and temperature independently to the housekeeping data from the AMICA software. Another logger (MSR165), monitoring the output voltage from the VIPACs (DC-DC converter, VICOR HUB 3300-S, Andover, Massachusetts) is also integrated. Two SlamSticks (Mide Technology LOG000200-0006, Medford, Massachusetts), mainly monitoring vibration, but also pressure and temperature are attached to the outside of the AMICA housing. One above a spring and one below, to observe the effect of the springs. Both loggers and both SlamSticks are triggered over an individual software from the computer via USB port connection.
An inlet integrated on the top of Geophysica was designed and developed by enviscope GmbH, Frankfurt, Germany (Figure 3.13, picture in Figure 3.14). It has a weight of 2.5 kg and is shared between three instruments, a Cryogenically Operated Laser Diode spectrometer (COLD), The Chicago Water Isotope Spectrometer (Chi-WIS) and AMICA.

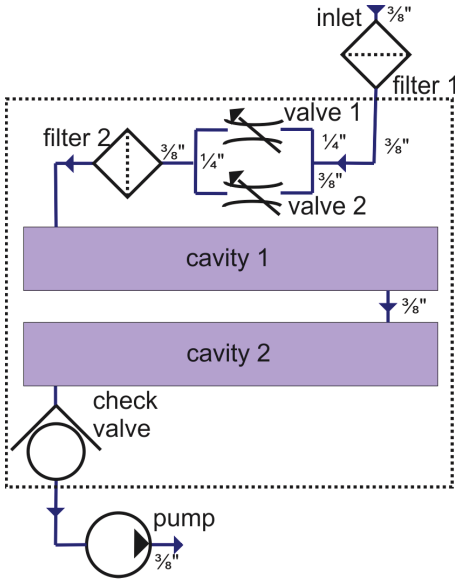


**Figure 3.12:** Overview of the flow system integrated in AMICA.

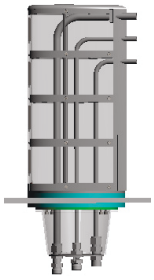

**Figure 3.13:** Geophysica inlet for AMICA, Chi-WIS and COLD, designed by enviscope.

**Figure 3.14:** The position of the inlet on the Geophysica.

The tube connection to AMICA is sulfinert treated stainless steel (RESTEK, Bad Homburg, Germany, diameter 3/8 ").

The position on the plane is seen in Figure 3.14. To avoid aerosol penetration during flight, the inlet points backwards to the flight direction. The front of the inlet is heated by the Geophysica with 27 VDC. The AMICA tubing inside of the inlet is also heated (115 VAC supply from AMICA), when temperatures drop below 10 °C. The inlet and AMICA are connected by a 160 cm sulfinert treated tube, on both sides connected to bellows for flexibility.

## 3.6 Laboratory performance assessment

Several lab experiments have been carried out during this project. The following questions are addressed in this section.

- How is the cavity pressure kept constant at highly variable ambient pressures (50 - 1000 hPa) on reseach aircrafts?
- How is the acquisition hardware of AMICA kept at a constant temperature (c.f. Chapter 3.2) (at 35 °C ± 0.5 °C) to ensure accurate measurements?
- How does the whole instrument, including the developed components, perform during a flight simulation test?

Experiments as described in Chapter 3.6.1 and 3.6.2, have been carried out under simulated flight conditions in the climate chamber at IEK-7. The climate chamber (WK 500/70-100D) can be regulated from ambient pressure down to 10 hPa and has a temperature range from +100 °C to -70 °C. With a usable volume of 770mm × 750mm × 750mm, it is ideal for component tests of instruments, like AMICA, that are operated on high altitude research aircraft as for example the Geophysica, reaching pressures down to 55 hPa and temperatures down to around - 90 °C.

### 3.6.1 Flow system assessment

The pumps tested are listed in Table 3.1. Figure 3.15a shows the set up of the pump/valve experiments. Components were added to the test step by step. The assembly for the pump tests is shown in blue. The electricity supply for the MFC, pump and pressure sensor are placed outside the chamber and connected through vacuum tight feedthroughs. For AMICA, the KNF 940.5 pump is too big and too heavy, however the main issue is the high flow rate that shows too high resistance at the valve and cavity inlet, decreasing the flow rate from a valve regulated value of 2 SLM (at 1000 hPa) down to 0.2 SLM at 500 hPa. Further tests described here are carried out with the KNF 950.5 and the MD1 VARIO-SP. Because of the smaller size, lower weight, but also similar flow rate as the KNF 950.5 pump, the MD1 VARIO-SP is used in AMICA. Experiments show that the pump does not draw more than 7.54 A at 24 V (during power on). With a varying ambient pressure (1000 hPa to 55 hPa), keeping a constant pressure inside the cavities at 47 hPa is challenging. Experiments at different ambient pressures in the climate chamber show that a stable pressure inside the cavities cannot be sustained with one valve. Proportional solenoid valves are used. Either the orifice of the valve is too large to regulate the cavity pressure at high ambient pressure or it is too small to sustain a sufficient cell pressure at low ambient pressure. Hence, a parallel 2 valve set up was constructed as shown in Figure 3.15a (in blue, green and purple) with one larger and one smaller valve. Different orifice sizes were employed. The most successful assembly employed valves with orifices of 0.762 mm and 2.4 mm. Each valve is triggered by a Redwave pressure controller (RedWave Labs PC-200, Didcot, United Kingdom), the pressure is measured by a pressure sensor (1406405 honeywell, Columbus,

**Table 3.1:** Relevant pump specifications in the lab test phase of AMICA development.

| **Pump type** | **volume flow at 40 hPa** | **mass flow** | **weight** | **size** |
|---|---|---|---|---|
| KNF N 940.5 TTE | 41.6 l/min | 1.7 SLM | 18.6 kg | 270 x 246 x 185 mm |
| KNF N 950.5 KNDCB | 12.5 l/min | 0.5 SLM | 6.5 kg | 286 x 186 x 116 mm |
| MD1 VARIO SP | 25 l/min | 1 SLM | 4.1 kg | 223 x 143 x 163 mm |

Ohio). For high ambient pressures, the small valve regulates the cavity pressure. As soon as the smaller valve reaches its limit and the cavity pressure drops below 47 hPa, the bigger valve starts regulating, ensuring accurate regulation within both working ranges. Figure 3.16a shows a 17 h flight simulation of temperature and pressure steps in the climate chamber (red and blue), the cavity pressure and the recorded pump temperature. Figure 3.16b shows in more detail the variability of the cavity pressure. For ambient pressure above 100 hPa, the standard deviation of the cavity pressure is around 0.005 hPa, while below 100 hPa it increases up to 0.5 hPa. Here, the amplitude of the oscillation depends on the setting of the pressure control point units. From the results four important conclusions were drawn:

- The two valve system was successful. For high (above 250 hPa ambient pressure) and low (below 250 hPa) a controlled mode is achieved. During the tests stability was better than 1 hPa in the cavity (c.f. Figure 3.16b). For AMICA, this is acceptable. The settings for the control units need to be optimized to minimize oscillations.
- The pump temperature does not exceed 35 °C even after 17 h of operation. Therefore, overheating is not an issue (c.f. Figure 3.16a).
- Long term drifts (in the time scale of hours) in cavity pressure (c.f. Figure 3.16b) are most likely a result of temperature effects on one pressure sensor. As seen in Figure 3.15a, two pressure sensors are integrated, one for the pressure control units and one for monitoring. Figure 3.16a shows the values observed from the monitoring pressure sensor.
- In the test set up, the diameter of the valves is the main limiting factor for flow resistance and therefore the cavity pressure. For AMICA all tubes and components have to be checked for diameters (c.f. 3.6.3).

**The valve set up in the delivered instrument AMICA:** a two valve set up was assemblied in the instrument (see Figure 3.12). However, the orifices of the valves were not chosen according to the flow system experiments described above. Two valves with an orifice of 1 mm each (Parker Porter) were included. In later tests (Chapter 3.6.3) those orifices were proven to not be sufficient during ambient pressures below 200 hPa.

### 3.6.2 Test enclosure

To achieve a stable temperature in the inside of AMICA it is important to build the 80 L enclosure of AMICA pressure tight, so that the cavity and the laser can work under normal conditions

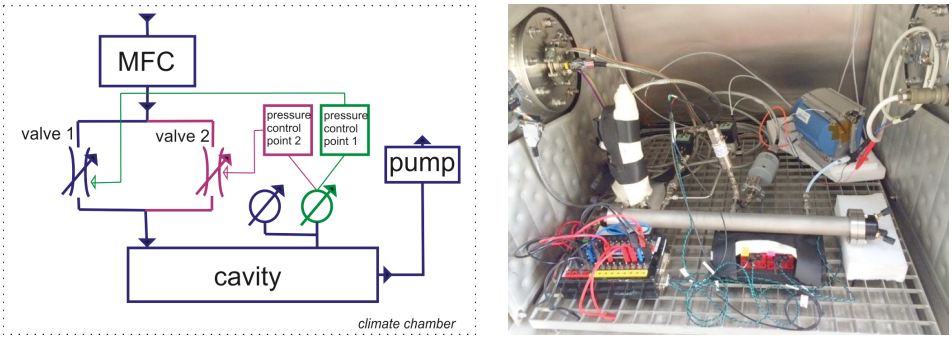


(a) (b)

**Figure 3.15:** The flow system test set up in the climate chamber. The schematic set up evolution in (a) in the order: 1st blue 2nd blue and green 3rd blue, green and purple. A picture of the final set up in (b). Components of the final set up: The flow controller MKS Instruments INC Type 1259CC-02000RV, Andover, Massachusetts; Parker Porter valve with a orifice diameter of 0.762 mm EPCA30SSVCAA, Hatfield, Pennsylvania; ASCO valve Type SCB202A012T12VDC with a orifice diameter of 2.4 mm, Ölbronn-Dürrn, Germany; MD1 VARIO-SP pump, Wertheim, Germany; monitoring pressure sensor MKS Baraton 626 A, Andover, Massachusetts; pressure controller: RedWave honeywell 1406405, Columbus, Ohio.

during a whole campaign flight (ambient conditions: minimum pressure of 55 hPa and minimum temperature of -70 °C).

To save space, a box-shaped enclosure was chosen for the design of the pressure tight box in AMICA. A design using adhesives, screws and bolts was planned for AMICA. Before the actual manufacturing of AMICA, however, a test housing (Figure 3.17), with the same material, screws, adhesives and sealings as planned for AMICA was tested for pressure tightness. Creating a pressure tight box with screws, bolts and adhesive is an innovative, new and challenging approach, here developed to decrease weight and space. (Usually, for a pressure tight approach, a cylinder with two lids is chosen). The starting set up for the tests included:

- Material: chromated aluminum.
- Top cover: screws mounted with 4 Nm torque, oring-seal (Si with Ag).
- Hatch/panel: screws mounted with 2 Nm, oring-seal (Viton), 3 X (1X 6mm, 2X $\frac{1}{4}$“) NPT sealed with Teflon tape.
- Cover on the bottom: screws mounted with 2 Nm torque, flat gasket.
- Connection of the walls: adhesive (Polytec Polymere Technologien, EC 101, Waldbronn, Germany) and bolts.

Helium leak and pressure experiments in the climate chamber were carried out. Bolts are chosen to stabilize the set up and decrease shearing forces that would otherwise effect and weaken the adhesive bonding. However, one major weak point for pressure tightness in the test frame was the bonding adhesive at the bolts between the walls. With the process of several climate chamber

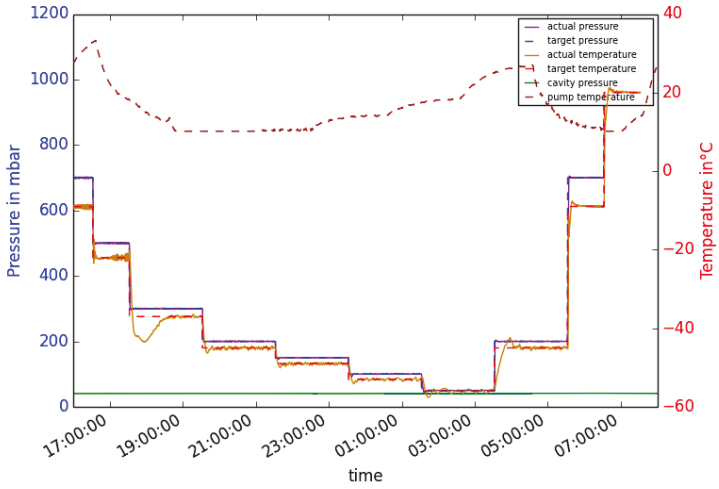


**(a)**

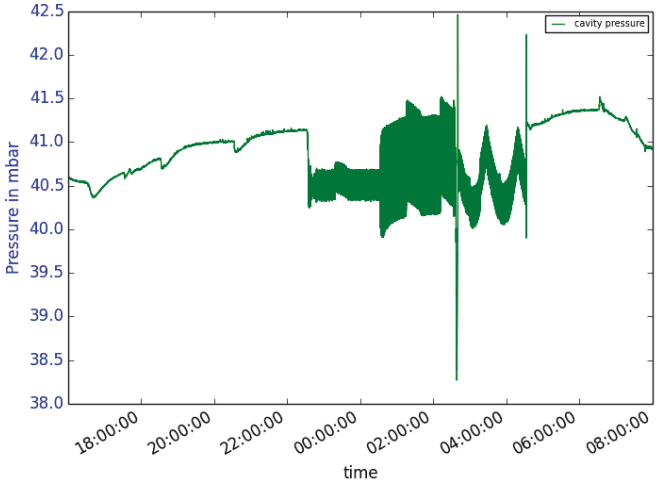


**(b)**

**Figure 3.16:** The 17 h flight simulation steps (pressure and temperature) in the climate chamber and the observed cavity pressure. (a) The first four label descriptions refer to the determined and observed climate chamber conditions. The dotted line shows the pump temperature. The cavity pressure in green is zoomed in Figure 3.16b. (b) Monitored cavity pressure during the flight simulation profile.

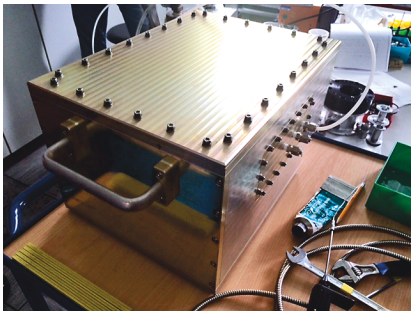

**Figure 3.17:** A photograph of the test frame built to investigate pressure tightness and gain experience for the final mechanical design of AMICA.

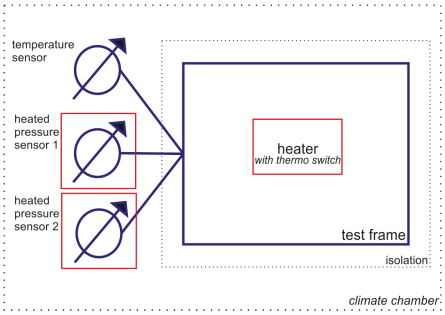


**Figure 3.18:** A schematic view of the test frame set up in the climate chamber. Two heated pressure sensors and one temperature sensor are connected to the isolated and heated test frame.

flight profile tests, with repeating high temperature changes (from +20 °C down to -55 °C), increasing leak rates were detected. This points to plastic deformation at the bolts and adhesive. As a consequence, a silicon sealing was applied to all inside seams (Dow Corning 3145) and from the outside the bolts were sealed with an additional adhesive (UHU Endfest 300).
Another main weakness in the construction of the test frame was identified to be the material of the orings, which were either not pressure tight from the beginning (Si with Ag filling) or leaking at low temperatures (viton orings are specified for temperatures down to -15 °C). Silicon orings perform better at lower temperatures and were used as a replacement. Even silicon orings leaked at very low temperatures <-55 °C. However, for AMICA the inside of the pressurized box is heated and the temperature effect on the seams and pins is expected to be different. Therefore, for the final set up in the climate chamber, a heater was integrated into the test frame and the box was thermally isolated from the outside (Figure 3.18). Two different (same measurement principle but different operating ranges), heated pressure sensors were used to monitor the pressure for comparison (black and green line). Figure 3.19 shows the measured parameters during a climate chamber flight profile of a pressure tight test frame. The behavior of both monitoring pressure sensors is the same with a constant offset of 35 hPa. The temperature inside the test frame stayed above a certain threshold so that the orings did not leak and the pressure inside the test frame remained constant (Figure 3.19). The experiment was successful as the test frame was pressure tight through a whole flight profile simulation. Visible pressure changes, seen in Figure 3.19, are a result of decreasing temperature in the test frame ($p \sim T$: decreasing pressure with decreasing temperatures).
Besides the tests described above, the frame was used for a preliminary EMC test and was shown to effectively block electromagnetic radiation.

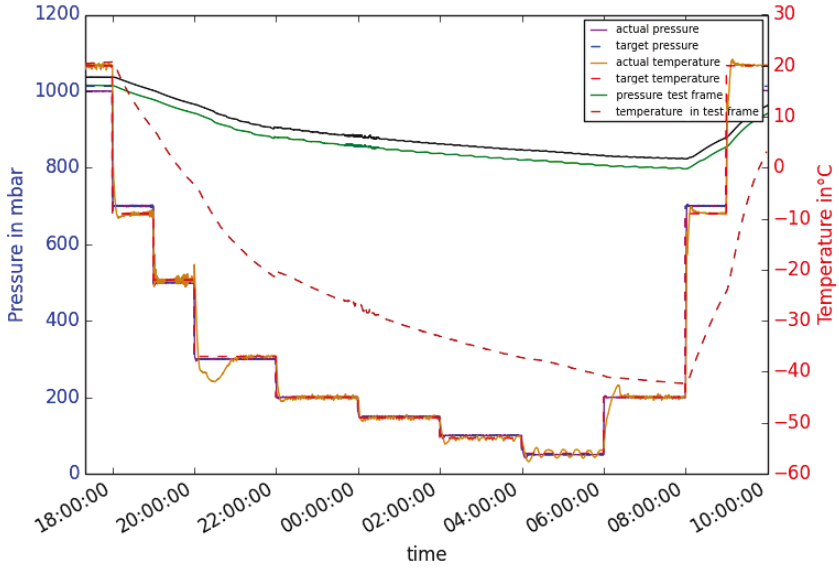


**Figure 3.19:** Observed parameters during the pressure tightness testing of the test frame. During the 17 h flight simulation program in the climate chamber, pressure and temperature values are regulated in 1 - 2 h steps. The first four label descriptions refer to target and actual measured climate chamber values, as 'ambient conditions'. The two lines (black and green, close together) show the test frame pressure, measured with two different pressure sensors (MKS). The dotted line shows the temperature in the test frame.

**Pressure tightness of the delivered instrument AMICA:** the components investigated with the test frame were proven to function appropriately. However, two big connectors at the bottom of the pressure tight enclosure were leaking. After applying 1 bar over pressure into the box, the pressure immediately decreased to ambient pressure. Because there was not enough time before the first StratoClim measurement campaign in Kalamata, AMICA could impossibly fly with such large leaks. Consequently, the connectors were made pressure tight with adhesives.

### 3.6.3 Flight simulation experiment with AMICA

Between the first test campaign in Kiruna without any previous measurement flights and the first real StratoClim measurement campaign, AMICA together with the designed inlet for the Geophysica were tested in a climate chamber under low temperature (down to -40 °C) and low pressure (down to 50 hPa) conditions. Flight simulation tests with the final instrument are crucial before a real measurement flight to exclude as many interferences as possible. The mechanical

design of AMICA is described in Chapter 3.5. Because of AMICAs dimensions, it does not fit in the climate chamber of IEK-7. An alternative chamber was found at IABG (Industrieanlagen-Betriebsgesellschaft mbH, Ottobrunn, Germany). They own a vacuum chamber with effective interior dimensions of 6m × 3m × 3m, with a temperature range from 80 °C to -70 °C, reaching pressures down to 50 hPa. Pictures of AMICA and the sample inlet in the vacuum chamber are shown in Figure 3.20. Although the previous valve tests described in Chapter 3.6.1 specific valve orifices were found to be necessary, in the delivered mechanical design of AMICA both implemented valves had orifices of 1 mm diameter (Parker, Porter valve) and the flight simulation was carried out with them. The monitored ambient pressure of the vacuum chamber together with the cell pressure in AMICA are shown in Figure 3.21. The experiment shows that the two valve system regulates the cell pressure to 47 hPa (35 torr) successfully down to an ambient pressure of 150 hPa, the point where the cell pressure continuously starts to drop. At this point the experiment was interrupted to replace one, with a bigger 2.4 mm orifice diameter ASCO valve. This valve changing phase is shown in Figure 3.21 and can be identified by the sudden cell pressure increase up to 110 hPa (83 torr), which is the limitation of the pressure sensor (honeywell 1406405, specification to 69 hPa). With the new set up, the cavity pressure regulation worked down to an ambient pressure of 132 hPa and continuously decreased again after this point. The reason for the pressure drop was mainly an implemented filter (Swagelok 2 $\mu$m), which represented the highest flow resistance and was exchanged for the measurement flights.

Besides the valve set up in AMICA, the anti-ice heater of the inlet was also investigated. The configuration of the inlet heating is set to start when outside temperatures decrease below 10 °C. In the vacuum chamber the position of the inlet was chosen according to the airflow, the airflow direction is visulized in Figure 3.20b.

Comparisons show that the temperature at the inlet is higher than the ambient temperature, measured in the chamber (up to 40 °C higher), demonstrating that the inlet system heating works.

The pressure in the enclosure (pressurized box of AMICA, c.f. Chapter 3.6.2) was also monitored. The lowest pressure measured during the seven hour operation was 870 hPa, which indicated a small, but tolerable leak. The temperature in the power box increased up to 70 °C, at the lowest pressure with the least heat conductance. Component failures occur at temperatures higher than 80 °C, thus 70°C is acceptable for this experiment. The performance under warmer conditions is questionable. As seen in Figure 3.21 the temperature regulation by the supercoolers inside the pressure tight enclosure of AMICA continuously heated the enclosure. The sudden decrease can be explained by opening the cover, when ambient air streamed into the enclosure. It took ∼3 hours for the temperature to rise up to 40 °C.

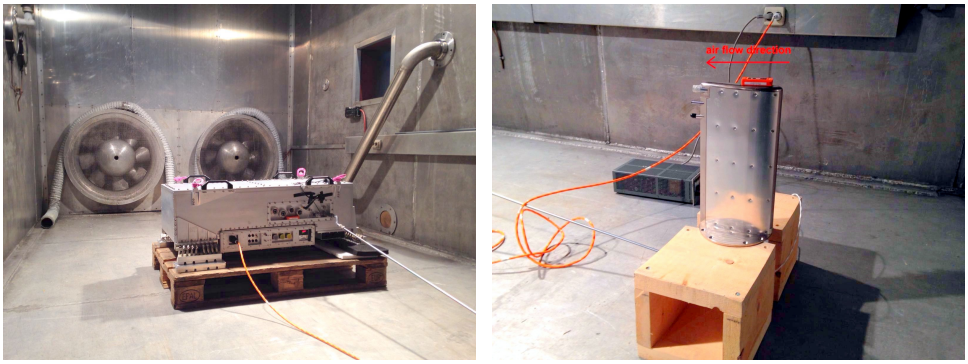


(a) (b)

**Figure 3.20:** Two photographs showing the set up of AMICA and the inlet, used for the flight simulation experiment, in the vacuum chamber of IABG in Ottobrunn, Germany. (a) AMICA in the vacuum chamber of IABG and (b) the inlet designed for the research aircraft Geophysica in the vacuum test chamber.

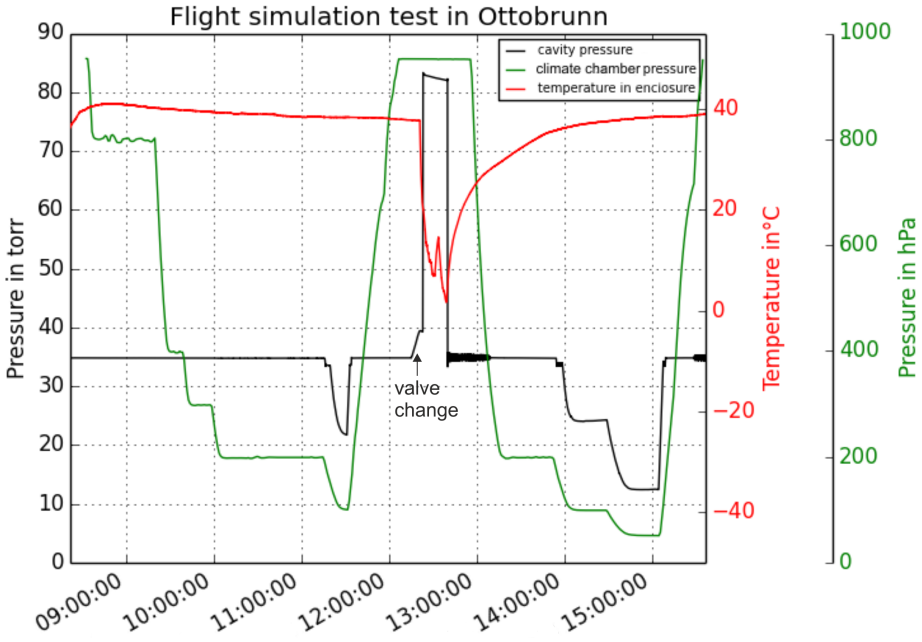


**Figure 3.21:** The observed ambient pressure in the vacuum chamber (at IABG May $18^{th}$ 2016) together with the cell pressure of AMICA, which should be regulated to 47 hPa (35 torr).

Some crucial conclusions can be drawn from this flight profile test at IABG with AMICA:

- Unforeseen errors and failure of electrical or mechanical components did not occur and AMICA measured for any pressure and temperature condition (down to -40 °C and 50 hPa).
- The larger orifice valve had to be exchanged for the first measurement campaign to ensure accurate cell pressure regulation for ambient pressures down to 55 hPa.
- The anti ice inlet heating functioned well.
- The pressure tight enclosure stayed sufficiently pressure tight during the experiment.
- The enclosure temperature regulation by TECs, with a set point of 40 °C functioned, but did not perform well.
- All components in the power box worked throughout the experiment at temperatures up to 70 °C.
- The valve set up during this experiment did not maintain the pressure in the measurement cells at a constant level. Therefore, the flow resistance needs to be minimized for the measurement flights, by exchanging valves, but also exchanging implemented filters.

## 3.7 AMICA performance

### 3.7.1 Performance of AMICA during first measurement flights

AMICAs first flight operation took place in Kalamata Greece, within the first campaign phase of StratoClim. Three measurement flights were carried out on August $30^{th}$, September $1^{st}$ and September $6^{th}$ 2016 and AMICA measured throughout all of them.
At the campaign site, the larger valve was disabled prior to the first flight, because of electronic problems and only the smaller valve regulated the pressure inside the cavities, which dropped below the target 47 hPa at ambient pressures below 200 hPa. During the second flight, both valves operated, but the pressure inside the cavities dropped down to 12 hPa (9 torr) as shown in Figure 3.22a. One possible reason was a filter, limiting the flow, which was exchanged. During the next measurement flight the pressure dropped down to 21 hPa (16 torr) (Figure 3.22b), however this is still not satisfactory. The main cause was a reduced effective ambient pressure at the inlet (see Picture 3.14) on top of the aircraft. The attack angle of the aircraft and the spikes in cavity pressure (e.g. in Figure 3.22a at around 10 a.m.) correlate and the pressure at the inlet depends on the aircraft position during flight. While the lowest pressure level recorded with the research aircraft Geophysica is 55 hPa, the effective pressure at the inlet position can therefore be much lower (down to around 35 hPa). The flow system would have maintained the pressure inside the cavities to 47 hPa at 55 hPa ambient pressure at the inlet, however, it cannot regulate the pressure with lower inlet pressures. The COLD instrument, drawing air from the same inlet, suffered from the same issue. The internal software of the AMICA instrument is not able to

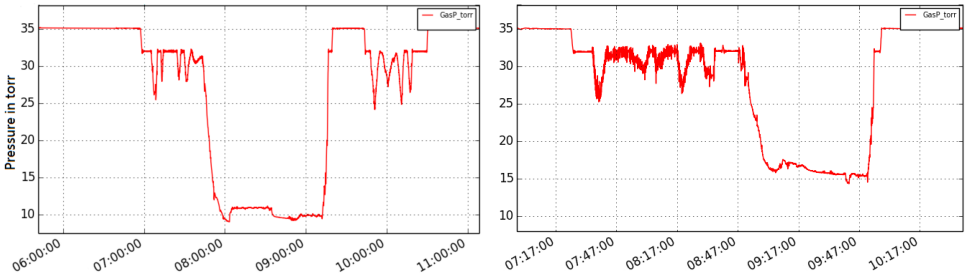


(a) (b)

**Figure 3.22:** Cavity pressure in AMICA throughout (a) the second measurement flight, September $1^{st}$ and (b) the third measurement flight, September $6^{th}$ in Kalamata, Greece 2016.

account for such pressure drops in the cell for accurate mixing ratio determinations. Therefore, mixing ratios were retrieved from raw spectra using a spectral model, developed at IEK-7 based on HITRAN line parameters that fully account for the actual pressure and temperature in the cavity.

The pressure in the AMICA enclosure drops throughout the flight from 1000 to $\sim$ 810 mbar, which is tolerable, considering the implemented connectors, which were not pressure tight and have only been made as pressure tight as possible using adhesive (c.f. Chapter 3.6.2). The temperature in the enclosure drops from $\sim$ 28 °C to $\sim$ 22 °C. The temperature drop in the enclosure has been identified to be caused by i) a very high internal heat and power dissipation on the board, controlling the thermoelectric cooler (TEC) units and ii) an inadequate position of the temperature sensor, used for the control circuit. Both issues have been solved after the campaign.

During necessary EMC tests of the Geophysica aircraft during the campaign, AMICA shut down a few times due to what was thought to be overheating. Temperatures in the power box increased up to 80 °C after a few minutes of operation on top of the aircraft in the sun (ambient temperatures of around 30 °C). To avoid an early shut down during a measurement flight (and especially before take off), AMICA was switched on as close as possible to take off. The respective preflight procedure is listed in Table 3.2.

Although a number of complications appeared during the first measurement campaign with AMICA, a working new instrument on its first mission, delivering data, is a success.

First measurement results from AMICA on its first measurement campaign in Kalamata, are presented in Chapter 4. The second measurement flight is chosen for data analysis because of a compromise of strengths and weaknesses of the measurements throughout the three flights:

- $1^{st}$ measurement flight: due to the lowest cavity pressure observed throughout the first measurement flight, the precision of AMICA was worst.
- $2^{nd}$ measurement flight: the precision performance of AMICA was better than during the

**Table 3.2:** The pre-flight procedure for AMICA in Kalamata, Greece.

| Time prior to take off | Action | Comment |
|---|---|---|
| T0 - 40 min | Switch on AMICA and Wifi | |
| T0 -35 min | Switch off AMICA | Instructed by PI |
| T0 -20 min | Pilot takes his seat | |
| T0 -10 min | Switch on AMICA | Done by the pilot |

first flight and no temperature instabilities occurred. Hence, this flight was chosen for a data analysis of the AMICA measurements.

- $3^{rd}$ measurement flight: because of the best cavity pressure regulation, the precision during this flight was best, however temperature instabilities at the laser occurred (c.f. Chapter 3.2).

In July/August 2017, the main StratoClim campaign for the investigation of the Asian monsoon took place in Kathmandu, Nepal. Throughout all eight measurement flights on the Geophysica, AMICA performed measurements without any complications. AMICA now reliably performs $OCS$, $CO$, $CO_2$ and $H_2O$ measurements during measurement campaigns on the research aircraft Geophysica. Collected data from the Kathmandu campaign are currently being processed and analyzed and are therefore not presented in this work.

### 3.7.2 OCS calibration

Before and after the first measurement campaign with AMICA, several calibrations were carried out, using the combination of NOAA $OCS$ standard and permeation system, described in Chapter 3.3.3 (equivalent to the calibration presented in Chapter 3.3.4). Figure 3.23 presents a combination of calibrations after the first measurement campaign. During operation AMICA saves measurement values that are internally analyzed by a software, provided by LGR and also the raw spectra. This feature allows to analyze the spectra after operation separately. The blue data points with standard deviation result from the AMICA $OCS$ data output from the internal analysis software (provided by LGR). For those values a correction equation of 0.73x - 90.6 ppt is calculated. As a comparison the equivalent MICA measurement points are added in green with standard deviation. At the moment, the MICA measurements (from the internal spectra analysis by LGR) are closer to the gravimetric calculated values (with a relative difference of up to 12 %) than the AMICA data point (with a relative difference of up to 40 %). However, the external spectra analysis delivers AMICA $OCS$ measurements that agree well with the gravimetric values within the standard deviation. Due to the pressure problems in the cavities during flight (c.f. Chapter 3.7.1), the calibration with the measurements from the external spectral analysis (presented in cyan) are carried out during different pressure conditions in the cell: at 47 hPa

and at $\sim$ 18 hPa (which was roughly observed during the flight). Even with lower pressures in the cavity, measurements from the external spectral analysis agree well with the expected values. Hence, this gives confidence in the AMICA measured $OCS$ data during flight, which are presented in Chapter 4.

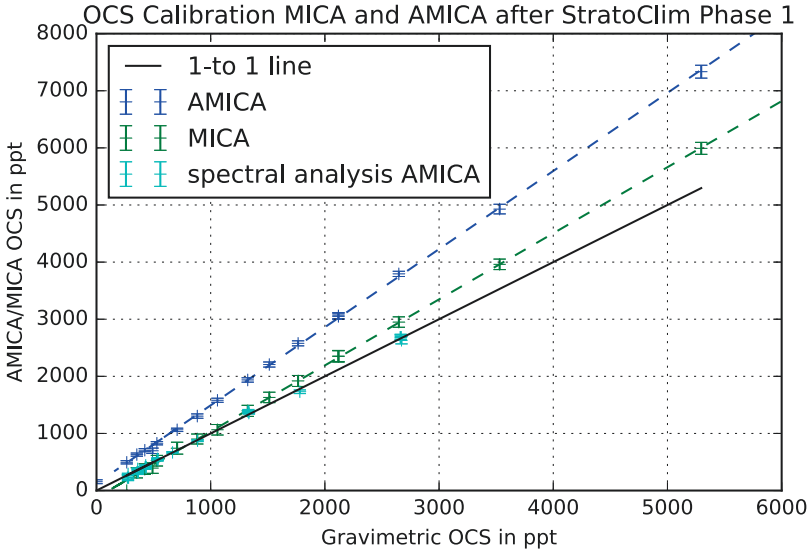


**Figure 3.23:** AMICA (blue) and MICA (green) $OCS$ measurement values together with their linear fit. The black one- to- one line represents the desired measurement outcome of the instruments with no deviation from the gravimetric values. Error bars for all measurements are indicated. The resulting correction function for MICA is: 0.73x - 90.6 ppt. Cyan crosses represent the AMICA measurements, separately analyzed from the measured spectra.

# Chapter 4

# AMICA results

During the first phase Campaign of the EU-project StratoClim in Kalamata, Greece, three measurement flights were carried out. The main campaign in the Asian monsoon region was originally planned for 2016 in India, however, due to flight permission issues it was shifted to July/August 2017 in Nepal. A first campaign phase, planned in April 2016 in Kiruna, mainly aiming to test the instrument during flight, did not take place as well due to political constrains. While the purpose of the main campaign is the investigation of the Asian monsoon as a transport pathway into the stratosphere, the goal of the Kalamata campaign was

1. Testing of the instruments, especially of the new instruments as for example AMICA, operated in flight for the first time.

2. To gather data in possibly Asian monsoon influenced air masses (outflow of the Asian monsoon) for data analysis.

In this Chapter, AMICA's first measurements together with scientific results during this campaign are presented.

## 4.1 Measurements

As discussed in Chapter 3.7.1, AMICA measured successfully at the StratoClim campaign in Kalamata throughout all three flights from take off to landing.
Figure 4.1 shows the time series for the three complete flights performed on August $30^{th}$, September $1^{st}$ and September $6^{th}$ 2016. The aircraft altitude (gray) is shown together with the measured trace gases $OCS$ (black), $CO$ (red) and $H_2O$ (blue). $CO_2$ has been detected, however due to base line issues the retrieval for $CO_2$ is still in process. $H_2O$ mixing ratios below 100 ppm cannot be accurately measured by AMICA, therefore Figure 4.1 only shows $H_2O$ mixing ratios above 100 ppm. A decreasing water mixing ratio with increasing altitude is observed. $H_2O$ mixing ratios agree within 20 % with the established water vapor instrument FISH (Fast In situ Stratospheric

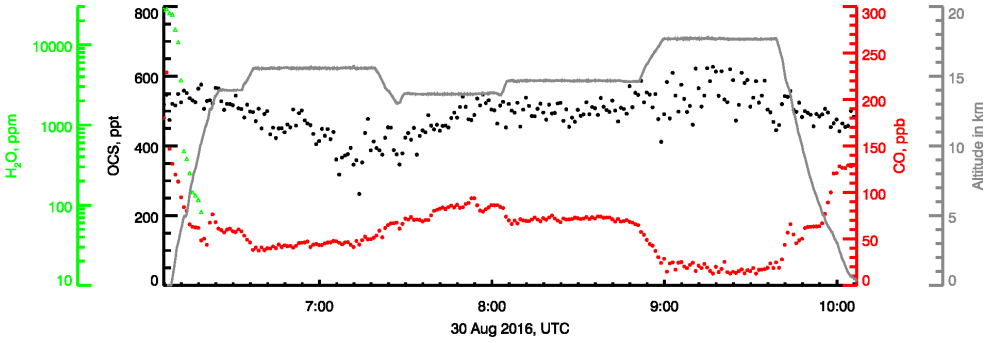


(a) $1^{st}$ measurement flight

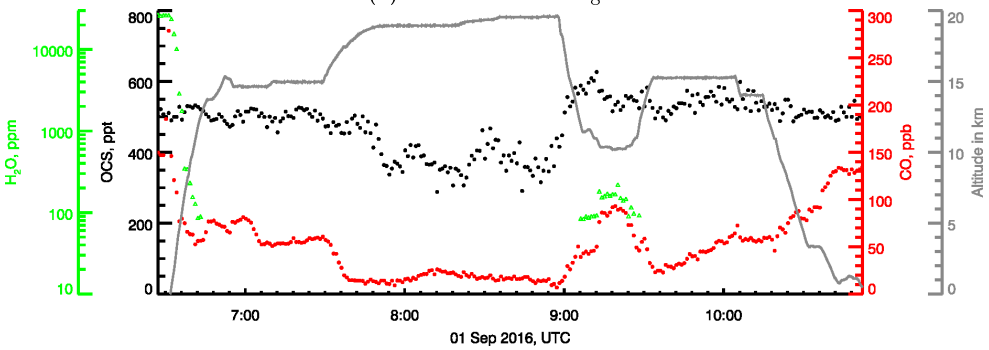


(b) $2^{nd}$ measurement flight

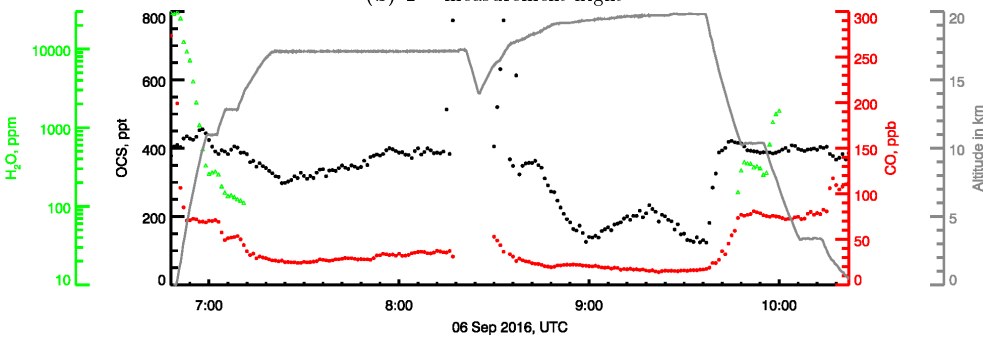


(c) $3^{rd}$ measurement flight

**Figure 4.1:** Measurements of $CO$, $OCS$ and $H_2O$ during all three campaign flights in Kalamata, Greece, 2016 performed with AMICA. The geometric altitude (from the Geophysica avionic data) are shown in gray.

Hygrometer Zöger et al. (1999)) on the Geophysica. Similar features are seen with $CO$, with highest values at ambient ground conditions, with mixing ratios at around 150 ppb, decreasing with increasing altitude and vice versa. $CO$ mixing ratios agree within 10 % compared to the $CO$ measurement instrument COLD (Viciani et al., 2008), which is also implemented on the Geophysica. $OCS$ mixing ratios remain fairly constant at 500 - 600 ppt and decrease to around 400 ppt at altitudes of 19 - 20 km.

## 4.2 OCS and CO in the UTLS and stratosphere

Vertical profiles of the measurements for $CO$ and $OCS$ from the second measurement flight, on September $1^{st}$ 2016 from AMICA are shown in Figure 4.2. Mixing ratios are plotted against altitude in km (Figure 4.2a), potential temperature in K (Figure 4.2b) and potential vorticity (Figure 4.2c), as different vertical coordinates. The geometric altitudes are taken from the avionic data. The potential temperature (theta) is calculated from pressure and temperature values from the avionic data, potential vorticity is extracted from the ERA-Interim, ECMWF data set. Potential vorticity and potential temperature are suitable coordinates especially in the stratosphere, giving additional subdivisions. Furthermore, the dynamical tropopause is defined by those parameters: At 380 K in the tropics and at 3.5 PV in the extra-tropics, indicated with the blue dashed line in Figure 4.2b and 4.2c. The flight path during the second measurement flight in Kalamata together with the occurring ECMWF dynamical tropopause height on a 1° by 1° grid is visualized in Figure 4.3. The tropopause height in km is highly variable along one flight track (from 11 - 16 km), as seen in Figure 4.3. Clearly the measurement flight took place in a region of a steep tropopause height gradient, from tropical tropopause heights of (16 - 18 km) down to subtropical values (lower than 13 km). Because of this variability in tropopause height, one single value is not accurate for the geometrical tropopause height determination, therefore it is not indicated in Figure 4.2a.

Each $CO$ and $OCS$ point in Figure 4.2 represents a one minute average value from the AMICA measurements. The general trend of $CO$ and $OCS$ with height is visible in all three plots, decreasing mixing ratios with increasing altitude.

For $OCS$, mixing ratios remain fairly constant in the troposphere between 500 and 600 ppt, due to the long photochemical lifetime of 36 years in the troposphere (Chin and Davis, 1995) and decrease in the stratosphere. This general $OCS$ distribution, constant in the troposphere and decreasing in the stratosphere has already been shown in Chapter 2.3.3 with the ACE-FTS data set (Figure 2.16). In the stratosphere, $OCS$ mixing ratios decrease very slowly up until $\sim$ 18 km, 440 K and 18 PV, because the photochemical lifetime above the tropopause, in the lower stratosphere is still high.

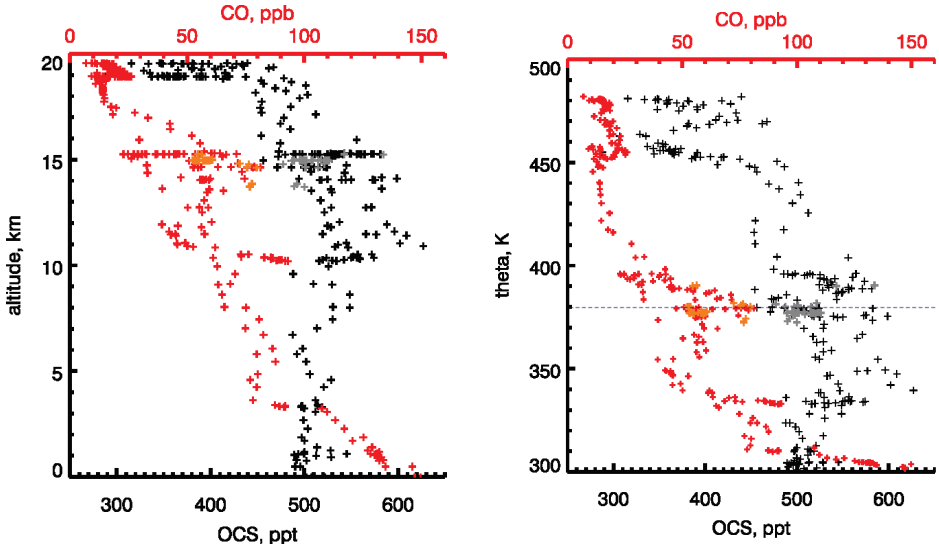


(a) Altitude

(b) Potential temperature

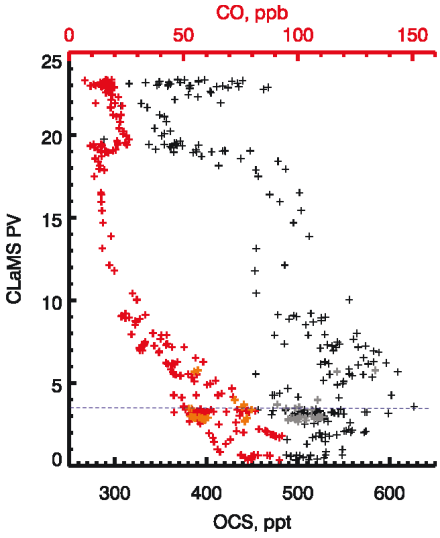


(c) Potential vorticity

**Figure 4.2:** Vertical profiles from AMICA's first operation, from the measurement flight (01/09/17), plotted for different altitude coordinates. *CO* values are indicated with red crosses and *OCS* values with black crosses. Orange crosses indicate *CO* and gray crosses *OCS* measurement values of possibly Asian monsoon influenced air.

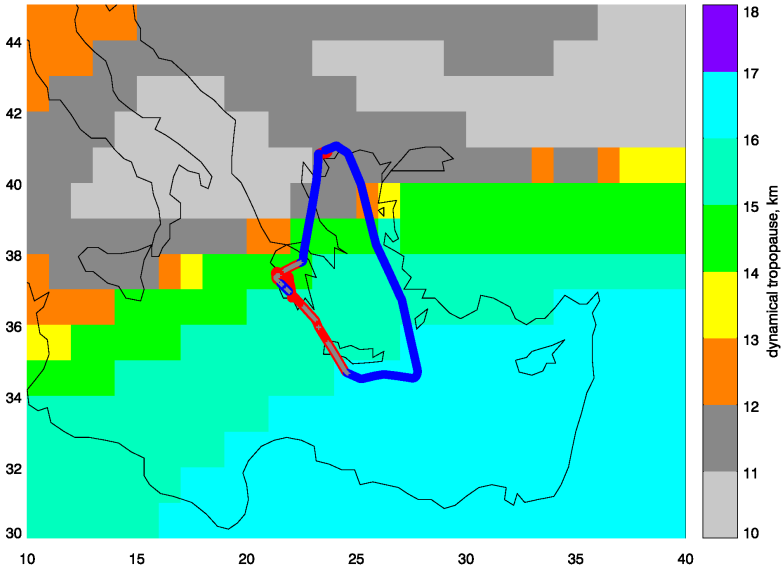


**Figure 4.3:** Flight track during the second flight (01/09/17) in Kalamata together with the ECMWF dynamical tropopause distribution. The flight path is shown in blue and red. Blue indicates that the aircraft was in the stratosphere and red that it was in the troposphere. Gray lines throughout the flight path, indicate possible Asian monsoon influenced air masses during flight.

As seen in Figure 4.2a, the $OCS$ mixing ratios decrease at about 20 km, in the PV based display of $OCS$ in Figure 4.2c at 17 to 20 PV. The steeper vertical gradient of $OCS$ at this altitude range points to a mixture of air masses, with $OCS$ mixing ratios spanning from 500 ppt down to 350 ppt. The higher mixing ratios measured indicate that air masses are not photochemically depleted yet. This is a result of the natural circulation between the lower stratosphere and the UTLS region, which leads to a total mean stratospheric lifetime of $64 \pm 21$ years (Barkley et al., 2008) (higher in the lower stratosphere, lower in higher altitudes). Lower $OCS$ mixing ratios down to 350 ppt at this altitude range, indicate a strong contribution of aged, more photochemically depleted air masses, which is a result of the transport processes occurring (c.f. Chapter 1.2.1). Measured air masses have likely been through the tropical pipe and have been transported along the tropopause in the lower stratosphere to higher latitude levels.
$CO$ has a shorter photochemical lifetime in the troposphere, which is latitude dependent from 1 month to 1 year (Staudt et al., 2001). It decreases with height in the troposphere from around 150 ppb in the boundary layer to around 50 ppb at the tropopause, decreasing further with altitude, potential temperature and potential vorticity in the stratosphere. Especially the potential temperature representation in Figure 4.2b of $CO$ shows increased mixing ratios at around 380 K in the UTLS region. This feature indicates a fast vertical transport in this area.

Another interesting feature, seen in Figure 4.2b and 4.2c, is a sudden increase of $CO$ mixing ratios at around 450 K and 20 PV, pointing to a stratospheric source of $CO$ at this range. Photochemical loss by oxidation to form $CO_2$ is the stratospheric sink for $CO$. In the stratosphere and mesosphere, above 30 km altitude (10 hPa pressure level), oxidation with $CH_4$ is a stratospheric source for $CO$ (Pommrich et al. (2014) and Minschwaner et al. (2010)). $CH_4$ has only tropospheric sources and a long stratospheric lifetimes (195 $\pm$ 135 years (Brown et al., 2013)). In the upper mesosphere and lower thermosphere (75 - 100 km) production of $CO$ via $CO_2$ occurs. The increase of $CO$ mixing ratios at around 450 K and 20 PV (around 20 km altitude) must be a result of a mixture of air masses partly from higher altitudes ($>$ 30 km), with elevated $CO$ levels from $CH_4$ oxidation.

## 4.3 Asian monsoon influence

Besides the general trend of $CO$ and $OCS$ with altitude, potential temperature and potential vorticity, some points with a high probability of Asian monsoon influence (i.e. outflow of the Asian monsoon anticyclone) are indicated with slightly different colors (orange for $CO$ and gray for $OCS$ measurements). The criteria for selecting AMICA $OCS$ and $CO$ data with a high probability of Asian monsoon influence are chosen according to Figure 8 from Ploeger et al. (2015). Orange and gray points are extracted with those criteria: (PV $<$ 6 and theta $>$ 390) or (PV $<$ 4 and theta $>$ 380) or (PV $<$ 3 and theta $>$ 370) or (PV $<$ 1.5 and theta $>$ 360). Those are purely dynamical criteria, no back-trajectories have been considered. From Figure 4.2b and 4.2c it is seen that all potentially Asian monsoon anticyclone influenced air masses are situated in the UTLS region. Especially in Figure 4.2b the orange $CO$ values are increased compared to most of the remaining red points, supporting the suggestion of a fast transport in this area, responsible for the increased $CO$ mixing ratios in the UTLS. Increased $CO$ values in the Asian monsoon anticyclone have already been shown with the ACE-FTS data set in Chapter 2.4. AMICA observations do not show a clear increase of $OCS$ mixing ratios in Asian monsoon influenced air masses. In the ACE-FTS data set, $OCS$ is significantly increased in the Asian monsoon anticyclone (Chapter 2.4), however, the variability of $OCS$ mixing ratios in the anticyclone from ACE-FTS is higher than for $CO$ and $HCN$.

## 4.4 A first AMICA and ACE-FTS comparison

During the StratoClim campaign phase 1 in Kalamata, AMICA made measurements on the research aircraft Geophysica as presented in Chapter 4.1, as well as ACE-FTS delivered some measurement profiles in the wider region. Kalamata is at 37° latitude and 22° longitude. The measurement flight presented here took place September $1^{st}$ 2017 (from about 6:30 a.m. to about 10:45 a.m. UTC).

The ACE-FTS profile chosen for comparison is from September $4^{th}$ 2017 at 34.6 ° latitude and 27.1 ° longitude (time: 03:51 a.m. UTC). This profile was chosen as compromise between closest location to the performed measurement flight and time difference between measurement flight and the ACE-FTS profile measurement. Figure 4.4 visualizes position and time of both, the chosen ACE-FTS profile and the AMICA measurement flight path, together with time and location of two other possible ACE-FTS profiles. Other ACE-FTS profiles, measured closer in time to the measurement flights in Kalamata lay outside of the chosen area, seen in Figure 4.4 and are therefore not selected.

Figure 4.5 shows the comparison between the chosen ACE-FTS profile and the AMICA measurements as presented before. The AMICA measurements are averaged in 1 km altitude bins over the entire flight. The same vertical coordinates as in Figure 4.5a are used: altitude, potential temperature (Figure 4.5b) and potential vorticity (Figure 4.5c). The potential temperature data are available from the ACE-FTS data set and have been extracted for the $CO$ and $OCS$ ACE-FTS data. The potential vorticity data are extracted from the Era Interim data set from ECMWF and added to the ACE-FTS data. As before, the tropopause definition is indicated with a blue dashed line in Figure 4.5b and 4.5c.

Taking into account the spacial and temporal differences of the measurement profiles and the very different origin of air masses especially in the region between 8 and 15 km, the observed large deviations in the troposphere between ACE-FTS and AMICA measurements are not surprising. The $OCS$ variability observed with AMICA is indicated with the standard deviation, error bar in Figure 4.5. In the stratosphere, $OCS$ mixing ratios agree well, as seen in Figure 4.5a, 4.5b and 4.5c. However, the mean $OCS$ mixing ratios from AMICA are consistently higher than the ones from ACE-FTS. Comparing ACE-FTS and AMICA $OCS$ measurements at equivalent potential temperatures and potential vorticities, ACE-FTS $OCS$ mixing ratios are around 11 % (5 - 19 %) lower than the mean value of all AMICA $OCS$ (per 1 km bin) measurements in the UTLS. In the stratosphere (up to 500 K) ACE-FTS $OCS$ values are between 5 and 14 % lower than the mean of the AMICA $OCS$ measurements. A comparison between MIPAS $OCS$ and ACE-FTS $OCS$ data also showed lower $OCS$ mixing ratios from ACE-FTS, the highest difference of 75 - 100 ppt is observed at 14 km (Glatthor et al., 2017). This low bias is also confirmed by Velazco et al. (2011) with balloon profiles (MkIV) with a 15 % lower ACE-FTS $OCS$ value at 12 - 23 km altitude (comparison measurements took place in 2004 and 2005) and by Krysztofiak et al. (2015a) with another balloon borne instrument (SPIRALE), with a lower ACE-FTS OCS value of up to 20 % below 22.5 km altitude. The observed low bias of ACE-FTS for $OCS$ measurements in the UTLS and stratosphere from Glatthor et al. (2017), Velazco et al. (2011) and Krysztofiak et al. (2015a) agrees with the bias observed with AMICA.

In the altitude and potential temperature (and mostly in the potential vorticity) display of the ACE-FTS and AMICA $CO$ data, $CO$ mixing ratios from AMICA are consistently lower than from ACE-FTS in the stratosphere. However, considering the high standard deviation of up to

± 30 % of the 1 minute averaged AMICA *CO* measurements throughout the flight, AMICA *CO* values and ACE-FTS *CO* values agree very well in the UTLS and stratosphere up to 500 K. The following differences between ACE-FTS and AMICA *CO* values are based on the mean *CO* values (averaged in 1 km altitude bins). In the UTLS region ACE-FTS *CO* measurements are ∼ 15 % higher than AMICA *CO* values and in the stratosphere (up to 500 K) ACE-FTS *CO* values are around 11 % higher (7 - 57 %). A *CO* comparison by Velazco et al. (2011) shows a similar difference with higher ACE-FTS *CO* values in the upper troposphere of 6.3 - 12.4 %. However, in the lower and mid stratosphere, they see lower ACE-FTS *CO* values by 6.0 - 17.8 % for the years 2004 and 2005.

Increased *CO* mixing ratios in the UTLS region due to fast transport including Asian monsoon influence observed with the AMICA data set, is also seen with the ACE-FTS *CO* data, especially in Figure 4.5c at 3.5 PVU.

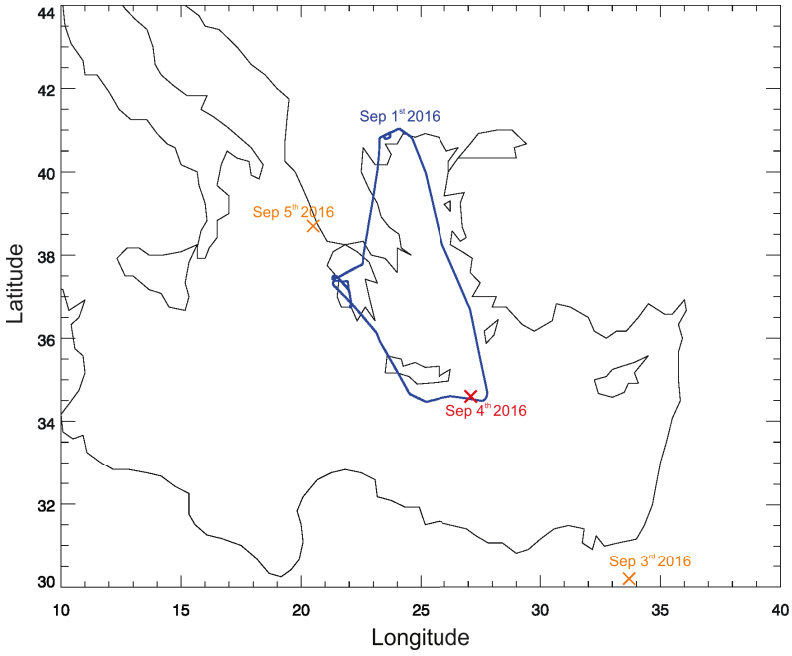


**Figure 4.4:** Comparison of the locations of the ACE-FTS profile and flight path during the second flight (01/09/17) in Kalamata. The flight path and date of the measurement flight is indicated in blue. Possible locations of ACE-FTS measurement profiles close to the flight path are indicated in yellow and red, where red is the profile, chosen for comparisons here.

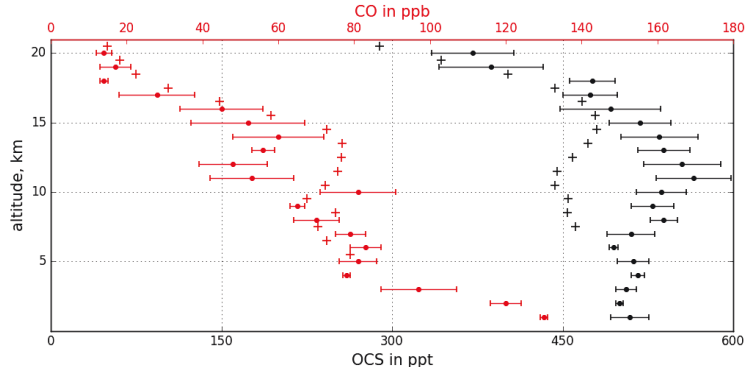


**(a)** Altitude.

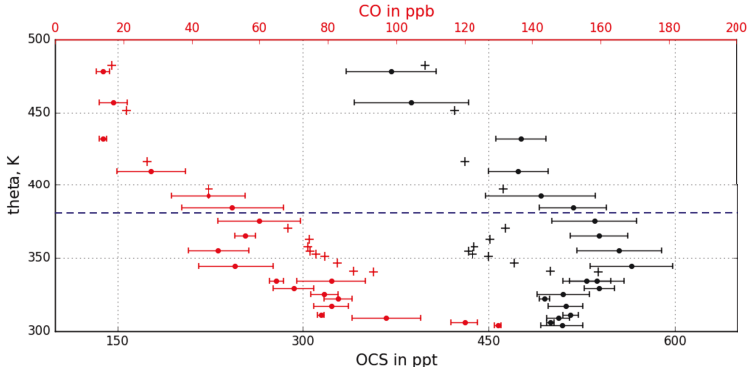


**(b)** Potential temperature.

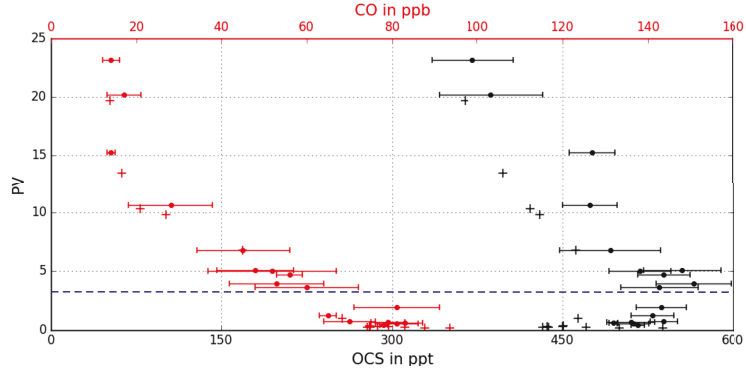


**(c)** Potential vorticity.

**Figure 4.5:** AMICA mean values per 1 km height (dots) compared with an ACE-FTS profile (crosses). The standard deviation of all AMICA measurements in 1 km altitude range, is indicated with the error bars.

# Chapter 5

# Conclusions and outlook

In this thesis stratospheric $OCS$ mixing ratios were investigated using in-situ high resolution data from the Airborne Mid-Infrared Cavity enhanced Absorption spectrometer AMICA and the satellite based data set Atmospheric Chemistry Experiment ACE-FTS. The key aspects and findings of this work are listed below:

- *The stratospheric $OCS$ burden*: For the first time, the global coverage of the ACE-FTS data set was used to calculate a stratospheric burden of $OCS$. 524 Gg of $OCS$ is the stratospheric burden for the year 2015, which is equivalent to 280 Gg of sulfur from $OCS$. Throughout the ACE-FTS measurement time frame, the stratospheric annual budget varies by about 6 %. Compared to the total atmospheric $OCS$ budget of $5.34 \cdot 10^{12}$ g (Barkley et al., 2008), 10 % is situated in the stratosphere. 524 Gg of $OCS$ burden in the stratosphere is equivalent to 280 Gg of sulfur from $OCS$. A global sulfur transport model by Sheng et al. (2015) gives a stratospheric sulfur burden value from $OCS$ of 283.1 Gg. This excellent agreement gives a lot of confidence towards the representation of $OCS$ in the transport model by Sheng et al. (2015).
- *The stratospheric burden trend*: during the ACE-FTS measurement phase until now (2004 - 2016) no significant trend in stratospheric $OCS$ is detected. This is in agreement with MIPAS $OCS$ observations.
  - *Contribution to a collaborative sulfur burden study*: the ACE-FTS $OCS$ stratospheric burden analysis done in this work is contributing to a collaborate study on stratospheric sulfur burden, an assessment based on gas and particle phase measurements, lead by Terry Deshler (expected to be published in 2018).
- *An approach for a sampling bias correction*: compared to other satellite data products (e.g. MIPAS), ACE-FTS measurements exhibit a larger sampling bias in seasonal and regional means, due to insufficient and often inhomogeneous spatial and temporal coverage. In this work a robust approach was developed and validated in collaboration with Bodeker Scientific to correct for this sampling bias. This approach has the big advantage of only

using the information that can be extracted from the ACE-FTS data set. The new budget values, which account for the sampling bias, are in some cases (close to the poles, in seasons with only a few measurements) significantly increased. However, using the burden values from the ACE-FTS measurements alone does not lead to different conclusions. The magnitude of the calculated sampling bias was verified with the MIPAS data set. Until now the sampling bias (which occurs especially with solar occultation instruments) is not corrected for in global climate studies. Thus the here presented procedure and a further development of this approach is of benefit to multiple applications.

- *$OCS$ mixing ratios in the Asian monsoon anticyclone*: using the ACE-FTS $OCS$ data from all available years during the Asian monsoon time, a clear increase of $OCS$ and also $HCN$ and $CO$ mixing ratios in the Asian monsoon anticyclone is observed. An increase of $CO$ mixing ratios in Asian monsoon influenced air masses is also seen with AMICA during the first phase StratoClim campaign in Kalamata, Greece. A clear increase of $OCS$ mixing ratios, however, is not detected with AMICA.
- *Transport processes in the Asian monsoon region*: The proposal that the convection from the Bay of Bengal region is mostly transported outside, along the southern border of the anticyclone is supported by a $HCN$, $CO$ and $OCS$ comparison. $HCN$ has a strong ocean sink, other than $OCS$ and $CO$. Less enhanced $HCN$ mixing ratios are found in the area that is defined to be mostly outside on the southern border of the anticyclone.
- *Development of AMICA*: a novel Airborne Mid-Infrared Cavity enhanced Absorption spectrometer AMICA was developed, measuring $OCS$, $CO$ and $H_2O$ mixing ratios in-situ on board of the research aircraft Geophysica. Until now, AMICA operated successfully throughout all three measurement flights of the first phase StratoClim Campaign in Kalamata, Greece. During the development of AMICA some valuable and unique features were implemented:
  - *Flow system*: a pumped two-valve-sampling system was developed, allowing for a stable pressure inside the measurement cells over a wide ambient pressure range from $\sim 50$ to $> 1000$ hPa.
  - *Pressure tight enclosure*: to protect the interior, electronic components and to allow for temperature regulation in the AMICA enclosure, the enclosure had to be built pressure tight. The development of an 80 L box-shaped pressure tight enclosure with a construction including screws and adhesive, is a space and weight saving new approach.
  - *Second measurement cell*: two measurement cells allow for the scanning of two wavelength regions and thus potentially for the simultaneous measurements of additional trace gases. The most relevant additional compound of interest to be measured with AMICA is $HCN$. However, finding a suitable set up for ICOS $HCN$ measurements is challenging and still under development.

  - The mechanical design of AMICA, and also the electrical configuration of the instrument are also suitable for future campaigns on the German research aircraft HALO. Hence, measurement flights with AMICA on future HALO campaigns are possible.

- *First research results from AMICA*: in the UTLS region, $CO$ exhibits an increase in mixing ratio (from 40 ppb up to 80 ppb), which is suggested to originate from fast transport processes. Especially air masses that are suggested to be influenced by the Asian monsoon, show increased $CO$ mixing ratios. A clear increase of $OCS$ mixing ratios of the same Asian monsoon influenced measurement points are not observed with AMICA. A steep vertical gradient in $OCS$ mixing ratios at around 20 km altitude is a result of the measurement of air masses, with more depleted components, resulting from a transport through the tropical pipe, mixed with air masses that have just been transported into the stratosphere.
- *AMICA and ACE-FTS measurements together in a comparison*: although there was no ACE-FTS measurement profile matching exactly in time and space data of the performed Geophysica flights, a few profiles were found that were close. $OCS$ and $CO$ values do not match in the well mixed troposphere; here the high variability in the troposphere and UTLS is probably too high. Consistently higher $OCS$ mixing ratios measured with AMICA are detected. This low bias of ACE-FTS has already been observed with other data sets, giving confidence in the AMICA measurements. $CO$ measurements in the stratosphere agree mostly within the standard deviation of the AMICA data points within 1 km altitude range.
- *StratoClim Asian monsoon campaign 2017*: considering the work that has been done on the ACE-FTS $OCS$, $CO$ and $HCN$ measurements in the Asian monsoon region, in-situ high resolution measurements with AMICA on Geophyisca in this area are of high relevance and were made in July/ August 2017 in Kathmandu, Nepal as the main campaign under the EU-project StratoClim. In general, transport processes from the Asian monsoon anticyclone were subject of interest during this campaign. However, the Nepal campaign rescheduled, AMICA data are currently processed and could not be considered in this work.
  - In general it will be investigated, to what extent theory and measurement data agree from where the air masses in the Asian monsoon anticyclone originate from.
  - Specifically for the AMICA $OCS$ measurements, a quantification of the increase and variability of $OCS$ in the Asian monsoon anticyclone that was also detected in this work with the ACE-FTS data set, will be performed.
  - A correlation of $OCS$ and $HCN$ measurements is of interest to better quantify the biomass burning source for $OCS$.

- *$OCS$ representation in global climate models*: with the increased knowledge from AMICA regarding $OCS$ transport and abundance in the atmosphere, an improvement of the understanding and representation in climate models can be realized. AMICA measurements show a high variability of $OCS$ in the UTLS region. Climate models, however, assume

constant $OCS$ mixing ratios of 500 ppt in the UTLS. A better understanding of the reasons for this $OCS$ variability will be achieved with further in-situ AMICA measurements and by using back trajectories of measured air masses. The improved understanding of the $OCS$ variability in the UTLS can therefore significantly improve the $OCS$ representation in climate models. For example, the following questions can be addressed: is 500 ppt in the UTLS a realistic value to be assumed for inter troposphere and stratosphere transport processes? And: how large is the source strength for $OCS$ from biomass burning?

# Bibliography

Bandy, A. R., Thornton, D. C., Scott, D. L., Lalevic, M., Lewin, E. E., and Driedger, A. R.: A time series for carbonyl sulfide in the northern hemisphere, Journal of Atmospheric Chemistry, 14, 527–534, doi:10.1007/BF00115256, URL http://dx.doi.org/10.1007/BF00115256, 1992.

Barkley, M. P., Palmer, P. I., Boone, C. D., Bernath, P. F., and Suntharalingam, P.: Global distributions of carbonyl sulfide in the upper troposphere and stratosphere, Geophysical Research Letters, 35, 2008.

Barletta, B., Meinardi, S., Simpson, I. J., Atlas, E. L., Beyersdorf, A. J., Baker, A. K., Blake, N. J., Yang, M., Midyett, J. R., Novak, B. J., McKeachie, R. J., Fuelberg, H. E., Sachse, G. W., Avery, M. A., Campos, T., Weinheimer, A. J., Rowland, F. S., and Blake, D. R.: Characterization of volatile organic compounds (VOCs) in Asian and north American pollution plumes during INTEX-B: identification of specific Chinese air mass tracers, Atmospheric Chemistry and Physics, 9, 5371–5388, doi:10.5194/acp-9-5371-2009, URL http://www.atmos-chem-phys.net/9/5371/2009/, 2009.

Bergman, J. W., Fierli, F., Jensen, E. J., Honomichl, S., and Pan, L. L.: Boundary layer sources for the Asian anticyclone: Regional contributions to a vertical conduit, Journal of Geophysical Research: Atmospheres, 118, 2560–2575, doi:10.1002/jgrd.50142, URL http://dx.doi.org/10.1002/jgrd.50142, 2013.

Bernath, P. F., McElroy, C. T., Abrams, M. C., Boone, C. D., Butler, M., Camy-Peyret, C., Carleer, M., Clerbaux, C., Coheur, P.-F., Colin, R., DeCola, P., DeMazière, M., Drummond, J. R., Dufour, D., Evans, W. F. J., Fast, H., Fussen, D., Gilbert, K., Jennings, D. E., Llewellyn, E. J., Lowe, R. P., Mahieu, E., McConnell, J. C., McHugh, M., McLeod, S. D., Michaud, R., Midwinter, C., Nassar, R., Nichitiu, F., Nowlan, C., Rinsland, C. P., Rochon, Y. J., Rowlands, N., Semeniuk, K., Simon, P., Skelton, R., Sloan, J. J., Soucy, M.-A., Strong, K., Tremblay, P., Turnbull, D., Walker, K. A., Walkty, I., Wardle, D. A., Wehrle, V., Zander, R., and Zou, J.: Atmospheric Chemistry Experiment (ACE): Mission overview, Geophysical Research Letters, 32, n/a–n/a, doi:10.1029/2005GL022386, URL http://dx.doi.org/10.1029/2005GL022386, l15S01, 2005.

Berry, J., Wolf, A., Campbell, J. E., Baker, I., Blake, N., Blake, D., Denning, A. S., Kawa, S. R., Montzka, S. A., Seibt, U., Stimler, K., Yakir, D., and Zhu, Z.: A coupled model of the global cycles of carbonyl sulfide and $CO_2$: A possible new window on the carbon cycle, Journal of Geophysical Research: Biogeosciences, 118, 842–852, doi:10.1002/jgrg.20068, URL http://dx.doi.org/10.1002/jgrg.20068, 2013.

Bodeker, G. E., Hassler, B., Young, P. J., and Portmann, R. W.: A vertically resolved, global, gap-free ozone database for assessing or constraining global climate model simulations, Earth System Science Data, 5, 31–43, doi:10.5194/essd-5-31-2013, URL http://www.earth-syst-sci-data.net/5/31/2013/, 2013.

Boone, C. D., Nassar, R., Walker, K. A., Rochon, Y., McLeod, S. D., Rinsland, C. P., and Bernath, P. F.: Retrievals for the atmospheric chemistry experiment Fourier-transform spectrometer, Applied Optics, 44, 7218–7231, 2005.

Brown, A. T., Volk, C. M., Schoeberl, M. R., Boone, C. D., and Bernath, P. F.: Stratospheric lifetimes of CFC-12, $CCl_4$, $CH_4$, $CH_3Cl$ and $N_2O$ from measurements made by the Atmospheric Chemistry Experiment-Fourier Transform Spectrometer (ACE-FTS), Atmospheric Chemistry and Physics, 13, 6921–6950, doi:10.5194/acp-13-6921-2013, URL http://www.atmos-chem-phys.net/13/6921/2013/, 2013.

Brühl, C., Lelieveld, J., Crutzen, P. J., and Tost, H.: The role of carbonyl sulphide as a source of stratospheric sulphate aerosol and its impact on climate, Atmospheric Chemistry and Physics, 12, 1239–1253, doi:10.5194/acp-12-1239-2012, URL http://www.atmos-chem-phys.net/12/1239/2012/, 2012.

Chin, M. and Davis, D. D.: Global sources and sinks of OCS and CS2 and their distributions, Global Biogeochemical Cycles, 7, 321–337, doi:10.1029/93GB00568, URL http://dx.doi.org/10.1029/93GB00568, 1993.

Chin, M. and Davis, D. D.: A reanalysis of carbonyl sulfide as a source of stratospheric background sulfur aerosol, Journal of Geophysical Research: Atmospheres, 100, 8993–9005, doi:10.1029/95JD00275, URL http://dx.doi.org/10.1029/95JD00275, 1995.

Coffey, M. T. and Hannigan, J. W.: The temporal trend of stratospheric carbonyl sulfide, Journal of Atmospheric Chemistry, 67, 61, doi:10.1007/s10874-011-9203-4, URL http://dx.doi.org/10.1007/s10874-011-9203-4, 2011.

Crutzen, P. J.: The possible importance of CSO for the sulfate layer of the stratosphere, Geophysical Research Letters, 3, 73–76, doi:10.1029/GL003i002p00073, URL http://dx.doi.org/10.1029/GL003i002p00073, 1976.

Du, Q., Zhang, C., Mu, Y., Cheng, Y., Zhang, Y., Liu, C., Song, M., Tian, D., Liu, P., Liu, J., Xue, C., and Ye, C.: An important missing source of atmospheric carbonyl sulfide: Domestic coal combustion, Geophysical Research Letters, 43, 8720–8727, doi:10.1002/2016GL070075, URL http://dx.doi.org/10.1002/2016GL070075, 2016GL070075, 2016.

Fischer, H., Birk, M., Blom, C., Carli, B., Carlotti, M., von Clarmann, T., Delbouille, L., Dudhia, A., Ehhalt, D., Endemann, M., Flaud, J. M., Gessner, R., Kleinert, A., Koopman, R., Langen, J., López-Puertas, M., Mosner, P., Nett, H., Oelhaf, H., Perron, G., Remedios, J., Ridolfi, M., Stiller, G., and Zander, R.: MIPAS: an instrument for atmospheric and climate research, Atmospheric Chemistry and Physics, 8, 2151–2188, doi:10.5194/acp-8-2151-2008, URL http://www.atmos-chem-phys.net/8/2151/2008/, 2008.

Fried, A., Drummond, J. R., Henry, B., and Fox, J.: Versatile integrated tunable diode laser system for high precision: application for ambient measurements of OCS, Appl. Opt., 30, 1916–1932, doi:10.1364/AO.30.001916, URL http://ao.osa.org/abstract.cfm?URI=ao-30-15-1916, 1991.

Fu, R., Hu, Y., Wright, J. S., Jiang, J. H., Dickinson, R. E., Chen, M., Filipiak, M., Read, W. G., Waters, J. W., and Wu, D. L.: Short circuit of water vapor and polluted air to the global stratosphere by convective transport over the Tibetan Plateau, Proceedings of the National Academy of Sciences, 103, 5664–5669, doi:10.1073/pnas.0601584103, URL http://www.pnas.org/content/103/15/5664.abstract, 2006.

Glatthor, N., Höpfner, M., Baker, I. T., Berry, J. E., Campbell, J. E., Kawa, S. R., Krysztofiak, G. P., Leyser, A., Sinnhuber, B.-M., Stiller, G. P., Stinecipher, J. E., and Von Clarmann, T. T.: Tropical sources and sinks of carbonyl sulfide observed from space, Geophysical Research Letters, 42, 10 082–10 090, doi:10.1002/2015GL066293, URL https://hal-insu.archives-ouvertes.fr/insu-01363835, 2015.

Glatthor, N., Höpfner, M., Leyser, A., Stiller, G. P., von Clarmann, T., Grabowski, U., Kellmann, S., Linden, A., Sinnhuber, B.-M., Krysztofiak, G., and Walker, K. A.: Global carbonyl sulfide (OCS) measured by MIPAS/Envisat during 2002–2012, Atmospheric Chemistry and Physics, 17, 2631–2652, doi:10.5194/acp-17-2631-2017, URL http://www.atmos-chem-phys.net/17/2631/2017/, 2017.

HAMAMATSU PHOTONICS K.K.: Test Datasheet Of QC-laser, Characteristic data of LC0107, 2009.

Hanst, P. L., Spiller, L. L., Watts, D. M., Spence, J. W., and Miller, M. F.: Infrared Measurement of Fluorocarbons, Carbon Tetrachloride, Carbonyl Sulfide, And Other Atmospheric Trace Gases, Journal of the Air Pollution Control Association, 25, 1220–1226, doi:10.1080/00022470.1975.10470199, URL http://dx.doi.org/10.1080/00022470.1975.10470199, 1975.

Hassler, B.: Global patterns in halogen-induced changes in vertically resolved stratospheric ozone, Ph.D. thesis, Ludwig-Maximilians-Universität München, 2009.

Höpfner, M., Glatthor, N., Grabowski, U., Kellmann, S., Kiefer, M., Linden, A., Orphal, J., Stiller, G., von Clarmann, T., Funke, B., and Boone, C. D.: Sulfur dioxide ($SO_2$) as observed by MIPAS/Envisat: temporal development and spatial distribution at 15–45 km altitude, Atmospheric Chemistry and Physics, 13, 10 405–10 423, doi:10.5194/acp-13-10405-2013, URL http://www.atmos-chem-phys.net/13/10405/2013/, 2013.

Inn, E. C. Y., Vedder, J. F., Tyson, B. J., and O'Hara, D.: COS in the stratosphere, Geophysical Research Letters, 6, 191–193, doi:10.1029/GL006i003p00191, URL http://dx.doi.org/10.1029/GL006i003p00191, 1979.

Johnson, J. E.: The lifetime of carbonyl sulfide in the troposphere, Geophysical Research Letters, 8, 938–940, doi:10.1029/GL008i008p00938, URL http://dx.doi.org/10.1029/GL008i008p00938, 1981.

Junge, C. E. and Manson, J. E.: Stratospheric aerosol studies, Journal of Geophysical Research, 66, 2163–2182, doi:10.1029/JZ066i007p02163, URL http://dx.doi.org/10.1029/JZ066i007p02163, 1961.

Junge, C. E., Chagnon, C. W., and Manson, J. E.: Stratospheric Aerosols, Journal of Meteorology, 18, 81–108, doi:10.1175/1520-0469(1961)018<0081:SA>2.0.CO;2, URL http://dx.doi.org/10.1175/1520-0469(1961)018<0081:SA>2.0.CO;2, 1961.

Kaye, J. A. and Miller, T. L.: The ATLAS series of shuttle missions, Geophysical Research Letters, 23, 2285–2288, doi:10.1029/96GL02228, URL http://dx.doi.org/10.1029/96GL02228, 1996.

Kettle, A. J., Kuhn, U., von Hobe, M., Kesselmeier, J., and Andreae, M. O.: Global budget of atmospheric carbonyl sulfide: Temporal and spatial variations of the dominant sources and sinks, Journal of Geophysical Research: Atmospheres, 107, ACH 25–1–ACH 25–16, doi:10.1029/2002JD002187, URL http://dx.doi.org/10.1029/2002JD002187, 4658, 2002.

Kremser, S., Jones, N. B., Palm, M., Lejeune, B., Wang, Y., Smale, D., and Deutscher, N. M.: Positive trends in Southern Hemisphere carbonyl sulfide, Geophysical Research Letters, 42, 9473–9480, doi:10.1002/2015GL065879, URL http://dx.doi.org/10.1002/2015GL065879, 2015GL065879, 2015.

Kremser, S., Thomason, L. W., von Hobe, M., Hermann, M., Deshler, T., Timmreck, C., Toohey, M., Stenke, A., Schwarz, J. P., Weigel, R., Fueglistaler, S., Prata, F. J., Vernier, J.-P., Schlager, H., Barnes, J. E., Antuña-Marrero, J.-C., Fairlie, D., Palm, M., Mahieu, E., Notholt, J., Rex,

M., Bingen, C., Vanhellemont, F., Bourassa, A., Plane, J. M. C., Klocke, D., Carn, S. A., Clarisse, L., Trickl, T., Neely, R., James, A. D., Rieger, L., Wilson, J. C., and Meland, B.: Stratospheric aerosol—Observations, processes, and impact on climate, Reviews of Geophysics, 54, 278–335, doi:10.1002/2015RG000511, URL http://dx.doi.org/10.1002/2015RG000511, 2015RG000511, 2016.

Krysztofiak, G., Té, Y. V., Catoire, V., Berthet, G., Toon, G. C., Jégou, F., Jeseck, P., and Robert, C.: Carbonyl Sulphide (OCS) Variability with Latitude in the Atmosphere, Atmosphere-Ocean, 53, 89–101, doi:10.1080/07055900.2013.876609, URL http://dx.doi.org/10.1080/07055900.2013.876609, 2015a.

Krysztofiak, G., Té, Y. V., Catoire, V., Berthet, G., Toon, G. C., Jégou, F., Jeseck, P., and Robert, C.: Carbonyl sulfide (OCS) variability with latitude in the atmosphere, Atmosphere-Ocean, 53, 89–101, doi:10.1080/07055900.2013.876609, URL https://hal-insu.archives-ouvertes.fr/insu-00906943, 2015b.

Kuai, L., Worden, J., Kulawik, S. S., Montzka, S. A., and Liu, J.: Characterization of Aura TES carbonyl sulfide retrievals over ocean, Atmospheric Measurement Techniques, 7, 163–172, doi:10.5194/amt-7-163-2014, URL http://www.atmos-meas-tech.net/7/163/2014/, 2014.

Kuai, L., Worden, J. R., Campbell, J. E., Kulawik, S. S., Li, K., Lee, M., Weidner, R. J., Montzka, S. A., Moore, F. L., Berry, J. A., et al.: Estimate of carbonyl sulfide tropical oceanic surface fluxes using Aura Tropospheric Emission Spectrometer observations, Journal of Geophysical Research: Atmospheres, 120, 2015.

Lennartz, S. T., Marandino, C. A., von Hobe, M., Cortes, P., Quack, B., Simo, R., Booge, D., Pozzer, A., Steinhoff, T., Arevalo-Martinez, D. L., Kloss, C., Bracher, A., Röttgers, R., Atlas, E., and Krüger, K.: Direct oceanic emissions unlikely to account for the missing source of atmospheric carbonyl sulfide, Atmospheric Chemistry and Physics, 17, 385–402, doi:10.5194/acp-17-385-2017, URL http://www.atmos-chem-phys.net/17/385/2017/, 2017.

Li, Q., Palmer, P. I., Pumphrey, H. C., Bernath, P., and Mahieu, E.: What drives the observed variability of HCN in the troposphere and lower stratosphere?, Atmospheric Chemistry and Physics, 9, 8531–8543, doi:10.5194/acp-9-8531-2009, URL http://www.atmos-chem-phys.net/9/8531/2009/, 2009.

Mahieu, E., Rinsland, C., Zander, R., Duchatelet, P., Servais, C., and De Maziere, M.: Tropospheric and Stratospheric Carbonyl Sulfide (OCS): long-term trends and seasonal Cycles above the Jungfraujoch Station, EUR 20650, URL http://hdl.handle.net/2268/101162, 2003.

Minschwaner, K., Manney, G. L., Livesey, N. J., Pumphrey, H. C., Pickett, H. M., Froidevaux, L., Lambert, A., Schwartz, M. J., Bernath, P. F., Walker, K. A., and Boone, C. D.: The

photochemistry of carbon monoxide in the stratosphere and mesosphere evaluated from observations by the Microwave Limb Sounder on the Aura satellite, Journal of Geophysical Research: Atmospheres, 115, n/a–n/a, doi:10.1029/2009JD012654, URL http://dx.doi.org/10.1029/2009JD012654, d13303, 2010.

Montzka, S. A., Aydin, M., Battle, M., Butler, J. H., Saltzman, E. S., Hall, B. D., Clarke, A. D., Mondeel, D., and Elkins, J. W.: A 350-year atmospheric history for carbonyl sulfide inferred from Antarctic firn air and air trapped in ice, Journal of Geophysical Research: Atmospheres, 109, n/a–n/a, doi:10.1029/2004JD004686, URL http://dx.doi.org/10.1029/2004JD004686, d22302, 2004.

Montzka, S. A., Calvert, P., Hall, B. D., Elkins, J. W., Conway, T. J., Tans, P. P., and Sweeney, C.: On the global distribution, seasonality, and budget of atmospheric carbonyl sulfide (COS) and some similarities to $CO_2$, Journal of Geophysical Research: Atmospheres, 112, n/a–n/a, doi:10.1029/2006JD007665, URL http://dx.doi.org/10.1029/2006JD007665, d09302, 2007.

Notholt, J., Kuang, Z., Rinsland, C. P., Toon, G. C., Rex, M., Jones, N., Albrecht, T., Deckelmann, H., Krieg, J., Weinzierl, C., Bingemer, H., Weller, R., and Schrems, O.: Enhanced Upper Tropical Tropospheric COS: Impact on the Stratospheric Aerosol Layer, Science, 300, 307–310, doi:10.1126/science.1080320, URL http://science.sciencemag.org/content/300/5617/307, 2003.

O'Keefe, A. and Deacon, D. A. G.: Cavity ring-down optical spectrometer for absorption measurements using pulsed laser sources, Review of Scientific Instruments, 59, 1988.

O'Keefe, A., Scherer, J. J., and Paul, J. B.: cw Integrated cavity output spectroscopy, Chemical Physics Letters, 307, 343 – 349, doi:http://dx.doi.org/10.1016/S0009-2614(99)00547-3, URL http://www.sciencedirect.com/science/article/pii/S0009261499005473, 1999.

O'Shea, S. J., Bauguitte, S. J.-B., Gallagher, M. W., Lowry, D., and Percival, C. J.: Development of a cavity-enhanced absorption spectrometer for airborne measurements of $CH_4$ and $CO_2$, Atmospheric Measurement Techniques, 6, 1095–1109, doi:10.5194/amt-6-1095-2013, URL http://www.atmos-meas-tech.net/6/1095/2013/, 2013.

Pan, L. L., Honomichl, S. B., Kinnison, D. E., Abalos, M., Randel, W. J., Bergman, J. W., and Bian, J.: Transport of chemical tracers from the boundary layer to stratosphere associated with the dynamics of the Asian summer monsoon, Journal of Geophysical Research: Atmospheres, 121, 14,159–14,174, doi:10.1002/2016JD025616, URL http://dx.doi.org/10.1002/2016JD025616, 2016JD025616, 2016.

Park, M., Randel, W. J., Emmons, L. K., Bernath, P. F., Walker, K. A., and Boone, C. D.: Chemical isolation in the Asian monsoon anticyclone observed in Atmospheric Chemistry

Experiment (ACE-FTS) data, Atmospheric Chemistry and Physics, 8, 757–764, doi:10.5194/acp-8-757-2008, URL http://www.atmos-chem-phys.net/8/757/2008/, 2008.

Park, M., Randel, W. J., Emmons, L. K., and Livesey, N. J.: Transport pathways of carbon monoxide in the Asian summer monsoon diagnosed from Model of Ozone and Related Tracers (MOZART), Journal of Geophysical Research: Atmospheres, 114, n/a–n/a, doi:10.1029/2008JD010621, URL http://dx.doi.org/10.1029/2008JD010621, d08303, 2009.

Ploeger, F., Gottschling, C., Griessbach, S., Grooß, J.-U., Guenther, G., Konopka, P., Müller, R., Riese, M., Stroh, F., Tao, M., Ungermann, J., Vogel, B., and von Hobe, M.: A potential vorticity-based determination of the transport barrier in the Asian summer monsoon anticyclone, Atmospheric Chemistry and Physics, 15, 13 145–13 159, doi:10.5194/acp-15-13145-2015, URL http://www.atmos-chem-phys.net/15/13145/2015/, 2015.

Pommrich, R., Müller, R., Grooß, J.-U., Konopka, P., Ploeger, F., Vogel, B., Tao, M., Hoppe, C. M., Günther, G., Spelten, N., Hoffmann, L., Pumphrey, H.-C., Viciani, S., D'Amato, F., Volk, C. M., Hoor, P., Schlager, H., and Riese, M.: Tropical troposphere to stratosphere transport of carbon monoxide and long-lived trace species in the Chemical Lagrangian Model of the Stratosphere (CLaMS), Geoscientific model development discussions, 7, 5087 – 5139, doi:10.5194/gmdd-7-5087-2014, URL http://juser.fz-juelich.de/record/154949, 2014.

Provencal, R., Gupta, M., Owano, T. G., Baer, D. S., Ricci, K. N., O'Keefe, A., and Podolske, J. R.: Cavity-enhanced quantum-cascade laser-based instrument for carbon monoxide measurements, Appl. Opt., 44, 6712–6717, doi:10.1364/AO.44.006712, URL http://ao.osa.org/abstract.cfm?URI=ao-44-31-6712, 2005.

Randel, W. J., Park, M., Emmons, L., Kinnison, D., Bernath, P., Walker, K. A., Boone, C., and Pumphrey, H.: Asian Monsoon Transport of Pollution to the Stratosphere, Science, 328, 611–613, doi:10.1126/science.1182274, URL http://science.sciencemag.org/content/328/5978/611, 2010.

Rinsland, C. P., Goldman, A., Mahieu, E., Zander, R., Notholt, J., Jones, N. B., Griffith, D. W. T., Stephen, T. M., and Chiou, L. S.: Ground-based infrared spectroscopic measurements of carbonyl sulfide: Free tropospheric trends from a 24-year time series of solar absorption measurements, Journal of Geophysical Research: Atmospheres, 107, ACH 24–1–ACH 24–9, doi:10.1029/2002JD002522, URL http://dx.doi.org/10.1029/2002JD002522, 4657, 2002.

Rinsland, C. P., Chiou, L., Mahieu, E., Zander, R., Boone, C. D., and Bernath, P. F.: Measurements of long-term changes in atmospheric {OCS} (carbonyl sulfide) from infrared solar observations, Journal of Quantitative Spectroscopy and Radiative Transfer, 109, 2679 – 2686, doi:http://dx.doi.org/10.1016/j.jqsrt.2008.07.008, URL http://www.sciencedirect.com/science/article/pii/S0022407308001611, 2008.

Sandoval-Soto, L., Stanimirov, M., von Hobe, M., Schmitt, V., Valdes, J., Wild, A., and Kesselmeier, J.: Global uptake of carbonyl sulfide (COS) by terrestrial vegetation: Estimates corrected by deposition velocities normalized to the uptake of carbon dioxide ($CO_2$), Biogeosciences, 2, 125–132, doi:10.5194/bg-2-125-2005, URL http://www.biogeosciences.net/2/125/2005/, 2005.

Sayres, D. S., Moyer, E. J., Hanisco, T. F., St. Clair, J. M., Keutsch, F. N., O'Brien, A., Allen, N. T., Lapson, L., Demusz, J. N., Rivero, M., Martin, T., Greenberg, M., Tuozzolo, C., Engel, G. S., Kroll, J. H., Paul, J. B., and Anderson, J. G.: A new cavity based absorption instrument for detection of water isotopologues in the upper troposphere and lower stratosphere, Review of Scientific Instruments, 80, 044102, doi:http://dx.doi.org/10.1063/1.3117349, URL http://scitation.aip.org/content/aip/journal/rsi/80/4/10.1063/1.3117349, 2009.

Schrade, S.: Ground based measurements of Carbon Dioxide and other climatically relevant trace gases using Off-Axis Integrated-Cavity-Output-Spectroscopy (ICOS), Diplomarbeit, RWTH Aachen University, 2011.

Sheng, J.-X., Weisenstein, D. K., Luo, B.-P., Rozanov, E., Stenke, A., Anet, J., Bingemer, H., and Peter, T.: Global atmospheric sulfur budget under volcanically quiescent conditions: Aerosol-chemistry-climate model predictions and validation, Journal of Geophysical Research: Atmospheres, 120, 256–276, doi:10.1002/2014JD021985, URL http://dx.doi.org/10.1002/2014JD021985, 2014JD021985, 2015.

Simkin, T. and Fiske, R.: Krakatau, 1883–the volcanic eruption and its effects, Smithsonian Institution Press, URL https://books.google.de/books?id=i7cPAQAAMAAJ, 1983.

Solomon, S., Daniel, J. S., Neely, R. R., Vernier, J.-P., Dutton, E. G., and Thomason, L. W.: The Persistently Variable "Background" Stratospheric Aerosol Layer and Global Climate Change, Science, 333, 866–870, doi:10.1126/science.1206027, URL http://science.sciencemag.org/content/333/6044/866, 2011.

Staudt, A. C., Jacob, D. J., Logan, J. A., Bachiochi, D., Krishnamurti, T. N., and Sachse, G. W.: Continental sources, transoceanic transport, and interhemispheric exchange of carbon monoxide over the Pacific, Journal of Geophysical Research: Atmospheres, 106, 32 571–32 589, doi:10.1029/2001JD900078, URL http://dx.doi.org/10.1029/2001JD900078, 2001.

Stimler, K., Montzka, S. A., Berry, J. A., Rudich, Y., and Yakir, D.: Relationships between carbonyl sulfide (COS) and $CO_2$ during leaf gas exchange, New Phytologist, 186, 869–878, doi:10.1111/j.1469-8137.2010.03218.x, URL http://dx.doi.org/10.1111/j.1469-8137.2010.03218.x, 2010a.

Stimler, K., Nelson, D., and Yakir, D.: High precision measurements of atmospheric concentrations and plant exchange rates of carbonyl sulfide using mid-IR quantum cascade laser, Global Change Biology, 16, 2496–2503, doi:10.1111/j.1365-2486.2009.02088.x, URL http://dx.doi.org/10.1111/j.1365-2486.2009.02088.x, 2010b.

Thompson, D. W. J., Wallace, J. M., Jones, P. D., and Kennedy, J. J.: Identifying Signatures of Natural Climate Variability in Time Series of Global-Mean Surface Temperature: Methodology and Insights, Journal of Climate, 22, 6120–6141, doi:10.1175/2009JCLI3089.1, URL http://dx.doi.org/10.1175/2009JCLI3089.1, 2009.

Toohey, M. and von Clarmann, T.: Climatologies from satellite measurements: the impact of orbital sampling on the standard error of the mean, Atmospheric Measurement Techniques, 6, 937–948, doi:10.5194/amt-6-937-2013, URL http://www.atmos-meas-tech.net/6/937/2013/, 2013.

Toohey, M., Strong, K., Bernath, P. F., Boone, C. D., Walker, K. A., Jonsson, A. I., and Shepherd, T. G.: Validating the reported random errors of ACE-FTS measurements, Journal of Geophysical Research: Atmospheres, 115, n/a–n/a, doi:10.1029/2010JD014185, URL http://dx.doi.org/10.1029/2010JD014185, d20304, 2010.

Toohey, M., Hegglin, M. I., Tegtmeier, S., Anderson, J., Añel, J. A., Bourassa, A., Brohede, S., Degenstein, D., Froidevaux, L., Fuller, R., Funke, B., Gille, J., Jones, A., Kasai, Y., Krüger, K., Kyrölä, E., Neu, J. L., Rozanov, A., Smith, L., Urban, J., von Clarmann, T., Walker, K. A., and Wang, R. H. J.: Characterizing sampling biases in the trace gas climatologies of the SPARC Data Initiative, Journal of Geophysical Research: Atmospheres, 118, 11,847–11,862, doi:10.1002/jgrd.50874, URL http://dx.doi.org/10.1002/jgrd.50874, 2013JD020298, 2013.

Ulshöfer, V. S. and Andreae, M.: Carbonyl Sulfide (COS) in the Surface Ocean and the Atmospheric COS Budget, Aquatic Geochemistry, 3, 283–303, doi:10.1023/A:1009668400667, URL http://dx.doi.org/10.1023/A:1009668400667, 1997.

Van Diest, H. and Kesselmeier, J.: Soil atmosphere exchange of carbonyl sulfide (COS) regulated by diffusivity depending on water-filled pore space, Biogeosciences, 5, 475–483, doi:10.5194/bg-5-475-2008, URL http://www.biogeosciences.net/5/475/2008/, 2008.

Velazco, V. A., Toon, G. C., Blavier, J. L., Kleinböhl, A., Manney, G. L., Daffer, W. H., Bernath, P. F., Walker, K. A., and Boone, C.: Validation of the Atmospheric Chemistry Experiment by noncoincident MkIV balloon profiles, Journal of Geophysical Research: Atmospheres, 116, n/a–n/a, doi:10.1029/2010JD014928, URL http://dx.doi.org/10.1029/2010JD014928, d06306, 2011.

Vernier, J.-P., Thomason, L. W., and Kar, J.: CALIPSO detection of an Asian tropopause aerosol layer, Geophysical Research Letters, 38, n/a–n/a, doi:10.1029/2010GL046614, URL http://dx.doi.org/10.1029/2010GL046614, l07804, 2011a.

Vernier, J.-P., Thomason, L. W., Pommereau, J.-P., Bourassa, A., Pelon, J., Garnier, A., Hauchecorne, A., Blanot, L., Trepte, C., Degenstein, D., and Vargas, F.: Major influence of tropical volcanic eruptions on the stratospheric aerosol layer during the last decade, Geophysical Research Letters, 38, n/a–n/a, doi:10.1029/2011GL047563, URL http://dx.doi.org/10.1029/2011GL047563, l12807, 2011b.

Viciani, S., D'Amato, F., Mazzinghi, P., Castagnoli, F., Toci, G., and Werle, P.: A cryogenically operated laser diode spectrometer for airborne measurement of stratospheric trace gases, Applied Physics B, 90, 581–592, doi:10.1007/s00340-007-2885-2, URL http://dx.doi.org/10.1007/s00340-007-2885-2, 2008.

Vincent, R. A. and Dudhia, A.: Fast retrievals of tropospheric carbonyl sulfide with IASI, Atmospheric Chemistry and Physics, 17, 2981–3000, doi:10.5194/acp-17-2981-2017, URL http://www.atmos-chem-phys.net/17/2981/2017/, 2017.

Vogel, B., Günther, G., Müller, R., Grooß, J.-U., and Riese, M.: Impact of different Asian source regions on the composition of the Asian monsoon anticyclone and of the extratropical lowermost stratosphere, Atmospheric Chemistry and Physics, 15, 13 699–13 716, doi:10.5194/acp-15-13699-2015, URL https://www.atmos-chem-phys.net/15/13699/2015/, 2015.

von Hobe, M., Kuhn, U., Diest, H. V., Sandoval-Soto, L., Kenntner, T., Helleis, F., Yonemura, S., Andreae, M. O., and Kesselmeier, J.: Automated in situ analysis of volatile sulfur gases using a Sulfur Gas Analyser (SUGAR) based on cryogenic trapping and gas-chromatographic separation, International Journal of Environmental Analytical Chemistry, 88, 303–315, doi:10.1080/03067310701642081, URL http://www.tandfonline.com/doi/abs/10.1080/03067310701642081, 2008.

Wang, Y., Deutscher, N. M., Palm, M., Warneke, T., Notholt, J., Baker, I., Berry, J., Suntharalingam, P., Jones, N., Mahieu, E., Lejeune, B., Hannigan, J., Conway, S., Mendonca, J., Strong, K., Campbell, J. E., Wolf, A., and Kremser, S.: Towards understanding the variability in biospheric $CO_2$ fluxes: using FTIR spectrometry and a chemical transport model to investigate the sources and sinks of carbonyl sulfide and its link to $CO_2$, Atmospheric Chemistry and Physics, 16, 2123–2138, doi:10.5194/acp-16-2123-2016, URL http://www.atmos-chem-phys.net/16/2123/2016/, 2016.

Wardencki, W.: Problems with the determination of environmental sulphur compounds by gas chromatography, Journal of Chromatography A, 793, 1 – 19, doi:http://doi.org/

10.1016/S0021-9673(97)00997-7, URL http://www.sciencedirect.com/science/article/pii/S0021967397009977, 1998.

Wofsy, S. C.: HIAPER Pole-to-Pole Observations (HIPPO): fine-grained, global-scale measurements of climatically important atmospheric gases and aerosols, Philosophical Transactions of the Royal Society of London A: Mathematical, Physical and Engineering Sciences, 369, 2073–2086, doi:10.1098/rsta.2010.0313, URL http://rsta.royalsocietypublishing.org/content/369/1943/2073, 2011.

Xu, X., Bingemer, H. G., and Schmidt, U.: An empirical model for estimating the concentration of carbonyl sulfide in surface seawater from satellite measurements, Geophysical Research Letters, 29, 30–1–30–4, doi:10.1029/2001GL014252, URL http://dx.doi.org/10.1029/2001GL014252, 2002.

Zöger, M., Afchine, A., Eicke, N., Gerhards, M.-T., Klein, E., McKenna, D. S., Mörschel, U., Schmidt, U., Tan, V., Tuitjer, F., Woyke, T., and Schiller, C.: Fast in situ stratospheric hygrometers: A new family of balloon-borne and airborne Lyman $\alpha$ photofragment fluorescence hygrometers, Journal of Geophysical Research: Atmospheres, 104, 1807–1816, doi:10.1029/1998JD100025, URL http://dx.doi.org/10.1029/1998JD100025, 1999.

# Acknowledgements

Firstly, I would like to thank my advisor Dr. Marc von Hobe for a number of things: his enthusiastic commitment to supporting me throughout both projects of this work (even during his vacation time), his encouragement and good team work during AMICA development and lab tests, his insightful comments on my work as well as for all the sight seeing and running tours we did in between meetings.
Besides my advisor, I would like to thank Prof. Dr. Thorsten Benter, the supervisor of my work and Prof. Dr. Martin Riese and Dr. Fred Stroh for the opportunity to do my PhD at IEK-7 at Forschungszentrum Jülich, GmbH and the other members of my thesis committee Prof. Dr. Hans-Willi Kling and Dr. Rolf Müller.
I am grateful for the opportunity to be a part of the big StratoClim community and the involved measurement campaigns.
For the ACE-FTS part of my thesis I had support from Dr. Kaley Walker from the department of physics at the University of Toronto, who was the corresponding contact regarding the access of the ACE-FTS data, Dr. Rolf Müller and Dr. Jens-Uwe Grooß, who supported me with comments and discussions, as well as Dr. Michael Höpfner, who provided the MIPAS data set for validation purposes.
I thank the HITEC graduate school for the research grant to support my project and especially enjoyed the Scientific presentation courses, additionally I thank the ROMIC-SPITFIRE project for funding my PhD. During my thesis I had the chance to visit Bodeker Scientific in Alexandra, New Zealand with the HITEC Go program. I would like to thank Dr. Stefanie Kremser and Prof. Dr. Greg Bodeker for the chance to visit Bodeker Scientific, the input and additional ideas to my work.
The AMICA-team consists of numerous people: especially I would like to thank Vicheith Tan for his continuous and devoting support, but also the colleges from ZEA-1 (especially Herbert Schneider, Johannes Schillings, Achim Gussen and Thomas Kulessa) and Los Gatos Research (especially Dr. Brian Leen, Aaron Gardner and Garrett Madsen), as well as Nicole Spelten.
During my programming battles with python, I had support from many people, I would like to thank especially Dr. Christian Rolf for his help and patience, as well as Dr. Jörn Ungermann, Kage Nesbit and Ben Lewis.

I furthermore would like to thank Dr. Felix Plöger for his support and Karlheinz Nogai for the best office company, the best coffees at Forschungszentrum, Green Day breaks and running lunch breaks.

Band / Volume 385
**Bestimmung der Wolframerosion mittels optischer Spektroskopie unter ITER-relevanten Plasmabedingungen**
M. Laengner (2017), vi, 184, XI pp
ISBN: 978-3-95806-257-3

Band / Volume 386
**IEK-3 Report 2017**
Sector Coupling –
Research for an Integrated Energy System
(2017), 175 pp
ISBN: 978-3-95806-258-0

Band / Volume 387
**Photochemistry of Highly Oxidized Multifunctional Organic Molecules: a Chamber Study**
L. I. M. Pullinen (2017), II, 96, xviii pp
ISBN: 978-3-95806-260-3

Band / Volume 388
**Poröse Transportschichten für die Polymerelektrolytmembran-Wasserelektrolyse**
M. Höh (2017), VI, 186 pp
ISBN: 978-3-95806-262-7

Band / Volume 389
**Modelling of High Temperature Polymer Electrolyte Fuel Cells**
Q. Cao (2017), 173 pp
ISBN: 978-3-95806-263-4

Band / Volume 390
**Potential use of nitrification inhibitors for mitigating $N_2O$ emission from soils**
D. Wu (2017), 206 pp
ISBN: 978-3-95806-264-1

Band / Volume 391
**Mechanical Characterization of Solid Oxide Fuel Cells and Sealants**
J. Wei (2017), II, 151 pp
ISBN: 978-3-95806-266-5

Band / Volume 392
**Microcrystalline Silicon Carbide for Silicon Heterojunction Solar Cells**
M. B. Pomaska (2017), 150 pp
ISBN: 978-3-95806-267-2

Band / Volume 393
**Einfluss der Kristallisation auf das Fließverhalten oxidischer Schmelzen**
S. Seebold (2017), 168 pp
ISBN: 978-3-95806-268-9

Band / Volume 394
**Water vapour in the UTLS – Climatologies and Transport**
P. R. Neis (2017), x, 124 pp
ISBN: 978-3-95806-269-6

Band / Volume 395
**Neutronenaktivierungsanalyse mit gepulsten 14 MeV Neutronen zur Charakterisierung heterogener radioaktiver Abfälle**
F. Mildenberger (2017), vi, 128 pp
ISBN: 978-3-95806-271-9

Band / Volume 396
**Coupled biotic-abiotic mechanisms of nitrous oxide production in soils during nitrification involving the reactive intermediates hydroxylamine and nitrite**
S. Liu (2017), xvii, 148 pp
ISBN: 978-3-95806-272-6

Band / Volume 397
**Mixed-phase and ice cloud observations with NIXE-CAPS**
A. Costa (2017), xviii, 117 pp
ISBN: 978-3-95806-273-3

Band / Volume 398
**Deposition Mechanisms of Thermal Barrier Coatings (TBCs) Manufactured by Plasma Spray-Physical Vapor Deposition (PS-PVD)**
W. He (2017), ix, ca. 162 pp
ISBN: 978-3-95806-275-7

Band / Volume 399
**Carbonyl Sulfide in the Stratosphere: airborne instrument development and satellite based data analysis**
C. Kloss (2017), vi, 84, 1-14 pp
ISBN: 978-3-95806-276-4

Weitere ***Schriften des Verlags im Forschungszentrum Jülich*** unter
http://wwwzb1.fz-juelich.de/verlagextern1/index.asp

Energie & Umwelt /
Energy & Environment
Band / Volume 399
ISBN 978-3-95806-276-4